



Run Run Shaw Library

香港城市大學
City University of Hong Kong

Copyright Warning

Use of this thesis/dissertation/project is for the purpose of private study or scholarly research only. ***Users must comply with the Copyright Ordinance.***

Anyone who consults this thesis/dissertation/project is understood to recognise that its copyright rests with its author and that no part of it may be reproduced without the author's prior written consent.



邵逸夫圖書館
Run Run Shaw Library

Copyright Warning

Use of this thesis/dissertation/project is for the purpose of private study or scholarly research only. ***Users must comply with the Copyright Ordinance.***

Anyone who consults this thesis/dissertation/project is understood to recognise that its copyright rests with its author and that no part of it may be reproduced without the author's prior written consent.

CITY UNIVERSITY OF HONG KONG
香港城市大學

**On Urban Precipitation in the
Pearl River Delta Region**
珠三角區域的市區降水

Submitted to
School of Energy and Environment
能源及環境學院
in Partial Fulfilment of the Requirements
for the Degree of Doctor of Philosophy
哲學博士學位
by
Christopher Claus HOLST

December 2016
二零一六年十二月

Abstract

On Urban Precipitation in the Pearl River Delta Region

by Christopher Claus HOLST

In the research leading to this thesis the complex behaviour of precipitation was investigated over urban environments and their direct vicinity. The Pearl River Delta Region as one of South China's largest urban accumulations with Hong Kong located at its edge served as an ideal study area. The sensitivity of rainfall to anthropogenic sensible heat fluxes, urban extent and large scale variability have been studied in a series of partially idealized real-case scenarios and mechanisms potentially leading up to previously observed changes could be derived from the results. Urban precipitation scaling depends on the investigated forcing physics in complex ways and is discussed in detail in the thesis. Anthropogenic heat flux is contributing to heavier precipitation more than light precipitation through convective processes and increased buoyancy and turbulence. This mechanism only applies for sufficiently large urban areas and sufficient amounts of anthropogenic heat release. In smaller urban clusters, the initiated buoyancy is not resulting in local precipitation increases but rather downstream increases, dependent on advection length scales in comparison to buoyant (convection penetration) length scales and spatial extent of the urban cluster. Changes in the large scale moisture fields affect the precipitation in a more complex way in that the ratio of amounts of light and heavy precipitation is affected by background moisture adjustments. The relative importance of local convection and advection effects, as well as atmospheric stability parameters are affected by the background moisture changes. After taking into account these findings, one may conclude that observed changes in precipitation climate do not necessarily depend on global climate change, but show signatures of local forcing. In the final part of the thesis a discussion of the relevance of the study and its relation to past and future studies concludes, that the study of micro climatic forcing behaviour is essential to understand the larger scale changes which have been observed in the past century.

CITY UNIVERSITY OF HONG KONG

Qualifying Panel and Examination Panel

Author: Christopher Claus HOLST

Degree: Doctor of Philosophy

Department: School of Energy and Environment

The Qualifying Panel of the above student is composed of:

Supervisor:

Prof. CHAN Chung Leung Johnny School of Energy and Environment
City University of Hong Kong

Qualifying Panel Members:

Dr. LAM Yun Fat Nicky	School of Energy and Environment City University of Hong Kong
Dr. NGAN Keith	School of Energy and Environment City University of Hong Kong

This thesis has been examined and approved by the following examiners:

Prof. BRIMBLECOMBE Peter	School of Energy and Environment City University of Hong Kong
Prof. CHAN Chung Leung Johnny	School of Energy and Environment City University of Hong Kong
Prof. FUNG Chi Hung	Division of Environment Hong Kong University of Science & Technology
Prof. LI Yuguo	Department of Mechanical Engineering The University of Hong Kong

Declaration of Authorship

I, Christopher Claus HOLST, declare that this thesis titled, 'On Urban Precipitation in the Pearl River Delta Region' and the work presented in it are my own. I confirm that:

- This work was done wholly or mainly while in candidature for a research degree at this University.
- Where any part of this thesis has previously been submitted for a degree or any other qualification at this University or any other institution, this has been clearly stated.
- Where I have consulted the published work of others, this is always clearly attributed.
- Where I have quoted from the work of others, the source is always given. With the exception of such quotations, this thesis is entirely my own work.
- I have acknowledged all main sources of help.
- Where the thesis is based on work done by myself jointly with others, I have made clear exactly what was done by others and what I have contributed myself.

Signed:

Date:

Don't you have time to think?

Richard Feynman

Don't worry, be grumpy.

Ajahn Brahm

Just because it has been done the same way for generations doesn't mean that it makes sense.

William Gelvin

I'm going to sharpen my chisels now. Nothing better than working with sharp tools.

Ben Crowe

I prefer to not trust knowledge too much, as it is increasingly incomplete. Wisdom is far more appealing; being elusive, infinite and truthful. Just like stupidity.

Christopher C. Holst

Acknowledgements

This work would have been impossible without the support of my family, friends, mentors and guides. This section is dedicated to those people as a reminder for the change they have done to my life and motivation to change many more lives, as teachers often do but rarely get acknowledgement for.

I would like to thank Johnny Chan and Francis Tam for supervising me throughout my study and guiding me through times of doubt. My mentors throughout my academic study (in unspecific order) Julian Hunt, Peter Brimblecombe, Keith Ngan, Thomas Hauf, Siegfried Raasch, Gunther Seckmeyer and Günter Gross have left marks on my work and thinking processes and will continue to inspire me.

Larry Ng and Kevin Downing have been there for me when I was lost in various ways and showed me new facets of my life.

My friends Romain Carlevan, Eric Ng, Andie Au-Yeung and Lars Schönemann have played important roles in maintaining my sanity throughout the process and enabled me to become myself.

My parents Claus and Angelika Holst, who have never doubted me or stopped me, whatever silly plan and idea I came up with, letting me discover and explore the world and myself along the way, teaching me everything they know and forging my curiosity, creativity and grit.

My brother Daniel Holst, who is the person who has been closest to me for the longest period of time.

Elva Bai, my dear wife, who has been with me through the past seven years, being my motivation and challenge, my hope and trust and frustration at times. Without her, my life had taken a very different trajectory.

A large number of people who taught me different interesting skills without asking for anything in return, some without ever meeting me but by providing free education online. Among them are Brian Boyd, Alexandar Djordjevich, Cédric Villani, Vincenzo Nardelli, William Gelvin, Gordon Hon and many more.

Ajahn Brahm has saved me from insanity in the final stage of my study, when life struck me with several unexpected beatings, making me stumble and almost fall. He is among the wisest people of his generation and opened up my heart, turning

the harshest moments of life into the most empowering experiences.

This thesis may just be a piece of work, but it is the culmination of stimulations, that happened over a period of years. Maybe one day someone will be inspired through my teachings and I can hand on some of the gifts that all these amazing people shared with me.

Contents

Abstract	i
Declaration of Authorship	iv
Acknowledgements	vi
List of Figures	xiii
List of Tables	xvii
Abbreviations	xix
Physical Constants	xxi
Symbols	xxiii
1 Description of the problem	1
1.1 Observations	1
1.2 Hypothesis	2
1.2.1 Passive energy storage	2
1.2.2 Particles	3
1.2.3 Energy release	3
1.2.4 Surface sealing	4
1.2.5 Climate Change	4
1.3 Summary and study design	4
2 Literature review	7
2.1 Urban meso-scale meteorology	8
2.1.1 Urban atmospheric layers	9
2.1.2 Urban energy balance	10
2.2 Urban Precipitation	12
2.2.1 Structure and intensity of rainfall	12
2.2.2 Results of model simulations	13

2.2.3	Scale interactions	14
2.2.4	Model studies with the Weather Research and Forecast model	16
2.3	Brief summary	17
3	Methodology	19
3.1	The monsoon-trough summer storm benchmark case	19
3.2	Model system	21
3.2.1	Simulation domain	21
3.2.2	Initial and lateral boundary conditions	23
3.2.3	Dynamics and physics	26
3.3	Experiment design	27
3.3.1	Human activities	28
3.3.1.1	An illustrative example of AH estimation	31
3.3.2	Urban spatial extent	32
3.3.3	Large scale variability	33
3.4	Brief overview	34
4	Effects of anthropogenic heat	35
4.1	Quantification of model results	36
4.1.1	Model precipitation	36
4.1.2	Statistical parameters	36
4.1.2.1	Domain and sub-domain statistics	36
4.1.2.2	Distribution bin values	37
4.1.3	Reference simulation and comparison	38
4.1.4	Model realism	38
4.2	Rainfall sensitivity to anthropogenic heat	40
4.2.1	Accumulated precipitation	40
4.2.2	Statistics of raining grid points	42
4.2.3	Simulated precipitation intensity	44
4.2.4	The role of buoyancy and shear	45
4.3	Brief summary	47
5	Effects of urban spatial extent	51
5.1	Sampling area	52
5.1.1	Interpretation of different sampling areas	53
5.1.1.1	Stationary local data in "urban 1984"	53
5.1.1.2	Regional data in "urban 2004"	53
5.2	Precipitation intensity	53
5.2.1	Sensitivity in the region ("urban 2004")	55
5.2.2	Sensitivity in the old city ("urban 1984")	55
5.2.3	Amount and occurrence of rainfall	56
5.2.4	Interpretation	56
5.3	Brief summary	59
6	Effects of background moisture changes	61

6.1	Initial conditions	62
6.2	Precipitation statistics	64
6.2.1	Moisture dependence of the AH sensitivity	65
6.2.1.1	Urban sensitivity	65
6.2.1.2	Non-urban sensitivity	66
6.2.1.3	Urban effects in non-urban land	66
6.2.2	Moisture sensitivity	69
6.3	Vertical structure of the atmosphere	70
6.3.1	Temperature changes	71
6.3.2	Water vapour changes	72
6.3.3	Stability and cloud changes	75
6.4	Brief summary	77
7	Concluding remarks and future investigations	79
7.1	Concluding remarks	79
7.2	Suggested future studies	81
A	Compilation and performance	83
A.1	Compilation	83
A.1.1	Dependency Compilation	83
A.1.2	Model Code Compilation	84
A.2	Performance	85
A.2.1	Experiment for Large Scale Domain (D01)	85
A.2.2	Experiments for Small Scale Domains (D02, D03)	86
B	Model land use	89
B.1	Overview over the land use	89
C	Calculation of the equivalent potential temperature	93
C.1	Calculation of dewpoint temperature and saturation vapour pressure	93
C.2	Conversion from vapour pressure to mixing ratio	94
C.3	Temperatures at lifting condensation levels	96
C.4	Estimation of the equivalent potential temperature	96
D	Simulated Surface Variables	99
D.1	Example Snapshots	99
Bibliography		101

List of Figures

2.1	A schematic of the boundary layer structure in an urban environment, from Oke [1988]. The different layers are labelled in (a) and subdivided in (b) accordingly assuming that a background flow is approaching from the left boundary as indicated by arrows.	9
2.2	Urban Heat Island effect as observed when comparing temperature records from stations at the Hong Kong Observatory (HKO) and Ta Ku Ling (TKL), from Lam [2011].	11
3.1	Large scale surface weather map (0000 GMT, 07 June 2008) from the Hong Kong Observatory website, adopted from Holst et al. [2016]. The trough line can be seen parallel to the South China Sea coast.	20
3.2	Scales in atmospheric processes as horizontal bars and typical numerical model grid spacings as vertical lines. The numerics associated are large eddy simulation (blue), numerical weather prediction (red), regional climate models (green) and general circulation models (grey).	22
3.3	Model domain topography height in a nested setting. The grid spacings in the daughter domains are following a nesting ratio of 1:5. In Figure (a) the outermost domain D01 is shown with the daughter domains incorporated. (b) and (c) show the nested domains D02 and D03 respectively.	24
3.4	Urban land cover in the innermost domain shown in red with major cities indicated as dots.	25
3.5	Comparison of model temporal weighting function $\psi(t)$ for AH value scaling 3.5a and monthly averages of diurnal point measurements of AH in Hung Hom 3.5b [Oke, 1988].	30
3.6	Urban land use in domain 3 approximately 1984 (USGS data) in (a) and approximately 2004 (MODIS data) in (b).	32
4.1	Radar precipitation estimation product from the Hong Kong Observatory website for 1100 HKT on the 6 June 2008 (a) for comparison with simulated hourly precipitation rates at the same time of incidence for AH = 0 (b) and AH = 500 W m^{-2} (c). Adopted from Holst et al. [2016] supplementary materials.	39

4.2 Comparison of accumulated rainfall divided by simulation time (i.e. simulation average) for different AH scenarios: (a) 0 W m^{-2} , (b) 50 W m^{-2} , (c) 100 W m^{-2} , (d) 250 W m^{-2} , (e) 500 W m^{-2} and (f) 5 kW m^{-2} . Units: mm h^{-1} .	42
4.3 Snapshots of hourly precipitation rate values at (a, c) 1100 Hong Kong time on 6 June 2008 and (b, d) 1300 Hong Kong time on 7 June 2008, for AH = 0 (a, b) and AH = 500 W m^{-2} (c, d) model experiments. Unit: mm h^{-1} . Replotted from Holst et al. [2016].	43
4.4 Simulated relative occurrence likelihood of different precipitation intensity bands in the non-urban (a) and urban (b) parts of the domain for different values of AH. The insets illustrate the change of each experiment with a different AH value relative to the reference case without AH forcing. The colours of the bars and lines indicate the different values of AH [W m^{-2}] as labelled on the top of each figure. Adopted from Holst et al. [2016].	49
4.5 The ratio ($500\text{AH} : 0\text{AH}$) of standard deviations of PBL-averaged \bar{e} in (a) and Rif in (b). Adopted from Holst et al. [2016].	50
5.1 Model urban extent in 1984 (a) and 2004 (b). The plot shows domain 2 ($5 \times 5 \text{ km}^2$ grid spacing) and embedded in the box domain 3 ($1 \times 1 \text{ km}^2$ grid spacing).	52
5.2 PDF histogram and sensitivity plots as insets for different sampling areas ((a, b): "urban 2004" and (c, d): "urban 1984") and different AH forcing values and areas. Areas and lines in grey/black shades refer to forcing with "1984" urban extent while red shades refer to the respective "2004" extent. The shadings indicate magnitude of the AH parameter's values of 0 (reference case), 250 and 500 W m^{-2} as in the legend on the top of each panel. For clarity the areas are shown in the insets on the right side with matching colours.	54
5.3 Average and standard deviation of the vertical equivalent potential temperature gradient. The ratios (500 W m^{-2} AH)/(0 W m^{-2} AH) for two different comparisons 1984-1984 (a, b) and 2004-2004 (c, d) heat forcing areas are presented here.	58
6.1 The vertical profile of the layer water vapour mixing ratio in the initial condition, normalized with the column moisture.	63
6.2 Simulated precipitation intensity distribution for (a) urban and (b) non-urban sub-domains. The cases Q090 in red colours refer to dry conditions while Q110 in blue refer to wet conditions. Different AH values are shown in different shades and denoted as AH000, AH250 and AH500 (refer to the legend at the top). The insets show the AH-sensitivity of each of the non-zero AH PDF divided by the corresponding zero-AH PDF, for example Q090-AH250/Q090-AH000.	65

6.3 Comparison of (a, b, c) dry and (d, e, f) wet scenario accumulated precipitation pattern with reference simulations (e.g. Q100–Q090 and Q100–Q110) for different values of AH (0, 250 and 500 W m ⁻² as 3 columns). Each panel has the title to indicate the comparison shown. The colours show dryer conditions relative to reference moisture (red and black) and wetter conditions (blue and white), while light green indicates no changes. The contour lines show the outlines of urban (black) and water (blue) model land use categories.	67
6.4 Urban (a) and non-urban (b) moisture sensitivity of precipitation for different AH values. Dry scenarios are plotted in red and wet scenarios in blue. In each line, the dry/wet case is compared corresponding to the reference case, please refer to the legend. The dashed line shows the ratio of 1, indicating no change.	70
6.5 Vertical profiles of average Θ_v in the urban (a, c) and non-urban (b, d) sub-domains. The different colours refer to different scenarios for AH = 0 and 500 W m ⁻² and Q = 90, 100 and 110 % as shown in the legends at the top of each panel. The profiles are presented for (a, b)	73
6.6 Same as Figure 6.5 but for Q_{vapour}	74
6.7 Vertical profiles of average (a, b) Θ_e and (c, d) Q_{cloud} . Similar to previous profiles in Figures 6.6 and 6.5.	76
6.8 Vertical profiles of average difference $Q_{cloud}(\text{AH} = 500 \text{ W m}^{-2}) - Q_{cloud}(\text{AH} = 0)$. The green line indicates no difference.	77
B.1 Model domain land use dominant categories plotted for all domains in (a) 1984 and (b) 2004. The colours are explained in Table B.1 and the white lines indicate nest locations.	91
D.1 Simulated surface temperatures (a), surface winds (b) and precipitation rates (c) in an example on 7 June 2008 at 16:35.	100

List of Tables

3.1	Details of the model domain geometry.	23
3.2	Parametrization schemes used in the simulations of this study.	27
4.1	Total amount of accumulated precipitation for the entire domain, the urban and non-urban sub-domains for different values of AH. The increase relative to zero AH depicted as Δ_{0AH}	41
4.2	As in Table 4.1 except for the number of precipitating grid points.	44
5.1	Accumulated rainfall for different experiments "1984 AH" and "2004 AH" indicating the boundary conditions. Urban ₁₉₈₄ and Urban ₂₀₀₄ refer to the sampling areas. 0, 250 and 500 W m ⁻² are the values of the AH parameter in the simulations. The relative change between "1984" and "2004" AH forcing areas is indicated as Δ_{2004} and for each of the cases the sensitivity to AH is given as Δ_{0AH}	56
5.2	As in Table 5.1, except for the occurrence of rainfall in grid points.	57
5.3	Average and standard deviations of $\nabla_z \Theta_e$ for both scenarios in the domain and urban sub-domain. Units:	59
6.1	The vertical distribution of moisture in the model initial condition.	63
6.2	Scenario labels in Chapter 6 for the simulations with different moisture conditions and different AH parameters.	64
A.1	Estimated computational calls of dynamics and physics with relative comparison for different domains. The unit M in this case refers to 10 ⁶	87
B.1	Colour codes in Figure B.1. The author attempted to choose the colours in a reasonably intuitive way.	90
C.1	Coefficients for the empirical Arden Buck formula [Buck, 2012].	94

Abbreviations

AH	Anthropogenic Heat
BouLac	Bougeault-Lacarre scheme
FNL	Final Reanalysis dataset
LCL	Lifting Condensation Level
LSM	Land Surface Model
METROMEX	METROpolitan Meteorological EXperiment
MM5	Pennsylvania State University-NCAR Mesoscale Model 5
MODIS	Moderate-resolution Imaging Spectroradiometer
NAS	New Arakawa Schubert scheme
NCAR	National Center for Atmospheric Research
NCEP	National Center for Environmental Prediction
PBL	Planetary Boundary Layer
PDF	Probability Density Function
PR	Accumulated PRecipitation
PR1	Precipitation Rate extrapolated to 1 hour
RAMS	Regional Atmospheric Modeling System
RBL	Rural Boundary Layer
RRTMG	Rapid Radiative Transfer Model for Global applications
SCS	South China Sea
TKE	Turbulence Kinetic Energy
UBL	Urban Boundary Layer
UHI	Urban Heat Island
USGS	United States Geological Survey
WRF	Weather Research and Forecast model

Physical Constants

Gravitational acceleration	g	=	9.81 m s^{-2}
von-Kármán constant	κ	=	0.41
Poisson constant	$\kappa_d = \frac{R_d}{C_{pd}}$	=	0.2854
Specific gas constant for dry air	R_d	=	$287.058 \text{ J kg}^{-1} \text{ K}^{-1}$
Specific gas constant for water vapour	R_v	=	$461.5 \text{ J kg}^{-1} \text{ K}^{-1}$
Specific heat of dry air (constant pressure)	C_{pd}	=	$1005.7 \text{ J kg}^{-1} \text{ K}^{-1}$

Symbols

AH	Anthropogenic heat flux	W m^{-2}
C_{pd}	Specific heat of dry air (constant pressure)	$\text{J kg}^{-1} \text{K}^{-1}$
d	Differential operator	dimensionless
\bar{e}	Turbulence kinetic energy	$\text{m}^2 \text{s}^{-2}$
e	Partial pressure of water vapour	hPa
e_s	Saturation partial pressure of water vapour	hPa
g	Gravitational acceleration	m s^{-2}
\vec{k}	Unit vector in z-direction	dimensionless
L_v	Latent heat of evaporation	J kg^{-1}
m_d	Mass of dry air	kg
m_v	Mass of water vapour	kg
N	Number	dimensionless
p	Pressure	hPa
p_0	Reference pressure	hPa
PR	Accumulated precipitation	mm
$PR1$	Hourly precipitation rate	mm h^{-1}
Q_v	Water vapour mixing ratio	dimensionless
R_d	Specific gas constant for dry air	$\text{J kg}^{-1} \text{K}^{-1}$
R_v	Specific gas constant for water vapour	$\text{J kg}^{-1} \text{K}^{-1}$
S	Sensible heat flux	W m^{-2}
t	Time	s
T	Temperature	K
T_D	Dewpoint Temperature	K
T_e	Equivalent Temperature	K
T_L	Temperature at lifting condensation level	K
\vec{u}	Velocity vector	m s^{-1}
u	Velocity component in x-direction	m s^{-1}

Symbols

v	Velocity component in y-direction	m s^{-1}
w	Velocity component in z-direction	m s^{-1}
$\beta = \frac{g}{\Theta_v}$	Buoyancy coefficient	$\text{m s}^{-2} \text{K}^{-1}$
∂	Partial differential operator	dimensionless
δ	Kronecker delta operator	dimensionless
Δ	Discrete differencing operator	dimensionless
κ	von-Kármán constant	dimensionless
κ_d	Poisson constant	dimensionless
$\nabla_z = \frac{\partial}{\partial z} \vec{k}$	Vertical gradient operator	m^{-1}
ν	Molecular momentum diffusion coefficient	$\text{m}^2 \text{s}^{-1}$
ρ	Density	kg m^{-3}
ρ_d	Density of dry air	kg m^{-3}
ρ_v	Density of water vapour	kg m^{-3}
σ	Vertical coordinate	dimensionless
$\dot{\sigma}$	Vertical velocity	s^{-1}
Θ	Potential temperature	K
Θ_e	Equivalent potential temperature	K
Θ_L	Potential temperature at lifting condensation level	K
Θ_v	Virtual potential temperature	K

To my wife Elva.

of past work focusing on urban rainfall and meteorology in general are reviewed in Chapter 2. Based on that, a description of the tools used to investigate the problem are presented in Chapter 3. The results of these experiments are described and interpreted in Chapters 4, 5 and 6. Finally in Chapter 7, a number of conclusions towards applicability and representativeness as well as a preview on future investigations are provided.

1.2 Hypothesis

The question raised in the previous paragraph can be interpreted in different ways. One interpretation regards the urban area as a micro climate system that exerts certain independent forcing upon itself, in which case the proper question to ask will be which forcing affects the local rainfall. Another interpretation is respective larger scale variability, for example synoptic scale changes of moisture, temperature or wind. In the latter case, one should ask how the local system responds to external forcing and variability of what can be referred to as background climate. The methodology to investigate the second interpretation can potentially yield controversy, as there are a range of possible approaches to study climate sensitivity and the results can depend on the methodology applied. Hence it is difficult to study in a systematic way, yielding potentially more questions than answers and in this thesis the first question is investigated in detail. Rephrasing it yields a clear formulation of the problem: which aspect of urban land can potentially lead to increased local precipitation?

A number of hypotheses will be briefly described in the following short paragraphs.

1.2.1 Passive energy storage

The urban heat island effect is a phenomenon of increased surface air temperature, especially during night times, caused by higher heat capacity of concrete as compared to soil or vegetation. An example from Hong Kong will be given in the

following paragraph 2.1.2. Hence sunlight can be absorbed and stored effectively by the surface structures and materials causing a slow release of sensible heat after the solar irradiation passes its maximum at approximately noon. This effect reduces the relative humidity of air due to temperature increase. Because the amount of water molecules in the air is not affected, hence through the increase of saturation vapour pressure an increased accumulation time of vapour potentially suppresses light precipitation, while heavy precipitation is less sensitive to the suppression effect. The contrast of warm surface air and cooler surrounding air can cause a secondary circulation similar to a sea breeze, but more complex, because urban areas do typically have complex geometry. One may think of a city with some closed outline, the secondary circulation can result in a convergent flow in the evening hours and potentially cause rising motion and rainfall due to this effect.

1.2.2 Particles

Human activities release particles through combustion engines and mechanical friction processes in general. If more nucleation particles of certain type are available in the atmosphere, water vapour condenses to form a larger number of droplets. If the mass of water vapour is unchanged, one can conclude that precipitation is less likely, unless sufficient amounts of water are available, causing heavier precipitation as droplets take more time to grow through collision coalescence. This would result in less light precipitation and more heavy precipitation. The hypothesis depends on the composition of particle properties like particle surface area, hydrophilic or hydrophobic characteristics, static charge and other parameters, significantly enhancing the difficulty of studying the effects.

1.2.3 Energy release

Engines, electrical appliances and other machines release heat at the surface. For the sake of completeness warm-blooded bodies have to be mentioned as well, but it

is unclear how much energy is released by mammals' respiration and transpiration. One can ask how this heat will possibly affect the local micro climate and aspects of precipitation generation like buoyancy and convection. It is reasonable to assume that increased heat release at the surface increases atmospheric instability and hence can amplify convection and other more turbulent phenomena like mixing.

1.2.4 Surface sealing

If the land surface is covered with concrete and drainage systems are utilized, it is possible that less water is evaporated locally due to extraction into underground drainage systems at the surface. Re-evaporation is however a complicated process because it may be enhanced by stored heat in the surface materials. This can produce a layer of saturated air near the surface. Depending on the stability of the atmosphere this moisture may sustain local rainfall through rising motion or simply store the latent heat in the mixed layer.

1.2.5 Climate Change

If the climate state is changing towards increased temperature and moisture such changes similar to the above described effects can take place. However, the mechanisms and scale interactions are complex and it is not straight forward to give conjectures towards such relationships with confidence.

1.3 Summary and study design

In order to investigate the local system's sensitivity to the parameters that build the foundation of the hypothesis, a model simulation approach is selected. It is important to keep the comparison simulations as simple as possible as to identify those parameters that contribute to potential precipitation changes.

This study addresses local scale and global scale aspects of the systems behaviour.

The intensity of human activity is investigated by studying the parameter of anthropogenic heat flux and the spatial extent of the urban area. In simpler words one may ask how much activity humans can exert upon a city until the local micro-climate is affected and on the other hand, whether or not the size of a city matters for these effects. The larger scale sensitivity is investigated by forcing the numerical model with perturbed initial- and boundary-conditions as well as applying spectral nudging of corresponding large scale forcing data. This experiment is technically not a climate change study but rather a climate sensitivity study and hence only provides general hints towards possible footprints of large scale changes in local systems.

Chapter 2

Literature review

In order to understand the dynamics and thermodynamics of urban environments in meteorology, it is conducive to find a more precise perspective on the question that should be put into test. Referring to the quote in the preface, it is of great importance to comprehend the problem itself in such a way, that a precise question can be posed, whose answer needs to be interpretable and solve the problem. In order phrase a proper question to investigate regarding the hypothesis stated above, the literature covered in this review is sorted into two categories. Firstly, an overview about fundamental urban meso-scale meteorology and urban micro climate effects will be covered to demonstrate the behaviour of flows that are affected by such land surface. In the second part the focus is on precipitation and how cities are known to interact with precipitation.

The earliest account that could be identified regarding differences between urban and rural environments is a publication about non-instrumental observations reported by Mossman [1897] (see also Mossman [1898a] and Mossman [1898b]). The author mentioned that lightning seemed to occur more often in cities than rural areas. One can argue that the density of observers and hence the likelihood of observing an event is much higher in cities. There is a counter argument that farmers should be more aware and observant of heavy precipitation and thunderstorms as their crop yields may be affected by their occurrence, so overall the reliability of such eye witness data is questionable. The account merely serves as

a hint, that meteorologists already had similar ideas about the contents of this study from early on, but lacked the tools to carry out investigation that would withstand modern scientific scrutiny.

2.1 Urban meso-scale meteorology

Urban meteorology covers a variety of scales. Reference orders of magnitude for spatial extends in the scales as used in this study are provided throughout this paragraph. A large amount of currently ongoing work in micro scale meteorology (below $\mathcal{O}(1 \text{ km})$ spatial extend), more precisely street- and neighbourhood scales ($\mathcal{O}(100 - 1000 \text{ m})$ spatial extend), e.g. street canyon flows, dispersion of chemicals in urban boundary layers or thermal comfort on neighbourhood scales. In this study and review however, the focus will remain on meso-beta ($\mathcal{O}(10 - 100 \text{ km})$ spatial extend) and meso-gamma scales ($\mathcal{O}(1 - 10 \text{ km})$ spatial extend), hence flow features on kilometre scales and above, e.g. entire neighbourhoods being the smallest distinguishable objects of interest while cities and regions are in the focus.

Before discussing about local effects it is important to take note of scale interactions and how larger features of flows are affected by smaller scale changes. An illustrative example of scale interactions is the study of Dalu et al. [1991] in which changes in boundary layer stress were shown to induce mesoscale vertical velocity changes. High-rise buildings introduce changes of dynamic stress in the urban boundary layers. The vertical velocity is directly related to precipitation, as lifting of moist air causes adiabatic cooling through decreasing density. Cooling below the dew point temperature (e.g. the temperature at which the relative humidity equals 100 %) causes super-saturation and condensation (Wallace and Hobbs [2006]).

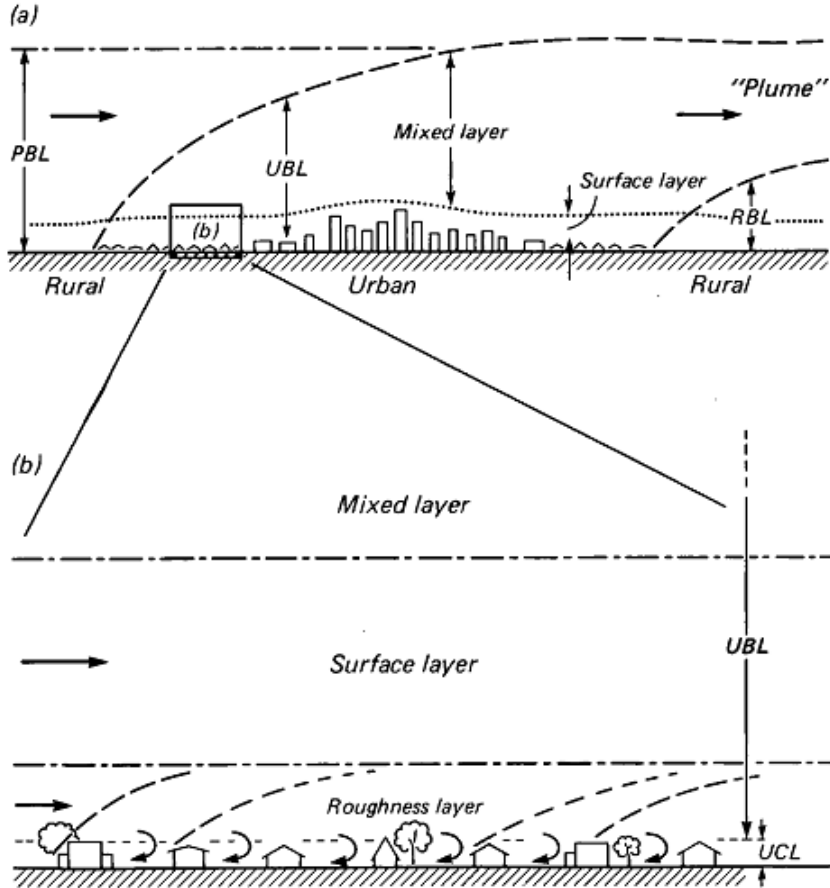


FIGURE 2.1: A schematic of the boundary layer structure in an urban environment, from Oke [1988]. The different layers are labelled in (a) and subdivided in (b) accordingly assuming that a background flow is approaching from the left boundary as indicated by arrows.

2.1.1 Urban atmospheric layers

Oke [1988] conceptualized urban flows by defining layers in which different effects can occur as shown in Figure 2.1a. The planetary boundary layer (PBL) can be separated into a surface layer and a mixed layer and further classified as urban- or rural boundary layer (UBL and RBL) respectively. The classification depends on the background flow as indicated by horizontal arrows at the left boundary of the schematic and the curvature of the boundary between the mixed UBL and PBL and UBL and RBL respectively. In Figure 2.1b the surface layer is further divided into a roughness layer and an urban canopy layer (UCL) which is dependent on the height of building structures and the magnitude of the approaching wind.

The concept of "plumes" as being the remainder of urban mixed layers that is

transported by a background flow will be important for understanding the scaling behaviour of urban precipitation. A further important concept is the definition of mixed layers itself, which in this study will be assumed as a layer in which the moist static stability of the air is neutral, e.g. no net gravity effects (buoyancy). This definition has significance as it reduces the dynamic properties of such flow to isotropy, meaning that properties of the flow are independent of spatial directions. In real cases this rarely occurs. Hence, it is necessary to apply such concepts with care. Theoretically one can define a base state of the atmosphere, in which the fluid is in a mixed condition upon which a perturbation of buoyancy fluctuations is introduced (e.g. warm air bubbles in convective flows) or in general closed isosteres (lines/surfaces of equal density) which lift or fall through differential gravitational pull as compared to the surrounding fluid. These fundamental concepts appear simple on a phenomenological plane but the details become complex and difficult to fully grasp, so in this study no emphasis on details of these structures will be given.

2.1.2 Urban energy balance

Another important result summarized by Oke [1988] is that when a land surface interacts with the environment, not only is the velocity of the flow (e.g. through friction or roughness elements) modified, but the thermodynamic variables like heat and moisture as well. Different land surfaces, for example concrete versus grass land have different physical properties such as heat capacity, heat conductivity, surface area, permeability/porosity (in the case of moisture) and other factors, which play important roles determining the physical interactions with air and soil temperature, evaporation, soil moisture, precipitation, albedo and other coupled variables. The differences in thermodynamic behaviour can explain the phenomenon which is called urban heat island (UHI). This phenomenon is best described by an example in Figure 2.2. The temperature records at two stations have been compared by Lam [2011] and the differences in diurnal wave amplitude as well as average can be seen. The line labelled TKL refers to a rural station (Ta

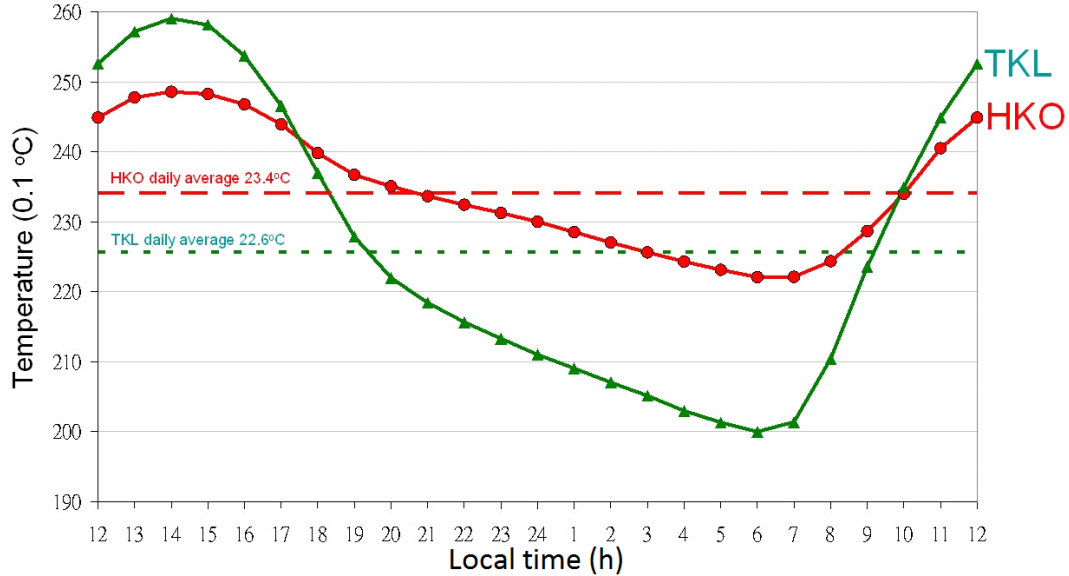


FIGURE 2.2: Urban Heat Island effect as observed when comparing temperature records from stations at the Hong Kong Observatory (HKO) and Ta Ku Ling (TKL), from Lam [2011].

Kwu Ling) while HKO refers to the Hong Kong Observatory in the centre of the urban area. In this particular case the higher heat capacity and changes in albedo of the city affect the average, extremes and the rates of change of air temperature. Significant fundamental studies regarding simulations of UHI have been conducted by Vukovich and King [1980] for the city of St. Louis in the USA, using a relatively simple three dimensional model [Vukovich et al., 1976]. They found that for purely dynamic representations (e.g. cities represented by increased surface-roughness) the quality of UHI simulations compared to observations mainly depends on initial conditions. Hence the proper selection of simulated conditions is crucial to simulate realistic flow behaviour over cities. In another study [Vukovich and Dunn III, 1978] they found that the thermal stability of the PBL and urban-rural air temperature gradient determine the intensity of the secondary circulation.

The perspective described above is however slightly over-simplified. Oke [1988] described how human activities release heat as well, caused by combustion processes in vehicles, stoves, power plants as well as conversion of electric energy into heat in appliances. In addition to that, warm-blooded mammals such as humans also emit heat through respiration and transpiration, as discussed and described in Oke [1987] Chapter 6. No emphasis will be given here on trying to estimate that

contribution. In a densely populated and vibrant city like Hong Kong, this anthropogenic heat can have large magnitudes (see Figure 3.5b) and have important contributions to the atmospheric condition and thermal behaviour of the city's boundary layer. Further details will be described in Chapter 3.3.1

2.2 Urban Precipitation

2.2.1 Structure and intensity of rainfall

Ackerman et al. [1978] concluded from the Metropolitan Meteorological Experiment ("METROMEX"), that precipitation downwind of St. Louis is increased relative to other sectors. Furthermore, an increase of mixing height was observed over the city centre, leading to a relatively moist area atop of the city. They described a potential relation between the energy and moisture transport through the PBL to higher altitudes and the initiation of convective thunderstorms. Interpreting data from the same campaign, Huff and Changnon, Jr. [1972] showed that the precipitation rate downwind of the city is increased, especially that the frequency of hail days is increased by 35 %. One year later, they published another study [Huff and Changnon, jr., 1973] considering different urban areas in the United States, leading to a more comprehensive result. They found a positive trend of warm season precipitation between 1950 and 1970 with a magnitude of 9 – 17 %. They also confirmed that large urban areas showed a higher frequency of thunder days and hail days; however, the difference of thunder frequency occurred mainly near the city, while the difference in rainfall and hail was found to occur 25 – 55 kilometres downwind of the city.

A relationship between population density and likelihood of heavy precipitation was found by Krishtawal et al. [2010] who found a non-linear relation between satellite derived rainfall data and census data over India. Statistically significant differences also exist in the rainfall rate probability density functions between urban and rural areas, showing that urban areas tend to have higher precipitation rates.

Bornstein and Lin [2000] found a relationship between UHI intensity and the convergence and precipitation for a number of cases in Atlanta. They also confirmed storm-bifurcation as structure change in mesoscale initiated storms over the city, e.g. the splitting-up of storms over urban areas. A further study in Atlanta that is worth mentioning in this context was carried out by Dixon and Mote [2003] where they demonstrated that precipitation is more sensitive to low-level moisture content than to UHI intensity. They also found, that most of the urban-induced precipitation occurred within 10 kilometres of the densely urbanized areas.

Satellite observations were utilized by Shepherd and Burian [2003] to verify that the precipitation rates show good agreement with observed lightning anomalies [Orville et al., 2001]. Furthermore, they remarked that the role of aerosols is not well understood and requires further investigation.

2.2.2 Results of model simulations

In a combined model and observation study in Indianapolis, Niyogi et al. [2011] showed that the structure of storms changed over the urban centre. By analysing observations for 91 storms, systematic changes of size and shape, e.g. splitting, initiation, intensification and dissipation have been examined. The authors found that medium-size storms occurred upstream of the city, while slow and larger size storms were more likely to be found downstream of the city. In the modelling part of the study, certain storms could not be reproduced without the presence of a city when using the Pennsylvania State University-NCAR Mesoscale Model ("MM5"). The Regional Atmospheric Modeling System (RAMS) was utilized by Lei et al. [2008] in a case study of an extreme precipitation event in Mumbai to demonstrate the improvement of simulation results by the coupling of an explicit urban energy budget model. They found an increase of performance in terms of reproducing precipitation fields, depending on the choice of schemes and input data. In their simulations, the urban-induced dynamics caused a convergence line that transported moisture from the sea surface and thus was assumed to be the major reason for the heavy rainfall event over Mumbai.

Another model study using the RAMS model was conducted by van den Heever and Cotton [2007] with a 1.5km grid spacing. They found that the influence of urban dynamics on local precipitation behaviour was larger than that of aerosols (with cloud condensation nuclei number concentration ranges of $800 - 2000 \text{ cm}^{-3}$). However, Steiger and Orville [2003] concluded that the concentration of particulate matter in the atmosphere promotes cloud-to-ground lightning in areas where no significant urban heat islands are present. The discrepancy between these two studies suggests that the aerosol physics in the RAMS model may not be able to simulate the urban variability of thunderstorms.

Lo et al. [2007] investigated secondary circulations in the Pearl River Delta Region and Hong Kong using an updated land use data set in the MM5 model and found that a recent land use information data set is required to simulate such local simulations with MM5. Furthermore, Paegle et al. [1996] identified surface evaporation to be a crucial factor for amplification of certain kinds of synoptic-driven precipitation.

2.2.3 Scale interactions

Pielke, Sr et al. [2007] pointed out, that the influence of different land surface features is different, depending on the surface structure. This puts emphasis on the fundamental limitation to numerical models with finite grid spacings (e.g. in the order of kilometres) and their representativeness. It also limits the interpretation of simulation results with respect to scale interactions, especially in the context of urban environments and vegetation since the hydrology and energy balance are of significant importance to precipitation.

Recently, new implementations of land-use information, so-called tile-approaches have been implemented into meso-scale models by different groups in Europe. Bohnenstengel et al. [2011] have reported a successful modelling of the evolution and diurnal cycle of the London UHI. Furthermore, they successfully modelled the advection of warm air from the city to the rural areas directly downstream. The difference between traditional land surface models (LSM) and a tile-approach is

that one grid box of the surface can be assigned a composite of different physical parameters. For example, the orientation of buildings (north-south or east-west) is not homogeneous, but if the fractional distribution of both is known for an area, this information can be included in the model to provide a better representation of physical and dynamical properties of the surface. This also applies for subgrid scale information about the land-use. If 40% of a grid box is water surface, then the model would not simulate this contribution in the traditional LSM. But with a composite tile approach, this information can be taken into account. Basically it can be interpreted as an interpolation between different land-use categories. Early progress in that direction was made by Avissar and Pielke, Sr [1989].

Hamdi et al. [2013] have shown that the tile approach performs well for simulations with other models as well. By comparing three dynamical downscaling methods for the urban area of Brussels, they found decreasing trends in UHI intensity, if the model is forced with boundary conditions from a climate projection run of a global climate system model. They have shown that coupled urban models produce results that are closer to observations than so-called offline models, in which meteorological models and urban models are run separately. This is also consistent with observations made in comparison with the Noah LSM and its predecessor, the Oregon State University LSM (OSU) (compare Chen and Dudhia [2001] and Chen et al. [1996]).

On a global scale, Westra et al. [2013] have recently shown that annual maximum daily precipitation has a significant increasing trend. Furthermore, they linked the precipitation data with near-surface temperature data and confirmed that a relationship exists between trends in near-surface temperature and trends in annual maximum daily precipitation, as explained by Trenberth et al. [2003]. The quantity concerned is the so-called Clausius-Clapeyron ratio, that bears an increase of approximately 6 % increase of saturation vapour pressure per Kelvin temperature increase. This affects precipitation and yields the question whether the observed changes in Hong Kong can be attributed to global scale changes, as opposed to local changes through urban modifications.

2.2.4 Model studies with the Weather Research and Forecast model

Hong and Lee [2009] demonstrated that the Weather Research and Forecast model (WRF) can reasonably well simulate heavy rainfall in Korea, with a good temporal and spatial agreement. However, they reported the underestimation of precipitation magnitude in their simulations. The authors related the findings to the large scale circulation behaviour and low-level moisture convergence and advection, and concluded that a lack of sufficient moisture was responsible for the underestimating the amount of rain that was observed.

Yu et al. [2013] worked on a case study of the record breaking rainfall event in Beijing on 21 June 2012 using a simulation with four domains and applied different cumulus parametrization schemes for estimating the predictability of such rain. They found that the Global Forecast System forecast input data limited the lead time of predictability to approximately 36 hours. A sensitivity test showed that about 63 % of the precipitation could be attributed to orographic effects. The timing and magnitude of the precipitation in these simulations showed some deficits, but overall the authors concluded, that such simulation can predict and reproduce heavy precipitation as observed.

An extensive study of Penelly et al. [2013] describes a verification of WRF simulation performance for a number of heavy precipitation cases in Alberta, Canada. The authors tested different resolutions and convective schemes to draw the conclusion that the Kain-Fritsch scheme and explicit convection calculation performed best in their local context. This result is expected, but might be a consequence of local dynamical behaviour. They also stated in the model description that the model was used in an "off-the-shelf" manner, using the environmental modelling system's default configuration". It is therefore unlikely that any adjustment to physical parameters to account for local situations has been made.

Srikanth et al. [2014] conducted a comparison study that verifies different surface layer variables with radar observations. They found that certain features like surface temperature and surface wind can be reasonably reproduced as well

as convective instability, sudden rise in relative humidity and some other effects. However, there are limitations in scale interactions because pressure perturbations associated with thunderstorm squall lines were not successfully reproduced. This could be a feature of the vertical coordinate system, which is a hybrid pressure coordinate system and may prevent such local surface variations from occurring. Yu and Liu [2015] conducted model simulations for a rainstorm in Beijing, China, investigating the possible effects of urbanization onto precipitation and reported both, up- and down-wind effects and changes in magnitude of the precipitation in their simulation. Most recently, Li et al. [2016] described interactions of sea breeze circulations and anthropogenic heat flux and their effects upon local climate in Singapore. The concluded, that anthropogenic heat introduces buoyancy and surface sealing restricts evaporation, so the balance of those two effect can either enhance or suppress local precipitation. In this thesis the diurnal variability of precipitation is not investigated, but this may become part of future work to be done.

2.3 Brief summary

The effects of urban areas on precipitation spatial pattern, magnitudes and also urban temperatures have been observed and described in the past (refer to Chapters 2.2.1 and 2.1.2). Different model studies have worked on the reproduction of previously observed cases as well as fundamental mechanisms such as dynamic structures (secondary circulation systems) and urban heat islands (see Chapter 2.2.2) and an effort has been made to describe the scaling behaviour of precipitation (Chapter 2.2.3). In the more recent work, authors have aimed to produce hind-cast simulations with fine model grid spacings down to kilometre scales to investigate local physical behaviour of rainstorms in comparison with observations. In this study two aspects have been targeted, first the surface-atmosphere interactions and their effect on precipitation and secondly the local systems sensitivity to changes in large scale average moisture. This was done by simulating a past record-breaking heavy rainfall case as a reference and studying the sensitivity of

this case simulation to various modifications of the models lower boundary conditions. To retain the comparability of the cases, a spectral nudging approach for synoptic scales (e.g. ≥ 1000 km) was applied on the outermost domain. In the second part for the analysis of background moisture changes the initial conditions and nudging data have been modified as well.

The following Chapter 3 describes how the experiments are set up. The results are discussed in Chapters 4, 5 and 6. Finally in Chapter 7 a number of concluding remarks and resulting from that suggestions for future studies are provided.

Chapter 3

Methodology

In this chapter the details of the investigative approach will be presented in two sections. After introducing the benchmark case to study, the model system setting and the design of the experiments that have been carried out for this study will be explained. Because of redundancy, many technical details of the model which are documented elsewhere will be referred to but not further explained and more focus will be put on those parts which have been modified and the experiments that have been carried out.

3.1 The monsoon-trough summer storm benchmark case

Choosing a case to study with a numerical model can be a difficult pursuit. A good source is from Wu et al. [2015] who reported and characterized rain storm cases. As expected, much of Hong Kong's heavy precipitation is caused by either tropical cyclone rain bands or monsoon trough flows. Since tropical cyclones happen less reliably than monsoon flow features on an annual basis and the city is prepared for heavy rain during typhoons, a severe rainstorm during monsoon trough conditions is chosen for the present study, the case on 7 June 2008. The case was also described in Holst et al. [2016] and the following description is adopted from the

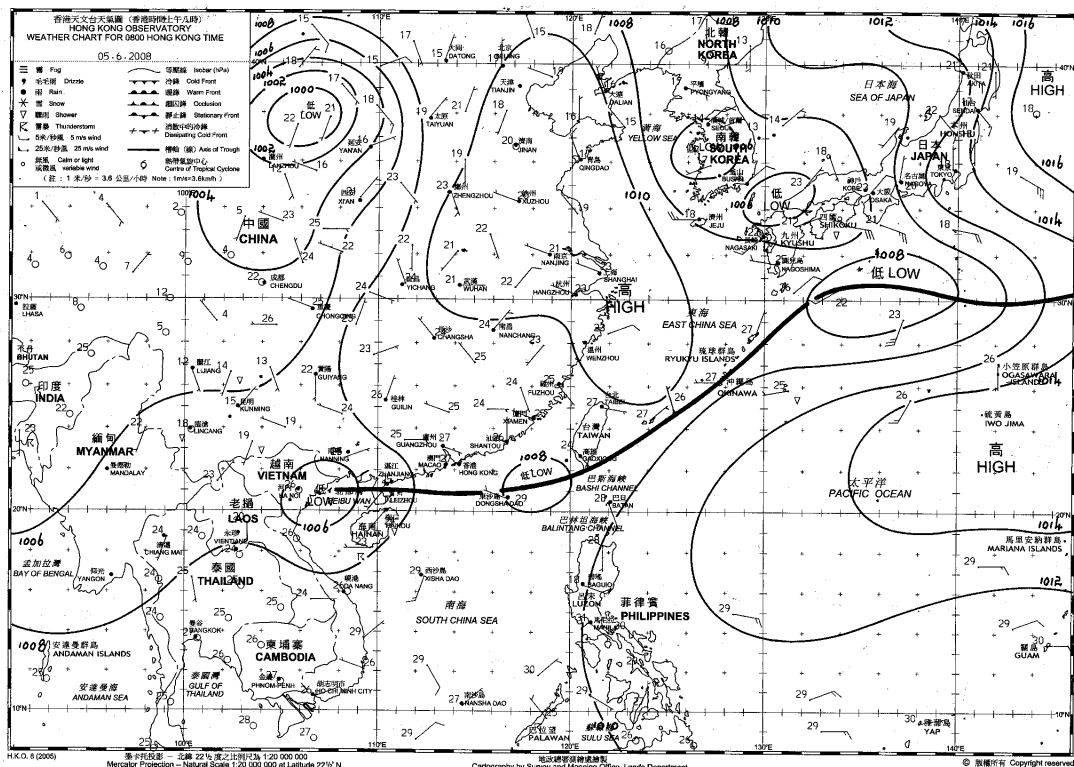


FIGURE 3.1: Large scale surface weather map (0000 GMT, 07 June 2008) from the Hong Kong Observatory website, adopted from Holst et al. [2016]. The trough line can be seen parallel to the South China Sea coast.

previous publication.

In early June 2008 a quasi-stationary surface pressure trough formed over the northernmost part of the South China Sea (SCS). This system extended from the open sea south-east of Japan past south Taiwan and the Bashi Channel all the way to Vietnam (see Figure 3.1). In the early summer monsoon season, such systems are not uncommon. With the westward extension of the subtropical high moving to the north on 6 June, the trough line followed. On the following day, the trough crossed the coast line of the South China Sea and southerly winds prevailed in Hong Kong. On that day, 7 June 2008, hourly rainfall rates reached 70 mm h^{-1} or more at many stations within Hong Kong. The system dissipated and a ridge line formed on 9 June associated with westward extension of the subtropical high approaching the SCS.

This case yields an interesting scenario as a short period of time yields the formation and dissipation of the conditions that are known to cause significant heavy precipitation in Hong Kong almost every year. The simulations in this thesis are

therefore chosen to start on 5 June 2008 and end at 9 June 2008, simulation 96 hours including three stages of through positioning relative to the urban area: south of the coast, above the urban area and north of the urban area in the dissipation stage.

3.2 Model system

The Weather Research and Forecast model (WRF) is a popular tool for atmospheric research and widely used (refer to Section 2.2.4). The model code and description are available freely in the internet [Skamarock et al., 2008]. This section describes the setting of the model and its parametrization schemes as well as the choice of domain and numerical initial and boundary conditions for the case studies. Details about the model compilation and performance are presented in Appendix A.

3.2.1 Simulation domain

Because WRF uses hybrid coordinates, the so called σ -coordinates in the vertical direction, it is useful to choose the domain and schemes accordingly. When studying urban phenomena in regional context, neighbourhood scales of one square kilometre should be the smallest details concerned. A visualization of the scales in atmospheric processes are illustrated in Figure 3.2 and it becomes visible that kilometre scales are the finest reasonable scales that the model dynamics should be handling. In a typical setting, nesting ratios of three or five should be considered but here five are preferable to avoid 9 kilometre grid spacings, which are problematic for convection scales.

Hence the innermost domain in the nested setting should have a grid spacing of $1 \times 1 \text{ km}^2$. The next consideration is the least amount of area that the model needs to simulate in order to ensure dynamic consistency and representativeness of the physical processes simulated. Because the monsoon trough covers a very

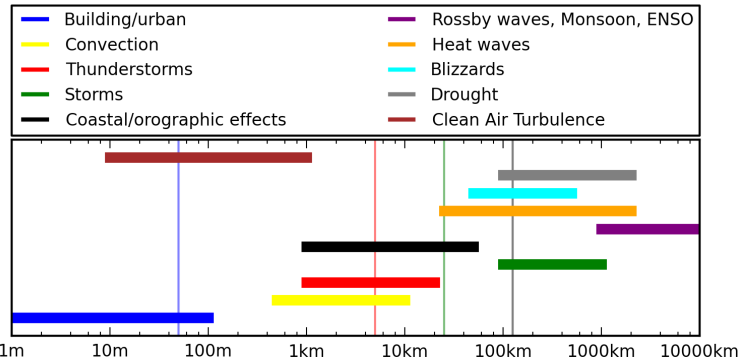


FIGURE 3.2: Scales in atmospheric processes as horizontal bars and typical numerical model grid spacings as vertical lines. The numerics associated are large eddy simulation (blue), numerical weather prediction (red), regional climate models (green) and general circulation models (grey).

large area and the monsoon dynamics depend highly on the Tibetan Plateau, the outermost domain in the model should cover all these areas for dynamic consistency. Special care was applied to the details of the model projection to make sure that the curvature factors over the steep topography of the Tibetan Plateau were not too large to avoid geometric distortions of the flow fields. When telescoping down to the innermost domain, intermediate domains output will not be used for analysis, hence the choice of the middle domain solely depends on the dynamic consistency at the boundary, e.g. no steep edges or sharp gradients at corners and boundaries. In this simulation, two-way nesting is applied, meaning that the information of inner domains overwrites the information in outer domains.

A nesting ratio of 1:5 is applied, hence the middle domain has a grid spacing of $5 \times 5 \text{ km}^2$ and the outermost domain simulates $25 \times 25 \text{ km}^2$. This reduces the "physical grey zones" of scale to the middle domain, where $5 \times 5 \text{ km}^2$ is a spacing in which it is not fully representative to use either no convective parametrization or any of the available convective parametrization schemes. Hence structures like thunderstorms may not be representative in that domain. However, because the innermost domain overwrites the output of the middle domain, this only plays a role in the area where the middle domain is not covered by the innermost domain. Hence, the middle domain should be as small as possible while covering sufficient area to provide adequate boundary conditions for the innermost domain.

Taking the limitations described above into account, the domain is defined as

shown in Figure 3.3. The second domain covers a relatively small area and has a different aspect ratio, in order to provide more information along the coast line, where topography gradient effects are important. The innermost domain is designed to cover the major urban areas of the Pearl River Delta region (see Figure 3.4), while the outermost domain covers the Tibetan plateau, the SCS and parts of the Indian and Pacific Ocean and Japan.

The geometry of the domain has been summarized in Table 3.1. The standard deviations of topography heights are significantly larger than the average. However, the quantity is physically limited to a minimum value of 0, hence the distribution is tilted strongly towards the positive side, indicating large peaks. Hence it is important to point out that none of the domain edges have very steep gradients or large inconsistency across domain borders. This is essential for near-surface processes to remain representative and avoid production of artificial gravity waves.

3.2.2 Initial and lateral boundary conditions

In all the experiments, it is important to produce balanced state soil-moisture fields before initializing the case study, as time scales in soil moisture fluctuations differ from those of atmospheric fluctuations. The National Center of Environmental Prediction (NCEP) Final Reanalysis data (FNL) was used to derive initial and lateral boundary conditions by utilizing the WRF pre-processing software. In order to ensure balanced soil moisture fields, the outermost domain was initialised

Domain	1	2	3
Grid spacing [km ²]	25 × 25	5 × 5	1 × 1
Grid points X×Y	310 × 200	151 × 91	241 × 231
Area [km ²]	38.75 × 10 ⁶	343525	55671
Aspect ratio (Y/X)	0.64	0.60	0.96
Topography height			
Maximum [m]	6454.54	1134.64	1100.38
Average ± std. dev. [m]	567.58 ± 1237.59	73.01 ± 134.57	53.49 ± 96.65

TABLE 3.1: Details of the model domain geometry.

one year before the start of the simulation and spectral nudging [Miguez–Macho et al., 2004] on $1400 \times 1200 \text{ km}^2$ horizontal scales and above was applied to maintain dynamic consistency with the reanalysis data. One could argue that nudging

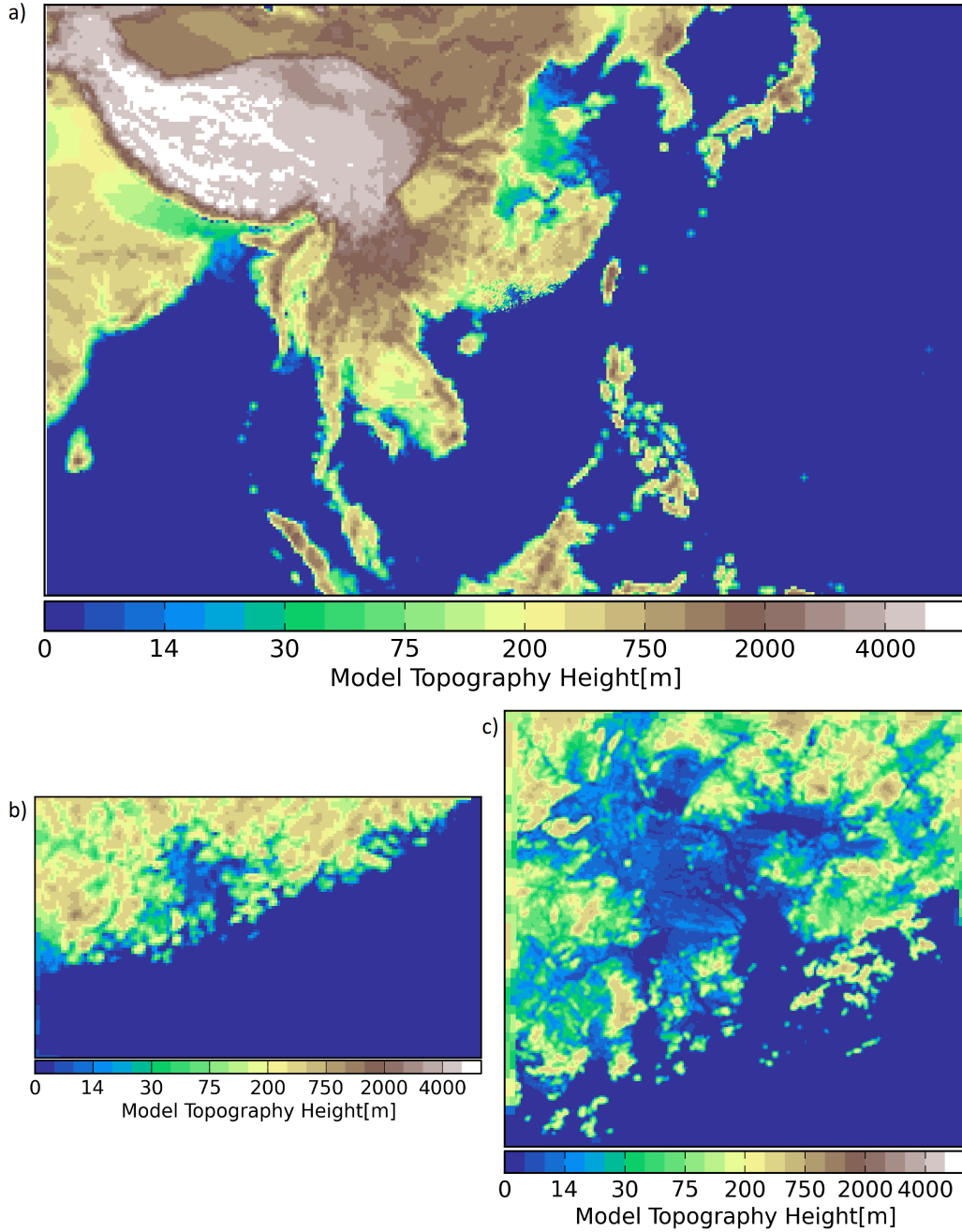


FIGURE 3.3: Model domain topography height in a nested setting. The grid spacings in the daughter domains are following a nesting ratio of 1:5. In Figure (a) the outermost domain D01 is shown with the daughter domains incorporated. (b) and (c) show the nested domains D02 and D03 respectively.

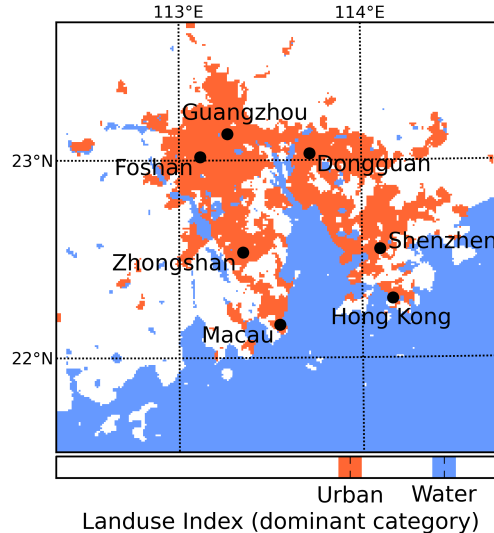


FIGURE 3.4: Urban land cover in the innermost domain shown in red with major cities indicated as dots.

is not necessary for simulation periods of just a few days for the actual case studies, but it is a helpful tool to maintain the location of the low pressure trough throughout different parameter scenarios to ensure comparability of different experiments. The soil moisture and temperature data of the outermost domain are used to initialize the simulations of the case studies and added upon by the actual FNL data in the atmosphere, so that a full set of initialization data is generated. The static lower boundary conditions are taken from the WRF package datasets, where the land use information dataset was derived from the Moderate-resolution Imaging Spectroradiometer (MODIS) satellite's data and made available in the WRF standard package. Note that the dominant land use category (e.g. the red area in Figure 3.4) is not entirely urbanized on every grid point but only indicates locations where the variable $LANDUSEF[urban] > 50\%$. Further details about the implementation of sub-grid-scale tiling in the LSM can be found in the WRF manual. This data was during the course of the experiment modified by applying the United States Geological Survey (USGS) dataset in some parts of the domain, which is significantly older than the MODIS data. The details of these changes will be discussed in the latter part of this chapter (see Section 3.3).

3.2.3 Dynamics and physics

This section provides a summary of the physics packages and dynamic adjustments applied to the WRF model in these case studies to give a reference to the reader for further interpretation of the results and experiment settings.

Table 3.2 shows the schemes chosen for the simulations. It is important to note that the New Arakawa Schubert Scheme (NAS) [Han and Pan, 2011] is only applied in the outermost domain, as in the child domains the convection should be explicitly resolved and two-way nesting assures that the resulting flow features are present in the parent domains. The large-scale spectral nudging approach is also applied exclusively to the outermost domain.

The Rapid Radiative Transfer Model for Global Applications (RRTMG) [Iacono et al., 2008] was chosen for all domains as it allows for random cloud overlap assumptions and seems to be more representative in cases of deep convection, within which multiple layers of clouds interact with each other. The unified NOAH land surface Model (LSM) [Tewari et al., 2004] has been chosen as it has been reported to perform reasonably well with urban canopy layer models available at the time [Kusaka et al., 2004]. The Bougeault-Lacarre scheme [Bougeault and Lacarèrre, 1989] is a Turbulence Kinetic Energy (TKE) prediction scheme that includes advection, shear, buoyancy and dissipation terms, hence is relatively representative on the scales on which the two inner domains focus. It is also expandable to allow for heat sources above the lowest model level, e.g. above 100 m. This is interesting for representing high-rise buildings in urban canopy model anthropogenic heat predictions in further parts of future studies.

In the final experiment set-up, the simple one-layer urban canopy model [Kusaka et al., 2004] is preferred over the fully integrated system because on a fundamental level assumptions are less numerous and less dubious in character (e.g. unavoidable errors by estimation of thickness of individual building components, etc.). Despite individual buildings in Hong Kong exceeding heights of 100 m, choosing the simpler scheme seems to be a sensible choice. In the future, as coherent urban data will become increasingly available, the use of more complex parametrizations like the building environment parametrization and building energy model (BEP-BEM) will

Domain	1	2	3
Radiative Transfer	RRTMG	RRTMG	RRTMG
Convection	NAS	none	none
Spectral Nudging	$1400 \times 1200 \text{ km}^2$	none	none
Land Surface	Unified NOAH LSM	U-NOAH	U-NOAH
Boundary Layer	BouLac	BouLac	BouLac
Cloud physics	WSM6	WSM6	WSM6
Urban Canopy Model	none	Single-layer	Single-layer

TABLE 3.2: Parametrization schemes used in the simulations of this study.

become feasible, which is why the BouLac scheme is the boundary layer scheme focused on in this study.

An element of control to ensure statistical robustness is the use of ensembles. The simplest way of ensuring comparability between different simulation runs is to use identical model settings but initialize the simulation at different times. The statistical behaviour of three and five member ensembles were tested in the preparation stage and it turns out that the difference in statistics is minimal once three members are simulated. As a consequence, the three-member ensemble approach was applied to all case simulations with initialization times that differ by six hours around the simulation start on 5 June 2008 at 00:00 GMT. All simulations in these experiments end at 00:00 GMT on the 9 June 2008, hence a period of four days \pm six hours is simulated for each experimental case.

3.3 Experiment design

The experiments have been divided into three sections as to investigate three different questions that are technically related and build upon each other but differ fundamentally:

1. Whether different human activities in cities can produce changes in local precipitation at all.
2. How large a city needs to be in order to produce its own micro climate effect and whether the size affects fundamental properties of that change.

3. How sensitive the local system is to larger scale changes, for example long term climatic variability trends.

3.3.1 Human activities

Typically, humans interact with their environment by exchanging energy, moisture, particles and momentum. The following paragraphs describe how these properties are affected by humans and which is chosen for the experiment.

Human activities change atmospheric momentum actively (e.g. traffic adding momentum) or passively by building structures and reducing momentum. Examples of momentum exchange are trains generating flows along their tracks or the construction of buildings and structures that change the local surface friction properties. A curious and more complex reported example are wind turbines for energy generation [Roy and Traiteur, 2010] and their downstream effects, but in general every structure affects the local environment.

Particles are mostly introduced through combustion processes as well as friction processes in general, for example road traffic or cooking. The same applies for energy and moisture, but small amounts of energy and moisture are released from the human metabolism itself. Because of entropy, every process that converts any form of energy (e.g. fuels or electricity) has to release at least sensible or latent heat and in case of material consumption (fuels) also particles or discharge (ashes, burnt fuel elements, etc.). Hence, every human activity releases some form of heat and under most conditions some form of particles. Moisture is often released as by-product of cooling facilities, because many open cooling systems (e.g. power plant cooling towers) use water as an agent for it having a large heat capacity and no toxicity.

For the case study in Hong Kong, where moisture and outside air temperatures are high in summer, the impact of sensible heat alone is chosen as a proxy for human activity. The parameter to investigate then becomes the sensible anthropogenic heat flux (AH), i.e. the amount of sensible heat released by human activities. This

heat can be produced by air conditioning, vehicle exhausts and cooking combustion, power generation and electrical appliances in general. Because the outside air temperature is high, the relative importance of human metabolic heat and moisture may be small compared to the other sources, given that the metabolic warm blood temperature is smaller than that of other heat sources (AC units, car engines, etc.).

In the UCM the parameter of AH has a diurnal cycle $\psi(t)$ (see Figure 3.5a) with two peaks to account for rush-hour transportation. Values at daytime are higher than nocturnal values due to business behaviour but do not drop entirely to zero at night because of residential air conditioning. The temporally-scaled AH parameter value is added to the LSM sensible heat flux S_{LSM} , resulting in the total sensible heat flux

$$S = S_{LSM} + AH \times \psi(t) \quad (3.1)$$

such that the effects are propagating from the surface itself. In reality, most of the heat is released above the surface, so thermal roughness effects play a role as well and are taken into account by the PBL scheme. Traditionally, splitting variables into resolved and unresolved scales (Reynolds Average, e.g. $u = \bar{u} + u'$), the TKE \bar{e} equation becomes

$$\frac{\partial \bar{e}}{\partial t} + \frac{\partial}{\partial x_k} \left(\bar{u}_k \bar{e} + \overline{u'_k \bar{e}} - \nu \frac{\partial \bar{e}}{\partial x_k} + \frac{1}{\bar{\rho}} \overline{u'_k p'} \right) = -\overline{u'_k u'_i} \frac{\partial \bar{u}_i}{\partial x_k} + \frac{g}{\bar{\theta}} \overline{u_3' \theta'} - \nu \overline{\left(\frac{\partial u'_i}{\partial x_k} \right)} \quad (3.2)$$

with local tendency term, the divergence of turbulent kinetic energy fluxes and production terms, describing how turbulent kinetic energy behaves in the system. In practice the model equation is cast in σ -coordinates, which then results in

$$\frac{\partial \bar{e}}{\partial t} = -(\delta_{1k} + \delta_{2k}) \left(\bar{u}_k \frac{\partial \bar{e}}{\partial x_k} + \frac{\partial u_k}{\partial x_3} \overline{u'_k u'_3} \right) - \dot{\sigma} \frac{\partial e}{\partial \sigma} - \frac{1}{\rho} \frac{\partial}{\partial x_3} \rho \overline{u_3' e'} + \frac{g}{\Theta} \overline{u_3' \Theta'} - \epsilon \quad (3.3)$$

where following the Einstein summation convention $k, i = 1, 2, 3$ and $x_3 \neq \sigma$, velocities u_k and $\dot{\sigma}$, density ρ , gravitational acceleration g , potential temperature Θ , molecular momentum diffusion coefficient ν and dissipation term ϵ . The equation hence includes advection, shear, buoyancy and dissipation effects. The advection component is important as turbulence decay is scale dependent [Kolmogorov, 1941]

but the advection speed retains its magnitude (when comparing, e.g. 25 with 1 km grid spacings), particularly in very heterogeneous conditions like Hong Kong. The details of the parametrization are rather interesting but will not be technically described in this chapter. The beauty of it lies in its simplicity. One significant benefit of this scheme is the use of buoyancy length scales for the estimation of buoyant freedom of an air parcel, e.g. estimation of mixing heights. Hence effects of steep topography are better represented than in some schemes which are designed for significantly larger scales. This is very important in the context of Hong Kong with its complex and heterogeneous terrain.

With the numerical tools as described above, the final challenge remains to

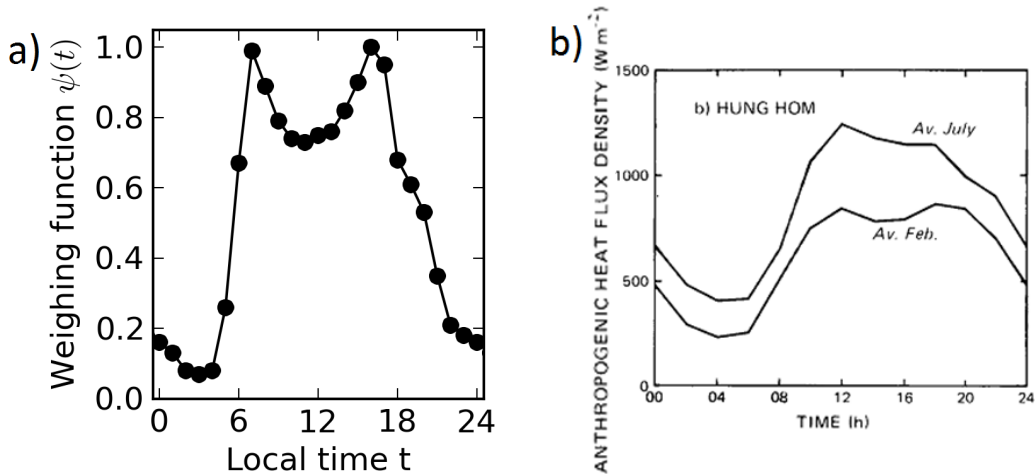


FIGURE 3.5: Comparison of model temporal weighting function $\psi(t)$ for AH value scaling 3.5a and monthly averages of diurnal point measurements of AH in Hung Hom 3.5b [Oke, 1988].

choose reasonable values for AH. It makes sense to compare a zero-AH case with a set of different values that symbolize different degrees of urban activity. Because of the work of Oke [1988] and Allen et al. [2011] a worst-case scenario value of $AH = 1000 \text{ W m}^{-2}$ is chosen. Hence AH will be simulated as $AH \in \{0, 50, 100, 250, 500, 1000\} \text{ W m}^{-2}$. Most interesting are the cases of 250 and 500 W m^{-2} respectively, because the true value most likely lies in between those. It is important to point out that the values presented in the literature appear quite large. Landsberg [1981] (see p. 73, Table 4.15) presents data based on energy consumption per area, which shows very low values for Hong Kong (3 W m^{-2}) and very high values for Manhattan (630 W m^{-2}), which were estimated in the 1970s.

It is hence important to emphasize once again, that the values in this study aim to provide an estimation of the worst possible impact of humans upon local urban micro-climate.

3.3.1.1 An illustrative example of AH estimation

The magnitude of AH appears quite large. To put this into perspective, the energy release in a single residential building is estimated as follows. Assuming that a building has 20 floors and 8 flat units per floor with 3 air conditioning systems each. This gives a total of

$$20 \text{ floors} \times 8 \frac{\text{flats}}{\text{floor}} \times 3 \frac{\text{AC - units}}{\text{flat}} = 480 \text{ AC - units}$$

per building without taking into account central systems for lifts, lobby and other appliances. Note that typical residential buildings are taller in densely populated residential Hong Kong, but of course these do not cover all of the area. If each of the units has a power consumption of 3 kW (e.g. low efficiency cheap in-window-systems that over-cool the air to reduce humidity; medium sized in-window-units have cooling capacities up to 6 kW) and the building covers an area of $70 \times 70 \text{ m}^2$, the energy throughput will be

$$\frac{480 \text{ units} \times 3,000 \frac{\text{W}}{\text{unit}}}{70 \times 70 \text{ m}^2} = 290 \text{ W m}^{-2}.$$

This value is indeed an over-estimation, because the compression ratio of modern AC systems allows for higher efficiency. If one then adds all other constant appliances and central cooling systems for other areas and emissions from busy road traffic, peak values of 500 W m^{-2} are not unreasonable.

3.3.2 Urban spatial extent

The second part of the investigation is to find out whether effects are affected by the size of cities. For this part, the lower boundary conditions are assimilated from two different time slices and data sources as mentioned in Chapter 3.2.2. These represent two different eras or urban development in the region and are visualized in Figure 3.6.

In order to obtain the data for having consistent boundary conditions, the MODIS dataset was used as a reference land use dataset. The urban land use fraction from the reference has been set to zero and replaced by green broad leaf forest (as it is found in pristine areas nearby) in areas, where urban land use fraction is zero in the USGS data. All other parts of the domain remained untouched, hence all areas are assumed to have not been urbanized in the 1980s had been untouched (on kilometre-average) until then. For the practical purpose of estimating how heavy urbanization affects micro climate in a particular area, this approach allows a sufficiently large change to promise interpretable results. Similar to the AH experiment, the sensitivity has been analysed for AH values of 0, 250 and 500 W m⁻². A more detailed presentation of the land use in the simulation domains and a description of how the data was changed is found in Appendix B.

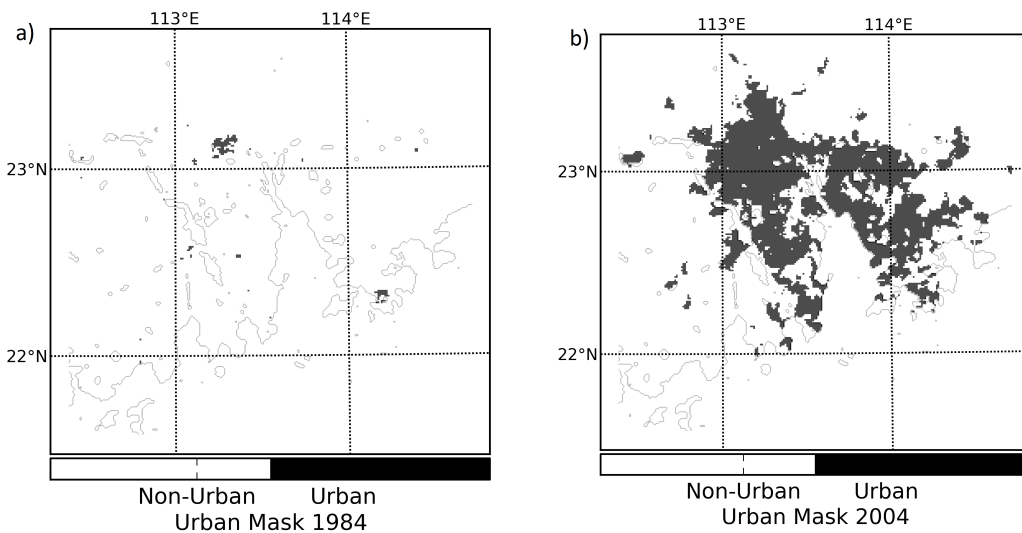


FIGURE 3.6: Urban land use in domain 3 approximately 1984 (USGS data) in (a) and approximately 2004 (MODIS data) in (b).

3.3.3 Large scale variability

The final question to address in this thesis is the sensitivity of the local microclimate to large scale dynamics. Previously climate projection downscaling or pseudo-climate change experiments have been considered.

Downscaling is a method with large uncertainty, because the uncertainty of the embedded model is added to the uncertainty of the climate model. The simulations will hence not be comparable to previous experiments. Pseudo-climate change experiments attempt to spin-up a model with modified forcing data, e.g. increasing model temperature by, for example, one Kelvin. For this investigation it is more practical to modify the moisture. Because the relationship between moisture and temperature changes are complex. According to the Clausius-Clapeyron ratio, an increase of one Kelvin can produce an increase of 6 % in saturation (see Chapter 6), thus precipitation. But in practice, the Clausius-Clapeyron equation describes only one aspect of the entire system, where fluid dynamics describe another major component of the system. Thus the actual effect of increasing temperatures is likely to differ from the theoretical static calculation and investigating the effects of changes in moisture appears to be more direct.

The experiment is carried out by increasing and decreasing the moisture in the forcing and nudging data. Changes of 10 % are introduced to study these scenarios. A change to dryer or wetter background climates can be simulated for the same rainstorm, hence yield comparability to previous simulations. Different vertical levels have different effects and physical significance. Low-level moisture increase yields information about evaporation and local effects, while mid level moisture can be related to advection processes. In these experiments the effects of low and mid level moisture changes are investigated and compared to the effects of local effects caused by AH and urban area changes.

3.4 Brief overview

In this chapter, the experimental tools to investigate the questions summarized in Chapter 2 have been described. In the following Chapters 4, 5 and 6 the results of each of the experiments will be presented and summarized. The effects of each of the modifications described above will be discussed in detail and provide the material for Chapter 7, in which concluding remarks that arise from the results will be presented and suggestions for further studies will be expressed.

Chapter 4

Effects of anthropogenic heat

Anthropogenic heat is one of the parameters to investigate when answering the question, what physical effects a city can exert on local precipitation, for example increases of rainfall as described by Mok et al. [2006]. The main results of this chapter have been published in Holst et al. [2016] and some plots from that publication have been used or replotted in this chapter. The case studied here as mentioned in Chapter 3.1 is a monsoon trough scenario from early June 2008. In this chapter the results of the innermost nested domain with 1-kilometre grid spacing (refer to Figure 3.3) will be discussed.

Before discussing the simulation results, a brief description of the analysis methodology is provided in the following section. Then the details of the simulated precipitation statistical changes are described with focus on different aspects of the statistics. The latter part of this chapter discusses dynamical properties of the flow that could explain the sensitivity of precipitation to the surface heat flux. Finally, a brief summary is presented.

4.1 Quantification of model results

4.1.1 Model precipitation

For this experiment, the rainfall rate was calculated in five minute intervals with a backward differencing scheme, applied to accumulated precipitation as diagnosed by the model micro physics at the surface, e.g.

$$PR1 = (PR[t] - PR[t - 5 \text{ min}]) \times 12$$

where PR is the accumulated precipitation, t is the time, and PR1 is the estimated hourly precipitation rate. The factor of 12 results from the fact that every five minutes, a value is estimated and extrapolated to one hour, e.g. $(60 \text{ min/h})/(5 \text{ min})$.

4.1.2 Statistical parameters

A statistical approach is adopted to assess the effect of AH. For this purpose, grid points that satisfy certain criteria are counted and summed as samples. Such an approach is described below.

4.1.2.1 Domain and sub-domain statistics

The total number of grid points in the domain is $241 \times 231 = 55,671$ for each time step (e.g. $241 \text{ km} \times 231 \text{ km}$). Because the simulations run for 96 h, summing all output time steps yields a sample volume of 64 million, e.g.

$$55,671 \text{ (output)}^{-1} \times 12 \text{ outputs(h)}^{-1} \times 96 \text{ h} = 64,132,992 .$$

This number applies to three ensemble members (please refer to the experiment description in Chapter 3.3), where one member runs for 6 h less and another one 6 h more simulation time, so the total sample volume is then tripled to 192,398,975 samples ($3 \times 64,132,992$).

Moreover, sub-domains (subsets of grid points) can be identified, for example one that only exhibits urban grid points or more precisely grid points with dominant urban model land use. If compared to a domain that is non-urban, different statistics can be evaluated that occur mainly in local urban or local non-urban environments respectively. The visualisation is given in Figure 3.6b, with the urban areas shaded. The urban sub-domain contains 9,200 out of the total 55,671 grid points, hence the urban area covers 17 % of the total simulation domain.

4.1.2.2 Distribution bin values

The value of 0.1 mm h^{-1} is chosen as a threshold to determine, whether a grid point at the surface is experiencing rain or not. The results in these simulations are identical for threshold values between 0.02 mm h^{-1} and 0.7 mm h^{-1} , indicating reasonable numerical signal to noise ratios. The distribution bins have been chosen to be 10, 20, 30, ..., 240 and 250 mm h^{-1} but only values up to 150 mm h^{-1} are shown. The Hong Kong Rainstorm Warning System uses 30, 50 and 70 mm h^{-1} as thresholds for amber, red and black warning signals respectively but the corresponding bins may not be interpreted as such without careful consideration. Each bin contains the threshold value of the upper bound, e.g. for n bins as

$$\text{bin}[k] < PR1[k] \leq \text{bin}[k + 1] \text{ for } k = 0, \dots, n - 1,$$

so that every bin does not include the exact value of its lower bound. In practice this distinction has no significant impact on the results because the exact chosen threshold values rarely occur.

It is important to point out that one will have to establish accumulated distributions if one were to apply these results for the Hong Kong Rainstorm Warning Signal thresholds. The implications towards this warning system will not be discussed in detail here, because it is not in the scope of this study. Further applications may be explored in future studies.

4.1.3 Reference simulation and comparison

It is difficult to know the true value of AH, which most likely behaves in a complex dynamic way (compare, e.g. Allen et al. [2011]), hence the reference value in this study is chosen to be zero. The character of this city is hypothetical because in reality no such city can exist, unless it is an abandoned city without human activities. So the comparison concerns a city's passive physical parameters (for example heat storage capacity or roughness elements) versus its active manifestations of human activities (traffic heat emissions and so on). Each of the simulations is carried out with different values of $AH \in \{0, 50, 100, 250, 500, 1000\} \text{ W m}^{-2}$ (refer to Chapter 3.3.1) and compared to the reference case ($AH = 0$).

4.1.4 Model realism

In order to estimate whether the simulations are sufficiently representative as described in other successful model studies with the same model (see Chapter 2.2.4), we compared the simulation results with radar products and station measurements in Hong Kong. Because the actual station data is not available for open access, only the publicly available radar data will be presented here and statements regarding the quality of the comparison with the station data will be omitted.

In Figure 4.1 the direct comparison of spatial rainfall patterns is presented. Each radar scan takes about 6 minutes of time and the precipitation output of the model is estimated every 5 minutes, hence minor mismatch is to be expected by the difference in timing. In addition, a perfect match should not be expected because of the uncertainty of radar remote sensing products and the limited representativeness of numerical models in general. However, the rain band spanning over Macau in the west and extending towards Hong Kong in the east occurs in both observations and simulations. Furthermore, the larger rain patches in the north centre of the domain slightly south of Guangzhou shows some resemblance as well. Given that these snapshots are computed 36 hours after the model initialization, the degree of comparability of the patterns should be acceptable for our purposes.

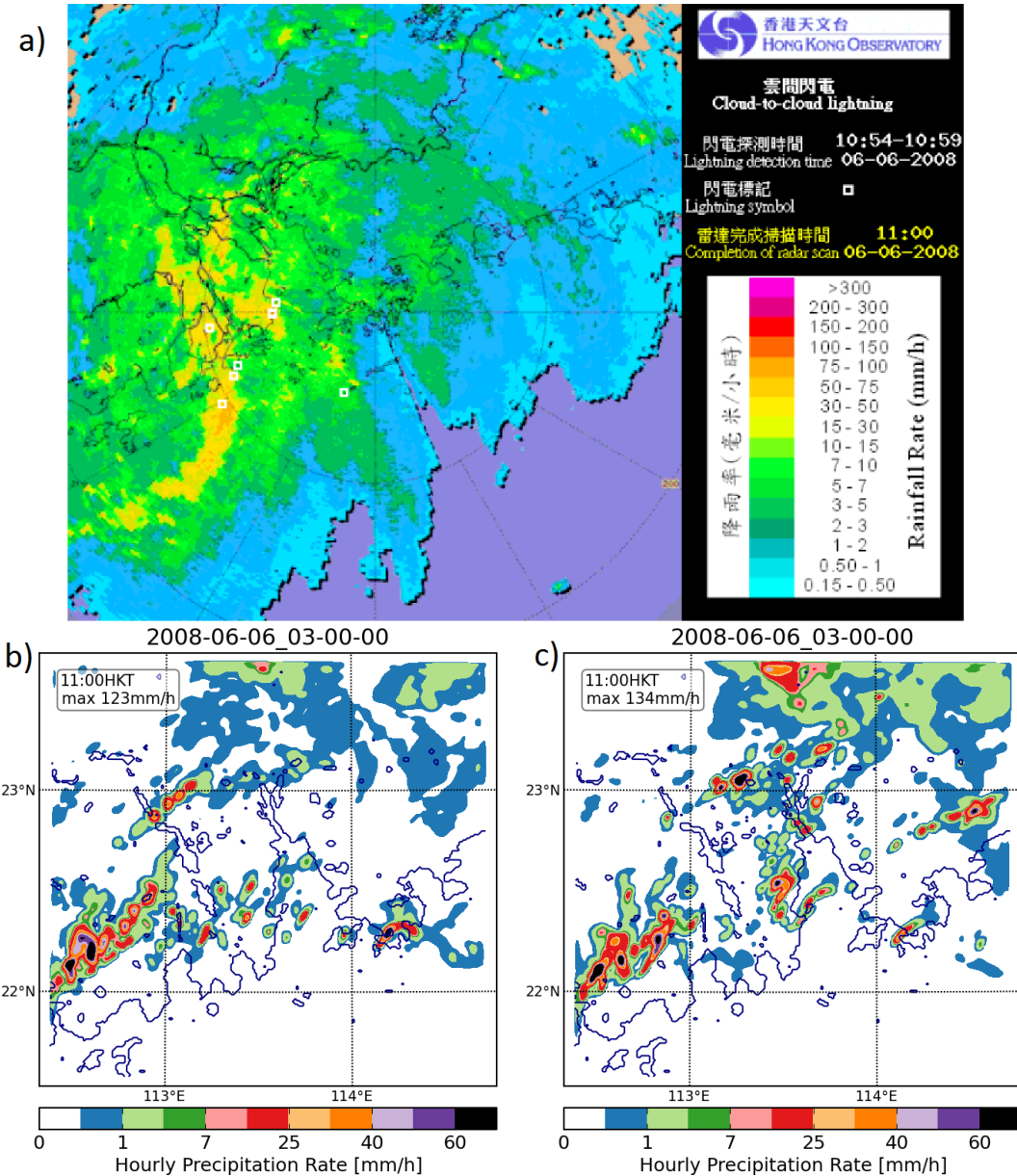


FIGURE 4.1: Radar precipitation estimation product from the Hong Kong Observatory website for 1100 HKT on the 6 June 2008 (a) for comparison with simulated hourly precipitation rates at the same time of incidence for AH = 0 (b) and AH = 500 W m⁻² (c). Adopted from Holst et al. [2016] supplementary materials.

Note that the observed and reported peak intensities during the Hong Kong rainstorms have been found to be mostly within 25 % error of simulated precipitation intensity in the vicinity of the city. Not all individual clouds have been traced and tested but some significant structures like precipitation band structures and convective rain are found to be similar when comparing RADAR products with simulated precipitation. Overall the larger scale structures simulations are closer to observations than convective local phenomena, which is to be expected. For an additional presentation of simulated surface conditions, refer to Appendix D.

4.2 Rainfall sensitivity to anthropogenic heat

When applying the mentioned analysis concepts to the simulations for this study the first step is to interpret the total amount of precipitation throughout the simulation period of 96 hours. The question to be answered is whether the accumulated precipitation is affected by human activities or not.

4.2.1 Accumulated precipitation

The first and simplest comparison is to evaluate the sum of all precipitation that occurs in the simulation results. Note that this is equivalent (except a constant factor) to computing average daily or hourly precipitation rates throughout the entire 96 hours of simulation period. Note, that all ensemble members were initialized in balanced states (commonly used in numerical weather prediction problems) to reduce spin-up effects. During the first 5 hours of each simulation, no precipitation rates larger than 1 mm h^{-1} were detected. This indicates that the statistics shown in this Chapter are largely unaffected by spin-up effects. Table 4.1 compares the total accumulated precipitation within the entire domain with those in the urban and non-urban parts. An increase of accumulated precipitation by up to 33 % is found for the entire domain when $\text{AH} = 1 \text{ kW m}^{-2}$, although the increase does

AH [W m ⁻²]	Total accumulated precipitation throughout domain [m]					
	Domain [mm]	Δ_{0AH}	Urban [%]	Δ_{0AH}	Non Urban [%]	Δ_{0AH}
0	62,355		10.6		89.4	
50	74,185	+19.0 %	13.0	+45.8 %	87.0	+15.8 %
100	64,806	+3.9 %	13.3	+30.5 %	86.7	+0.8 %
500	79,579	+27.6 %	18.0	+115.9 %	82.0	+17.1 %
1000	83,080	+33.2 %	24.7	+210.2 %	75.3	+12.2 %

TABLE 4.1: Total amount of accumulated precipitation for the entire domain, the urban and non-urban sub-domains for different values of AH. The increase relative to zero AH depicted as Δ_{0AH} .

not appear to be monotonic with AH. In addition, most of this increase occurs in the urban sub-domain, where an increase of up to 210% is found. The non-urban part of the domain appears to undergo an unsystematic increase compared with the reference simulation, but no clear interpretations can be drawn from this data alone. Hence, another degree of complexity is added to the analysis by examining the spatial pattern of accumulated precipitation in the different simulations.

The spatial behaviour of accumulated precipitation for different values of AH (Figure 4.2) can be compared with the urban coverage in Figure 3.6b to assess how (on average) the precipitation patterns in the simulation depend on human activity. In the cases of low heat release (AH being 50 – 250 W m⁻²), the wet areas remain down- and upstream of the cities but also show higher values in the area where the city is present (Figure 4.2(a–d)). A larger urban-rural difference is found for larger values of AH, e.g. 500 and 1000 W m⁻² (Figure 4.2(e, f)), showing increasingly wet urban areas in these simulations, while rural areas appear to be less affected. The large urban accumulation near 23° N latitude shows increased clustering for the large AH values, corresponding to the areas around Foshan, Guangzhou and Dongguan.

Figure 4.3 illustrates how these differences in accumulation occur by comparing simulated 5-minute snapshots of the hourly precipitation rate for AH = 0 and AH = 500 W m⁻². The snapshots in 4.3 show two different time slices from the simulation output in direct comparison. While the highest precipitation rates occur in the vicinity of Macau in the AH = 0 simulation in Figure 4.3 panel b), the corresponding AH = 500 W m⁻² simulation shows an increased occurrence of

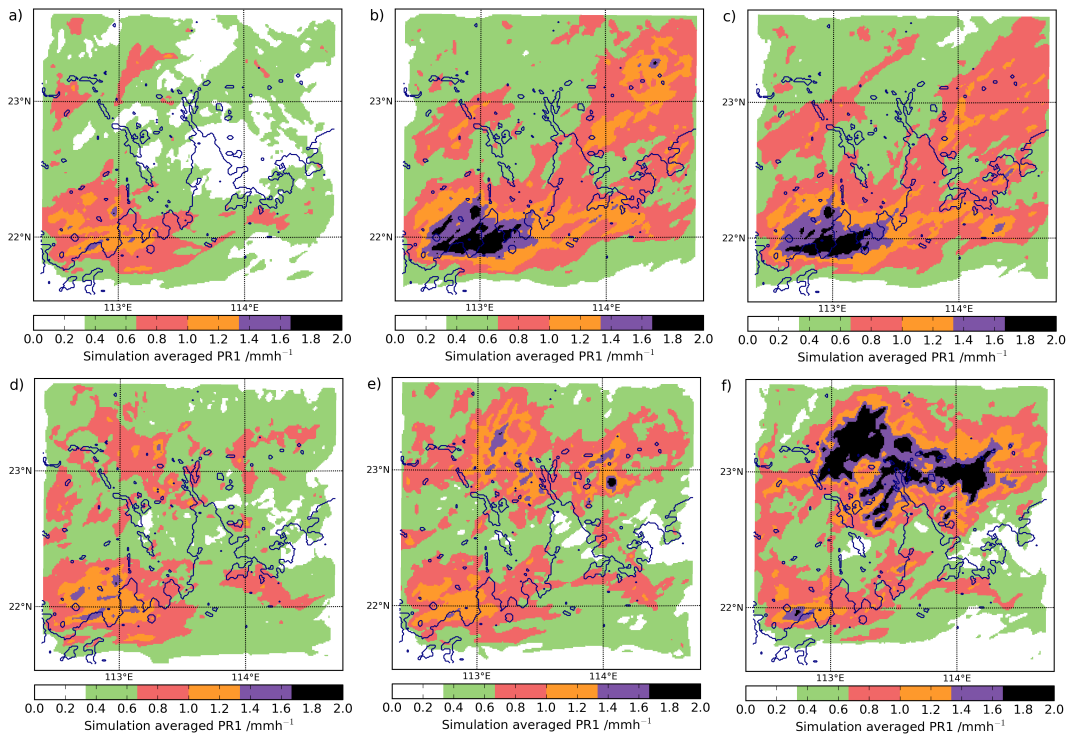


FIGURE 4.2: Comparison of accumulated rainfall divided by simulation time (i.e. simulation average) for different AH scenarios: (a) 0 W m^{-2} , (b) 50 W m^{-2} , (c) 100 W m^{-2} , (d) 250 W m^{-2} , (e) 500 W m^{-2} and (f) 5 kW m^{-2} . Units: mm h^{-1} .

inland precipitation, around 23° N (Figure 4.3c). The maximum intensity of the inland precipitation matches that of the rain band near Macau. In panel b) and d) the difference of clustering becomes more obvious with an increase in size and intensity of the rain band in the north western part of the domain and a slight southward shift towards the urban area in the $\text{AH} = 500 \text{ W m}^{-2}$ simulation.

4.2.2 Statistics of raining grid points

To quantify the simulated difference of occurrence of precipitation throughout urban and non-urban parts of the domain, the differences in counts of rainy grid points are calculated (Table 4.2). This number of wet grid points can be interpreted as the area covered and time spanned by precipitation in the domain.

The number of raining grid points appears to have a slight increase for all cases in which $\text{AH} \neq 0$, but no consistent dependency on AH is found in the domain as well

as in the non-urban sub-domain. In the urban sub-domain however, the increase scales from 11.3 % to 25.4 % and appears to be monotonic for $AH \geq 100 \text{ W m}^{-2}$.

This result illustrates that an increase of 25.4 % in likelihood of rain occurrence is accompanied by an increase of accumulated precipitation of 210 % (see Table 4.1). Hence the simulated rain in the urban area must have increased in intensity.

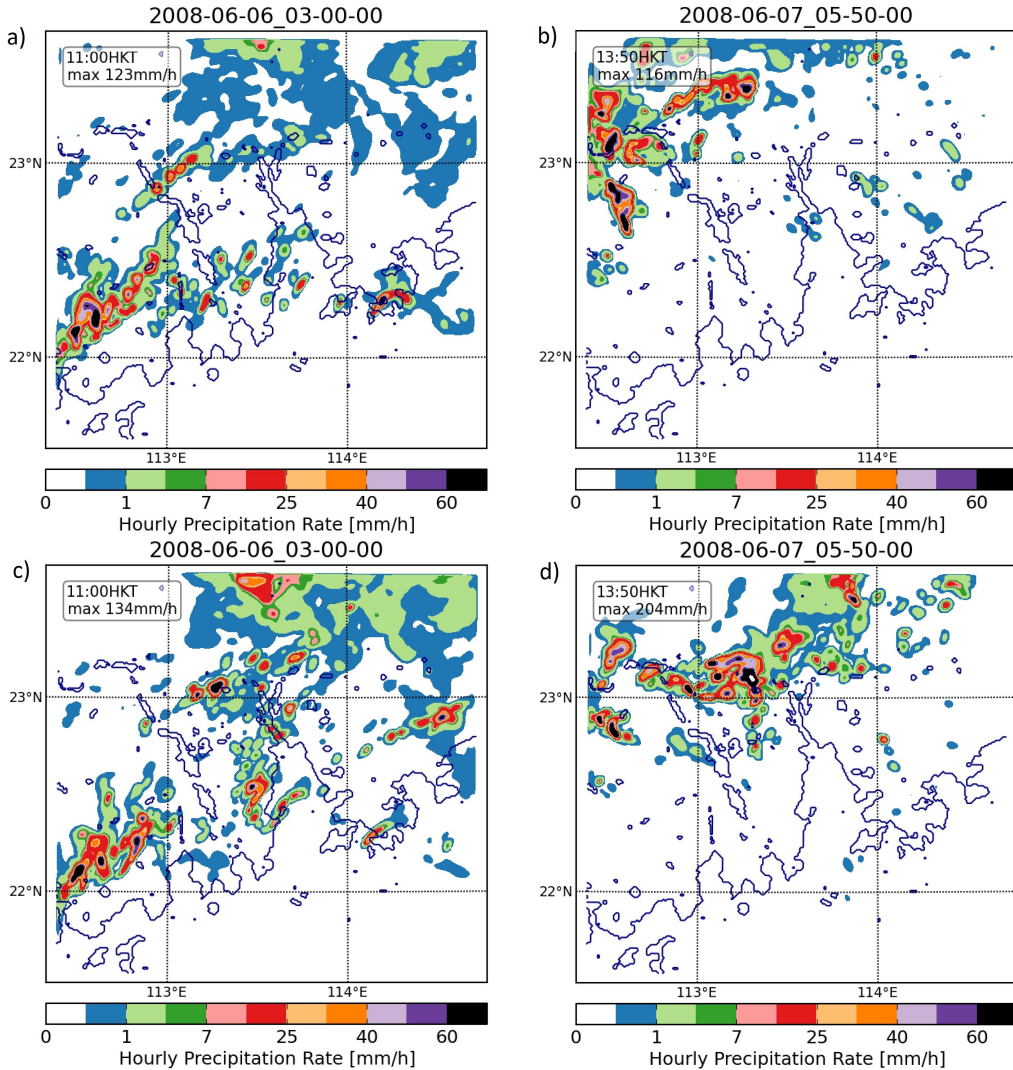


FIGURE 4.3: Snapshots of hourly precipitation rate values at (a, c) 1100 Hong Kong time on 6 June 2008 and (b, d) 1300 Hong Kong time on 7 June 2008, for $AH = 0$ (a, b) and $AH = 500 \text{ W m}^{-2}$ (c, d) model experiments. Unit: mm h^{-1} .
Replotted from Holst et al. [2016].

Total precipitating grid points throughout domain						
AH [W m ⁻²]	Domain [Number]	Δ_{0AH}	Urban [%]	Δ_{0AH}	Non Urban [%]	Δ_{0AH}
0	7,933,106		16.1		83.9	
50	8,712,676	+ 9.8 %	16.3	+11.3 %	83.7	+ 9.5 %
100	8,432,314	+ 6.3 %	16.8	+11.1 %	83.2	+ 5.4 %
500	9,000,400	+13.5 %	16.9	+18.9 %	83.1	+12.4 %
1000	8,625,845	+ 8.7 %	18.5	+25.4 %	81.5	+ 5.5 %

TABLE 4.2: As in Table 4.1 except for the number of precipitating grid points.

4.2.3 Simulated precipitation intensity

The change of precipitation intensity can be studied further by examining its probability density function (*PDF*). Note that the term probability density function may not be appropriate in this case, as the function itself is not quantified in the form of a formula but rather plotted and compared graphically among different AH values which show the likelihood of occurrence, i.e. the number of grid points within the bin divided by the total number of grid points in the respective sub-domain, e.g.:

$$PDF(bin) = \frac{count(bin)}{count(domain)}, \quad (4.1)$$

where $count(x)$ is a function that evaluates the number of grid points that fulfil the condition x . The counting method is described in Chapter 4.1.2. These bins therefore show the likelihood of simulating precipitation rates within the bin for this case.

In addition to showing the PDF alone, the direct comparison of the bins of different AH scenarios can directly show the sensitivity of the model precipitation as a function of hourly precipitation rate and AH.

Differences between urban and non-urban parts of the domain can clearly be seen from the PDFs shown in Figure 4.4. The sensitivity in the urban parts increases with intensity but undergoes unsystematic behaviour in the non-urban sub-domain. This difference can be expected because the changes to the bottom boundary conditions have been applied in the urban part of the domain only (changing only the parameter proxy for human activities in urban grid points).

For AH-values between 250 and 500 W m⁻², the likelihood of hourly urban precipitation rates of 100 mm h⁻¹ is doubled compared to the zero-AH scenario. This corresponds with the observed halving of the return period of this type of precipitation throughout the past half century as described by Wong et al. [2010]. So if human activities were the only cause affecting precipitation in the region, then the true value of AH could hypothetically range between 250 and 500 W m⁻². In reality this is a drastic over-simplification, because the spatial extent of urban areas has changed and these cities have emitted heat in the past as well.

The absolute values of simulated likelihood remain low which is to be expected when analysing statistical extreme conditions. The bins from 0 to 10 mm h⁻¹ have not been presented because the values of likelihood are much larger than the extremes. In addition, the dangers of heavy precipitation are far greater than those of prolonged weak precipitation (e.g. flash flood, landslide, etc.) and hence no further discussion of low precipitation rates will be made in this thesis.

Another interesting feature is the low sensitivity for low values of AH, e.g. less than 100 W m⁻². This indicates that certain amount of energy is required to modify the stability of the atmosphere to a significant extent that precipitation is affected.

Heavy rain appears to be most affected by AH as seen in Figure 4.4. In order to explain the process by which this happens, an investigation of the simulated convection is necessary, as the heaviest rain is produced through convection. Convection however is affected by the surface processes that transport heat and moisture into the higher atmospheric levels. This will be the subject of the coming sub-section.

4.2.4 The role of buoyancy and shear

The behaviour of buoyancy and shear in the simulations is significant to the production of convection. It is well known that vertical velocities yield a good proxy for precipitation, but through the coupling of dynamic land surfaces with atmospheric dynamics, surface energy fluxes do not directly translate into vertical velocities but rather more complex dynamical structures.

In order to demonstrate the role of small scales in these phenomena, turbulence kinetic energy \bar{e} and its production are used as proxies for convective activity. The number of changes between buoyant and stably stratified conditions in the flow can be interpreted as proxy for convective activity. Analysing only local values (e.g. single grid points in the vertical domain) can be misleading because high changing rates could indicate gravity waves. If, however vertically-averaged throughout the boundary layer, the change of the entire layer can be quantified.

To quantify the convective activity in the domain, the Richardson Flux number is calculated, the ratio of buoyant- and shear-production of turbulent kinetic energy, e.g.

$$Rif = \frac{\beta \bar{w}' \Theta'}{\frac{\partial \bar{u}}{\partial z} \bar{w}' u' + \frac{\partial \bar{v}}{\partial z} \bar{w}' v'} \quad (4.2)$$

with the buoyancy coefficient $\beta = \frac{g}{\Theta_v}$, model velocities \bar{u}, \bar{v} , their fluctuations u', v', w' as well as temperature fluctuations Θ' . In addition, the turbulence kinetic energy itself can provide hints on the importance of mixing.

To investigate convective activity, one can either analyse the full distribution of the time-derivative of \bar{e} or instead settle with the standard deviation as a measure of variance. In this analysis, the phenomena of interest move upward from the ground, hence the vertical average in the boundary layer (e.g. a layer between $z=0$ and $z=H$ for a boundary layer height H) of \bar{e} and Rif is calculated for each time step and analysed by calculating the standard deviation in the time dimension, e.g.

$$\sigma_t(Rif_{PBL}(x, y, t))(x, y) = \sigma_t \left(\frac{1}{H} \int_0^H Rif(x, y, z, t) dz \right). \quad (4.3)$$

The height of the boundary layer in this case is chosen to be the height of 12 vertical levels (roughly 2700 m) from the surface to retain comparability between different model simulations. So two elements of convection are presented: the rate at which moisture and energy are mixed within the boundary layer and the rate at which the mixed layer turns from shear-flow into buoyant flow and vice versa. The result of the standard deviations are two dimensional sets of data are useful to compare between different AH scenarios. Figure 4.5 illustrates such a comparison for standard deviations of the 500 W m^{-2} divided by those of the 0 AH case. Larger values show relative increases of the standard deviation, e.g. the width of

the distribution increases, while values close to unity show unsystematic behaviour or no changes.

The relatively noisy character of the ratio plotted can be attributed to the nature of statistical analysis of this data and their direct comparison (e.g. spatial shifts of features causing phase shifts, wave-like structures, etc.). To reduce the noise seen in Figure 4.5, one can apply narrow two dimensional median filters or similar tools. Despite this noise, there is some resemblance between the plots in Figure 4.5 and the urban outlines in Figure 3.6b. Hence it appears as if the increased urban surface heat flux manifests in increased buoyancy and turbulence generation which then affects convection and precipitation as described above. The highest increases here are about twofold for *Rif* and threefold for \bar{e} , indicating that the effect on the mixing and convective activity are large.

4.3 Brief summary

In this chapter the simulated sensitivity of precipitation to anthropogenic heat flux is shown to increase with increasing rainfall intensity. A likelihood-doubling of urban hourly precipitation rates 100 mm h^{-1} in the simulations is found for AH between 250 and 500 W m^{-2} , which is probably the range of the true value. The effect mainly manifests over urban parts of the model domain and for relatively large values of AH.

Implicit simulation evidence for the production of convection through buoyant turbulence generation and associated mixing of heat and moisture is presented. When comparing the $\text{AH} = 500 \text{ W m}^{-2}$ simulation with that of the reference, the time standard deviation of PBL Richardson flux numbers and turbulence kinetic energy are found to double (*Rif*) and triple (\bar{e}) respectively over urban area. Hence the local atmospheric stability in the model simulations could be affected by simulated human activities at the surface, if these activities are sufficiently intense.

Stull [1976] stated that the relative importance of surface-heat for the growth of convective mixed layers (so called encroachment) is $\mathcal{O}(70 - 90\%)$ with vertical

mixing at mixed-layer tops (entrainment) explaining the remaining 30 %. Recently, Sühring et al. [2014] described how the magnitude and size of heat-releasing surface structures increased these processes depending on the amount of energy released. The findings of this chapter appear to agree with their conclusion.

This would explain why there could be different trends in urban and rural Hong Kong [Wong et al., 2010]. However, humans have emitted heat in 1950 as well and in addition the urban areal extent has changed drastically over the past 50 years in the region, so in the next chapter this change and its effects on the sensitivity discussed here will be further analysed.

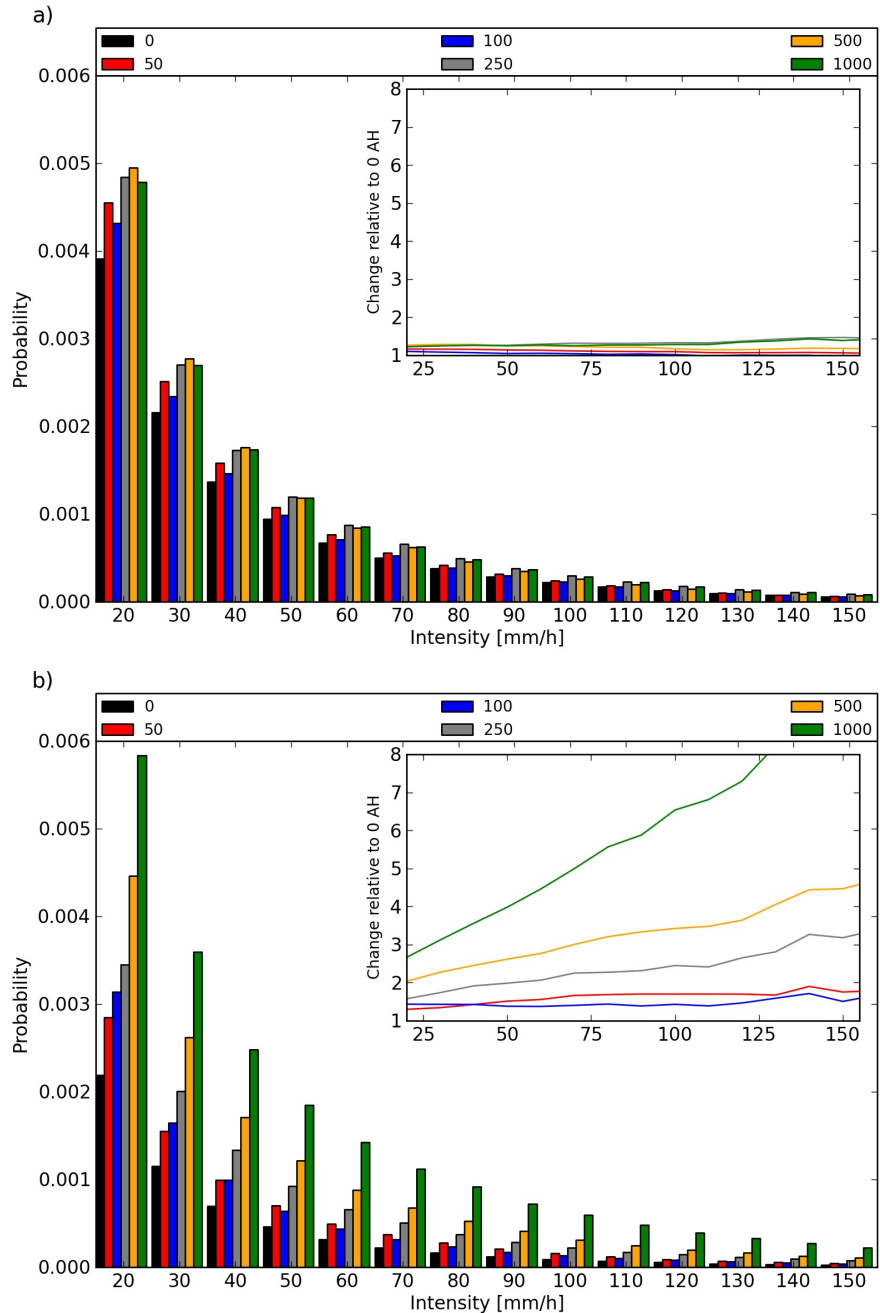


FIGURE 4.4: Simulated relative occurrence likelihood of different precipitation intensity bands in the non-urban (a) and urban (b) parts of the domain for different values of AH. The insets illustrate the change of each experiment with a different AH value relative to the reference case without AH forcing. The colours of the bars and lines indicate the different values of AH [W m^{-2}] as labelled on the top of each figure. Adopted from Holst et al. [2016].

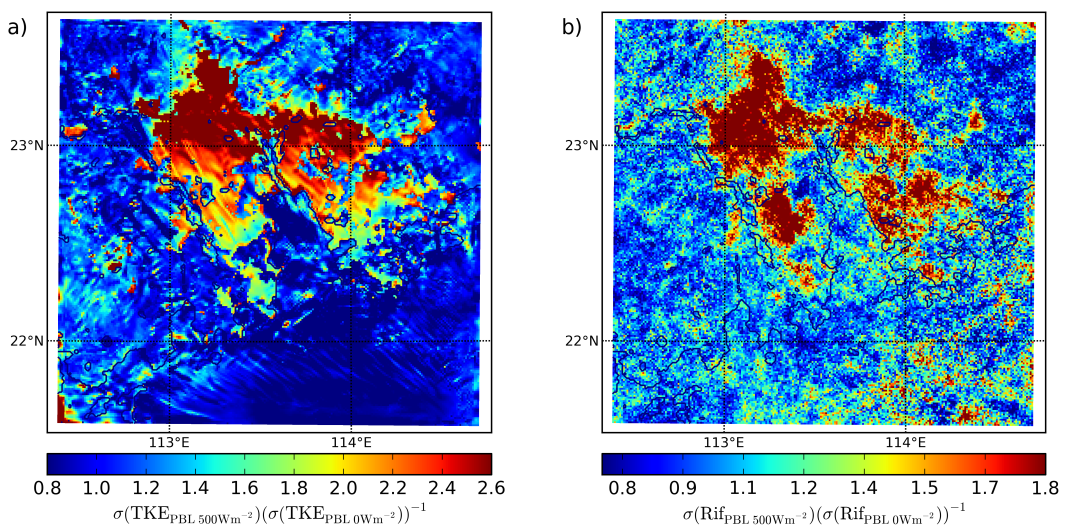


FIGURE 4.5: The ratio (500AH : 0AH) of standard deviations of PBL-averaged \bar{e} in (a) and Rif in (b). Adopted from Holst et al. [2016].

Chapter 5

Effects of urban spatial extent

As discussed in Chapter 4, the intensity of human activities in the region, as represented by anthropogenic sensible heat flux at the surface, can affect the convection and hence the precipitation by shifting the pattern and enhancing the precipitation intensity. This chapter will consider the question of whether this effect would produce similar manifestations if the urban area had not increased in the past three decades.

To retain comparability between all the experiments, the model setting is as close to that used for the experiments in Chapter 4 as possible. More precisely, the only aspect to be changed is the spatial extent of urban land use in the bottom boundary conditions for the simulations. Areas that are not urban are set to be broad leaf forest as observed in the pristine environments in this region. More technical details of how this is implemented are described in Chapter 3.3.2 and Appendix B.

Because the detailed mechanisms of the sensitivity to AH has been described in Chapter 4, only the differences to this sensitivity in the case of different urban extent will be presented here.

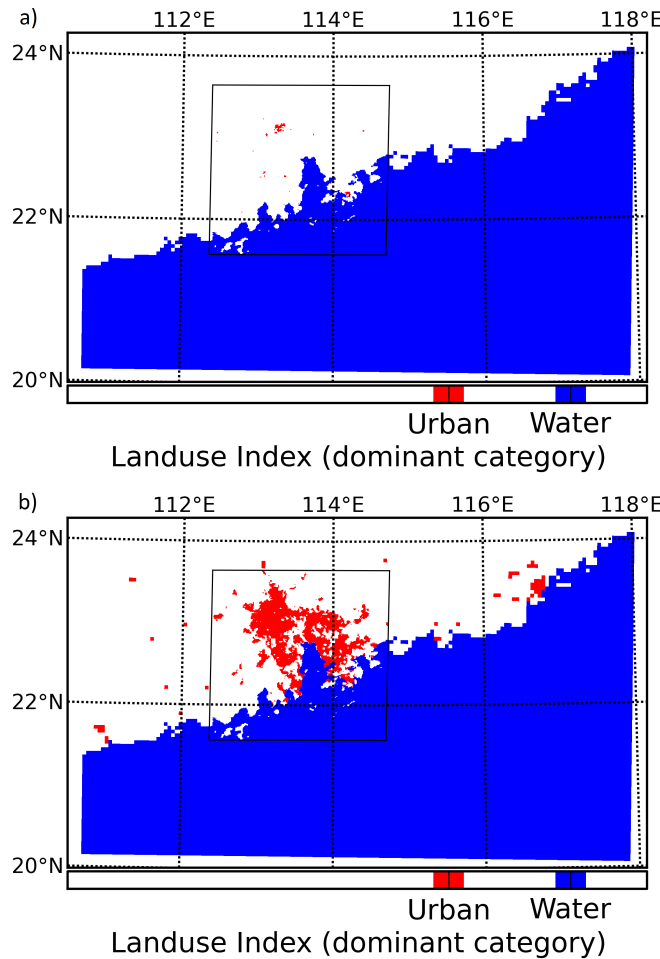


FIGURE 5.1: Model urban extent in 1984 (a) and 2004 (b). The plot shows domain 2 ($5 \times 5 \text{ km}^2$ grid spacing) and embedded in the box domain 3 ($1 \times 1 \text{ km}^2$ grid spacing).

5.1 Sampling area

The two approaches to sampling the model results analogous to Chapter 4.1.2. The two urban extents here are labelled as "1984" and "2004" respectively (Figure 5.1), with the model urban area in the 1984 scenario having only 171 grid points, but 9200 in the 2004 data, giving an urban growth of factor 50 within 20 years, a very large change to the local environment.

5.1.1 Interpretation of different sampling areas

It is important to point out the interpretations when sampling in the "1984 urban" sub-domain are different from those when sampling in the "2004 urban" sub-domain. Consider two examples as follows to illustrate the differences.

5.1.1.1 Stationary local data in "urban 1984"

Assuming that for example in Guangzhou an observatory would have been set up in 1980, then the observations at this point in time and space would be representative for this point in time and space. However, if the city expanded to "urban 2004" and the sampling would be carried out as in "urban 1984", then the regional changes can affect the locally sampled results.

5.1.1.2 Regional data in "urban 2004"

If one samples in the area "urban 2004" but actual urban effects (e.g. urban land use in the model) are only simulated in the area "urban 1984", then the results represent a regional impact of the small urban area. When then comparing to the larger city as in "urban 2004", the comparison can be made what changes the region can expect through complete urbanization of itself.

Because of this distinction, the PDFs and sensitivity tests are presented for both sampling areas. The interpretations are then presented separately and a more complete description is provided.

5.2 Precipitation intensity

The physics of the problem affect the expected results in accordance with the conservation of energy. If the surface heat flux in the AH experiment was partially converted into convection, then forcing the model with the same amount of heat in a smaller area is expected to produce less convection, because the total amount

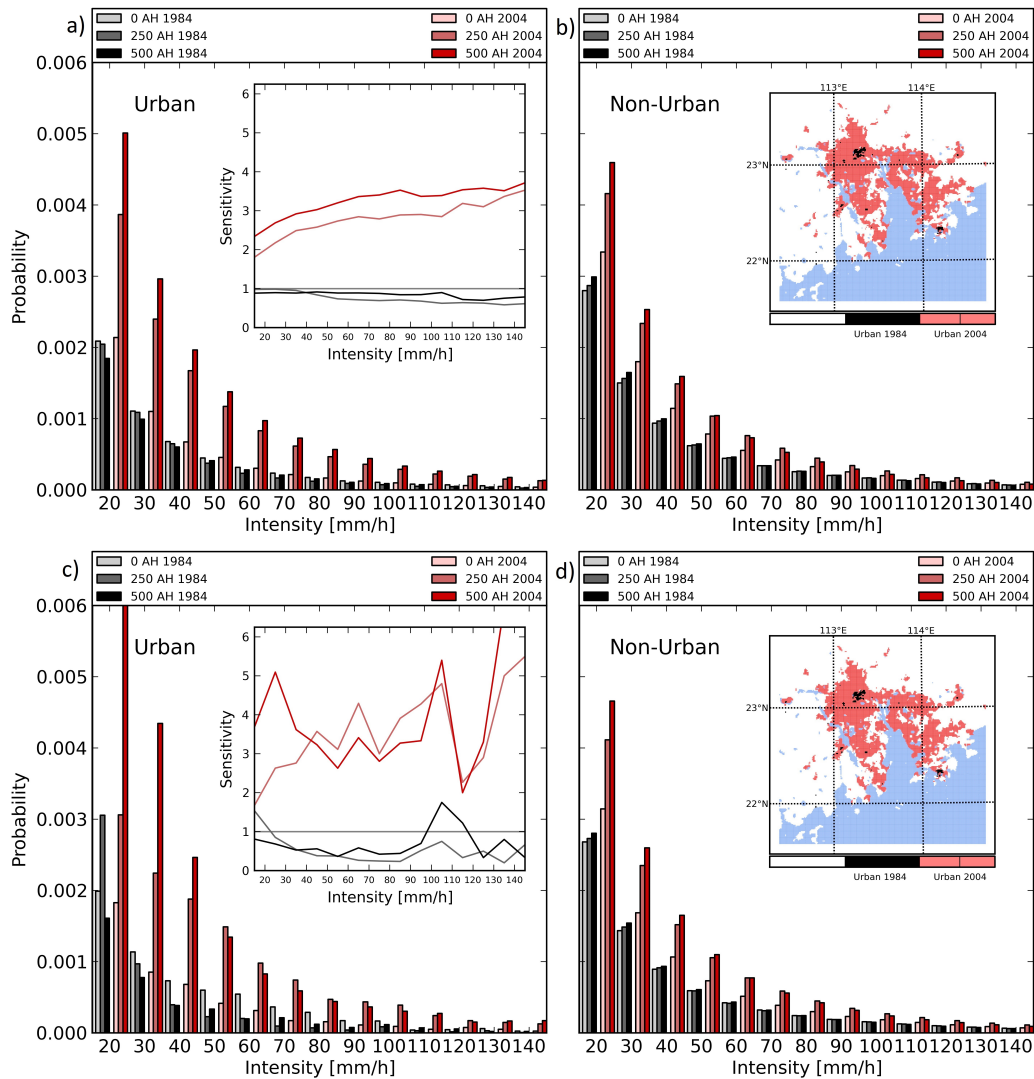


FIGURE 5.2: PDF histogram and sensitivity plots as insets for different sampling areas ((a, b): “urban 2004” and (c, d): “urban 1984”) and different AH forcing values and areas. Areas and lines in grey/black shades refer to forcing with “1984” urban extent while red shades refer to the respective “2004” extent. The shadings indicate magnitude of the AH parameter’s values of 0 (reference case), 250 and 500 W m^{-2} as in the legend on the top of each panel. For clarity the areas are shown in the insets on the right side with matching colours.

of energy released is proportional to the area.

This selection has been based on the results of Chapter 4, showing that the sensitivity of precipitation to AH is increasing for increasing values $\text{AH} \geq 250 \text{ W m}^{-2}$.

5.2.1 Sensitivity in the region ("urban 2004")

The inset of Figure 5.2a shows that the AH-sensitivity of precipitation is non-existent and even inverted for the case of "urban 1984" anthropogenic heat flux forcing area (grey and black line). The region would hence have experienced a decrease of heavy rainfall by up to 40 %. But the effect does not appear to scale with AH. When comparing the urban results with the non-urban results (compare the grey bars in Figure 5.2b), the non-urban precipitation appears to increase with AH for low precipitation rates, plateau at 70 mm h^{-1} and decrease at higher values. Following the reasoning in Chapter 4, it appears that the triggering of convection is either diminished or advected by the mean flow over smaller urban areas as compared to larger urban areas.

The sensitivity of the "urban 2004" anthropogenic heat forcing is identical to that described in Chapter 4, so will not be discussed further here.

5.2.2 Sensitivity in the old city ("urban 1984")

Although the statistics and sensitivity in the black area in the right inset of Figure 5.2d the general features of the PDF are similar to those in Figure 5.2(a, b), there is a number of interesting differences. Most obviously, the curves are far less smooth. The reason for this is the limited amount of samples if investigating the urban area that is 50 times smaller than that shown in Figure 5.2(a, b). The grey lines and bars (e.g. "urban 1984" AH forcing) show a larger diminishing of urban heavy rainfall, however there is a local maximum at $\text{PR1} = 110 \text{ mm h}^{-1}$, indicating that a local rainstorm may have occurred in the data, which has not occurred in the other simulations.

The more notable features are the large increases of simulated rainfall for the red lines ("urban 2004" AH forcing) that exceed those of the corresponding lines in Figure 5.2a. The interpretation is that heavy rainfall is largely affected by the surface energy release in the surrounding region.

Experiment	Domain	Δ_{0AH}	Urban ₂₀₀₄	Δ_{0AH}	%		
2004 0	5217740		552194		10,6		
2004 250	6591060	+26 %	980384	+77 %	14.9		
2004 500	6651920	+28 %	1192300	+115 %	14.9		
			Urban ₁₉₈₄	Δ_{0AH}	%		
2004 0			8746		0.2		
2004 250			19157	+119 %	0.3		
2004 500			25048	+186 %	0.4		
Experiment	Domain	Δ_{0AH}	Δ_{2004}	Urban ₂₀₀₄	Δ_{0AH}	%	Δ_{2004}
1984 0	4754170		-8 %	533122		11,2	-3 %
1984 250	4724820	-1 %	-28 %	463940	-13 %	9.8	-53 %
1984 500	4767960	0 %	-28 %	482650	-10 %	10.1	-59 %
			Urban ₁₉₈₄	Δ_{0AH}	%	Δ_{2004}	
1984 0			9840		0.2	+13 %	
1984 250			8295	-16 %	0.2	-57 %	
1984 500			8357	-15 %	0.2	-67 %	

TABLE 5.1: Accumulated rainfall for different experiments "1984 AH" and "2004 AH" indicating the boundary conditions. Urban₁₉₈₄ and Urban₂₀₀₄ refer to the sampling areas. 0, 250 and 500 W m⁻² are the values of the AH parameter in the simulations. The relative change between "1984" and "2004" AH forcing areas is indicated as Δ_{2004} and for each of the cases the sensitivity to AH is given as Δ_{0AH} .

5.2.3 Amount and occurrence of rainfall

A quantitative evaluation of the PDFs is given in Table 5.1. In addition, Table 5.2 provides the grid point counting statistics (similar to Chapter 4).

As described in the previous subsection, an increase of urban precipitation can be obtained for human activities in larger areas, while a decrease can be obtained for the similar analysis when heat is added to the model land surface on a smaller area. Furthermore, Table 5.2 shows that the likelihood of rainfall is also increased in the urban 1984 scenario, e.g. less occurrence throughout the simulation.

5.2.4 Interpretation

The equivalent potential temperature Θ_e and its changes are computed and evaluated over the domain explaining the statistical results. A detailed description of

Experiment	Domain	Δ_{0AH}	Urban ₂₀₀₄	Δ_{0AH}	%		
2004 0	7133358		1245425		17.5		
2004 250	8060126	+16 %	1347945	+8 %	16.7		
2004 500	8154511	+17 %	1451740	+17 %	17.8		
			Urban _{old}	Δ_{0AH}	%		
2004 0			19945		0.3		
2004 250			22241	+12 %	0.3		
2004 500			25492	+28 %	0.3		
Experiment	Domain	Δ_{0AH}	Δ_{2004}	Urban ₂₀₀₄	Δ_{0AH}	%	Δ_{2004}
1984 0	6951555		-3 %	1144600		16.5	-8 %
1984 250	7047865	+1 %	-13 %	1139974	-0 %	16.2	-15 %
1984 500	6951908	0 %	-15 %	1119751	-2 %	16.1	-23 %
			Urban ₁₉₈₄	Δ_{0AH}	%	Δ_{2004}	
1984 0			17840		0.3	-11 %	
1984 250			18517	+4 %	0.3	-17 %	
1984 500			20121	+13 %	0.3	-27 %	

TABLE 5.2: As in Table 5.1, except for the occurrence of rainfall in grid points.

the methodology used to calculate Θ_e is given in Appendix C.

In Chapter 4, the Richardson flux number as well as turbulent kinetic energy standard deviation have been analysed in the boundary layer. When applying the methodology to Θ_e in this section however, the comparison of the standard deviation alone is insufficient and the average equivalent potential temperature gradient needs to be compared as well. Furthermore, the lowest 20 model levels (i.e. 1000 – 590 hPa) are used to evaluate the stability of the lower troposphere instead of just the boundary layer. This ensures that the tropospheric region in which stratiform precipitation is forming through rising motion in the study area is covered by the statistical evaluation. Note that the stability should mostly affect precipitation caused through low-level moisture convergence. Moist advection in mid- and upper levels and mixing into warm air masses locally are processes that are known to cause thunderstorms and in some regions of the US even tornadoes. In this study the main scope are local effects.

In order to identify the changes in stability, the vertical gradient $\nabla_z \Theta_e$ has been computed for every point in the model atmosphere within the lowest 20 model layers and every 5 minutes for 96 simulated hours. Then the average and standard

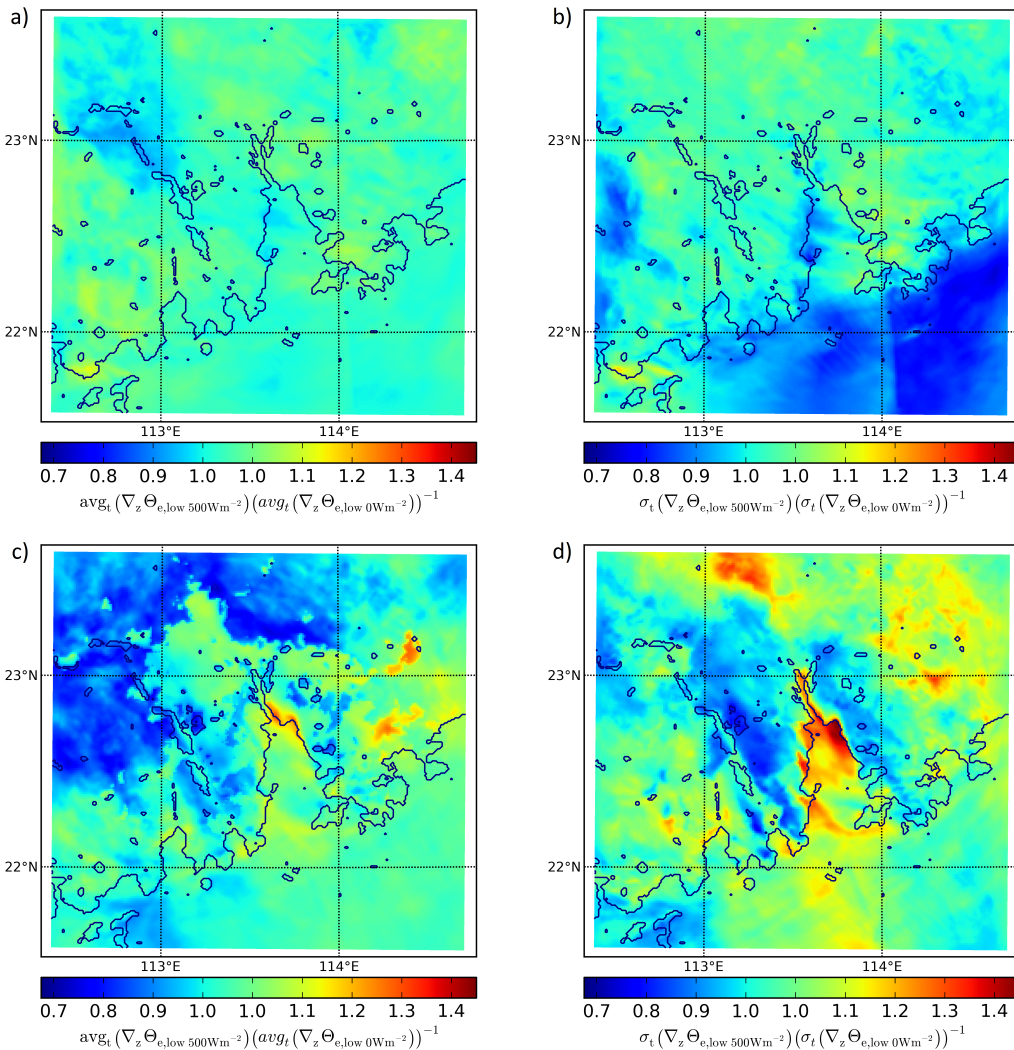


FIGURE 5.3: Average and standard deviation of the vertical equivalent potential temperature gradient. The ratios $(500 \text{ W m}^{-2} \text{ AH}) / (0 \text{ W m}^{-2} \text{ AH})$ for two different comparisons 1984-1984 (a, b) and 2004-2004 (c, d) heat forcing areas are presented here.

deviation have been computed vertically and in time, so that every point in horizontal space has values of average and standard deviation of $\nabla_z \Theta_e$ that represent the conditions of the column above throughout 96 simulated hours. Then these values are compared for different urban heat scenarios, for example "1984 500" divided by "1984 0" for both, average and standard deviation. This shows spatial variation of stability changes between different experiments.

Note that all average values are negative (see Table 5.3), hence dividing negative by negative values yields positive results for the comparison. Standard deviations are positive by definition, hence the scales in Figure 5.3.

Experiment	Domain [K m ⁻¹]	Urban [K m ⁻¹]
'84 0 W m ⁻² AH	-0.0055 ± 0.0091	-0.0043 ± 0.0073
'84 500 W m ⁻² AH	-0.0055 ± 0.0086	-0.0045 ± 0.0073
'04 0 W m ⁻² AH	-0.0052 ± 0.0085	-0.0036 ± 0.0068
'04 500 W m ⁻² AH	-0.0051 ± 0.0088	-0.0038 ± 0.0065

TABLE 5.3: Average and standard deviations of $\nabla_z \Theta_e$ for both scenarios in the domain and urban sub-domain. Units:

In the case of old urban forcing (Figure 5.3(a, b)) the impact of AH seems to be almost non-existent. Over the sea, the flow seems to be far more smooth in time, because the standard deviation is decreased. Over some areas with higher vegetation and topography gradients, the stability seems to fluctuate more. A slight decrease in average stability around 23°N and 113°E appears to be located near the Foshan area.

The effects of AH on the stability in the urban 2004 scenario are more drastic (Figure 5.3(c, d)). The average gradient is increased over the urban areas and especially over the mouth of the Pearl River and urban areas north-east of Shenzhen. The average gradient is decreased in the areas north-west of Macau and north of Guangzhou. The standard deviation however shows large increases of up to 40 % near the Pearl River outflow and slight increases north and north-east of the urban accumulations. In addition, the standard deviation shows a decrease over the densest urban areas. It appears that the stability of the local flow is stabilized by the presence of urban heat. Downstream in the absence of such heat, the fluctuations are far greater. Table 5.3 shows the related statistical values for urban areas in both scenarios. In all cases the average equivalent potential temperature gradient is slightly negative, indicating that the model flow is on average unstable in the lower troposphere during this case.

5.3 Brief summary

In this Chapter the possible effects of urban spatial expansion on the stability of the lower troposphere and the resulting effects on precipitation have been discussed with respect to the amount of human activities in the region. It was found that the

urban land cover area significantly affects the system's sensitivity to anthropogenic heat. In small urban areas a reversal of the statistical effects described in Chapter 4 have been found.

Significant large urban areas have been identified to exert a larger impact footprint on statistics in smaller local sampling areas near the centre of urban development. Hence systematic differences in measurements of operational stations could be possible in practical observations analysis, which could be related to the spatial expansion of human activities in the region. This local effect has so far rarely been studied for precipitation but mostly temperature in the context of the UHI effect [Oke, 1987].

In Chapter 6 the last question in the scope of this thesis will be addressed. How does the system respond to large scale moisture changes?

Chapter 6

Effects of background moisture changes

Chapters 4 and 5 described the effects of anthropogenic heat and extent of urbanized area on the local urban precipitation. In this chapter, the sensitivity of such precipitation to large scale changes is presented. The difference between the two concepts is the distinction between local and external forcing effects, which differ in the local system. Ultimately, the question of the thesis is whether local urban effects could explain micro climate changes in precipitation or whether larger-scale forcing effects like global climate change play a dominant role.

In principle, one could investigate temperature changes, because of the current state of knowledge in the climate research community [IPCC, 2013] suggests that temperature increases have been observed on large scales in the past half century. Due to the nature of statistics however, local effects on temperature may diverge from global trends. The assessment of the sensitivity of precipitation to temperature changes in a fully representative model atmosphere is a very difficult pursuit, and hence for this study a simplified approach is chosen in an attempt to reduce the dimensionality of the problem.

The Clausius-Clapeyron equation (see, for example, Etling [2008]) can be formulated as

$$\frac{de_s}{dT} = \frac{L_v e_s}{T^2 R_v} .$$

In the logarithmic formulation it can be utilized to estimate the relationship between temperature- and moisture changes by computing

$$\frac{de_s}{e_s} = \frac{L_v}{R_v} \frac{dT}{T^2} \approx \frac{2.5 \times 10^6 \times 1}{461 \times 300^2} = 6\% \quad (6.1)$$

with the saturation vapour pressure e_s , temperature T , latent heat of vaporization L_v and gas constant for water vapour R_v . In this particular example, a 1 K difference dT would change the saturation vapour pressure by approximately 6 %, hence potentially change the precipitation.

Assuming that the temperature changes by some amount, the moisture content of the atmosphere would change as well as shown in the example above. Hence, instead of studying the effects of large scale temperature changes, those of large scale moisture changes are investigated in this chapter. The advantage of this approach is that the water vapour itself has a weaker coupling to the velocity than the temperature (refer to the model equations in Skamarock et al. [2008]).

6.1 Initial conditions

The initial vertical moisture distribution has 75 % of the moisture located within the lowest 3 kilometre of the model atmosphere with only 9 % above 5 km (Table 6.1). There is no moisture above 11 km altitude.

Designing the proper adjustments to the moisture needs to take into account the vertical profile (Figure 6.1 and Table 6.1). It appears to be useful to compare mid level moisture advection effects with low-level convergence effects by changing the moisture in the respective layers and comparing the results.

The mass of water vapour is conserved, hence only what would be put in additionally could rain out at the surface. When interpreting Table 6.1 it becomes clear that changes of 10 % in the mass of mid-tropospheric moisture (e.g. around 500 hPa pressure or 5 km altitude) would only have relatively minor effects on the total moisture, because even if all the additional moisture converted into additional rainfall, only a 10 % increase could be expected as no additional moisture is

Level	Z [m]	$Q_v(0 : Z) / Q_v(:)$ [%]
1	109	7.2
2	174	14.2
3	251	21.0
4	340	27.4
5	438	33.7
9	1009	56.6
14	2283	76.8
20	5036	90.9
25	7775	98.0
30	10599	100.0

TABLE 6.1: The vertical distribution of moisture in the model initial condition.

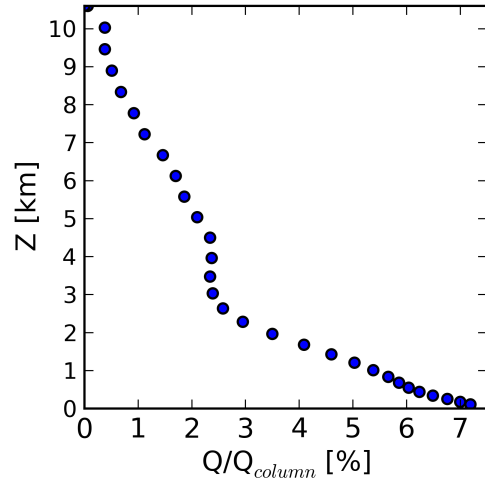


FIGURE 6.1: The vertical profile of the layer water vapour mixing ratio in the initial condition, normalized with the column moisture.

supplied from the surface (assuming that evaporation is not affected by additional precipitation). But previous chapters have focused on surface effects, so a different approach is chosen.

Moisture adjustments are applied to all vertical levels equally by $\pm 10\%$ increments. This value seems to be in line with expected magnitudes of global temperature trends according to the theoretical Clausius-Clapeyron ratio as described above.

Multiplying the mixing ratio Q_v with a constant factor a is a linear operation and the dynamic properties scale accordingly. The moisture equation in simplified form is

$$\frac{\partial(aQ_v)}{\partial t} + \vec{u} \cdot \vec{\nabla}(aQ_v) = F(aQ_v) \quad (6.2)$$

with source/sink term F . The constant factor propagates through all simple arithmetic operations linearly and hence does not affect the dynamic consistency of the model equations. This is a necessity for the numerical model to be stable, because of the conservation of mass. The first order numerical coupling between Q_v

and w is required to be small in order to maintain numerical stability; in WRF this is enforced by applying a cap-filter on w to avoid unrealistically large values. Note that in the real atmosphere, this quasi-linearity may not be true in general because of higher order non-linear inter-dependency of Q_v and Θ , hence w , $\overline{w' \Theta'}$ and $\overline{w' Q_v'}$.

To sum up, in the dry case, 10 % of moisture are subtracted from the initial and nudging conditions while in the wet case the same amount is added. The effects of these changes are studied for three different AH values: 0, 250 and 500 W m^{-2} . Consequently, the cases are labelled with their moisture values and AH parameters as shown in Table 6.2.

6.2 Precipitation statistics

As in previous chapters, the precipitation changes are characterized by comparing the simulated PDFs of different scenarios. First, the PDFs are analysed to compare the AH sensitivity for different moisture conditions. Then in the next step the moisture sensitivity of each of the different AH scenarios will be evaluated with the AH values unchanged.

These two steps address two different questions by analysing the simulation results from two different angles. Whether the moisture changes the way how AH affects the precipitation is the first and most relevant question with respect to the previous chapters. The second question is, what the influence of moisture itself is, assuming that AH remains unchanged and furthermore, whether the moisture dependence is different for different values of AH.

	90 % Q	Q	110 % Q
AH = 0 W m^{-2}	Q090–AH000	Q100–AH000	Q110–AH000
AH = 250 W m^{-2}	Q090–AH250	Q100–AH250	Q110–AH250
AH = 500 W m^{-2}	Q090–AH500	Q100–AH500	Q110–AH500

TABLE 6.2: Scenario labels in Chapter 6 for the simulations with different moisture conditions and different AH parameters.

6.2.1 Moisture dependence of the AH sensitivity

6.2.1.1 Urban sensitivity

The comparison of the PDFs of all simulated scenarios is shown in Figure 6.2, where the inset shows the sensitivity to AH by comparing each of the scenarios PDFs to the corresponding zero-AH scenario simulation.

The first finding is the similarity of the AH-sensitivity of precipitation for all but two simulated scenarios (Q110–AH250 and Q090–AH500) in the urban sub domain (see the inset of Figure 6.2a). If the urban AH-sensitivity of precipitation described in Chapter 4 shows low sensitivity to the moisture adjustments, then this means that the local AH effect is stronger than the large-scale moisture background forcing effect.

In the scenario Q110–AH250 a lower sensitivity with a similar slope is found, indicating that the intensity dependence is still comparable while the magnitude has changed. This indicates, that the increase of moisture counteracts the effect

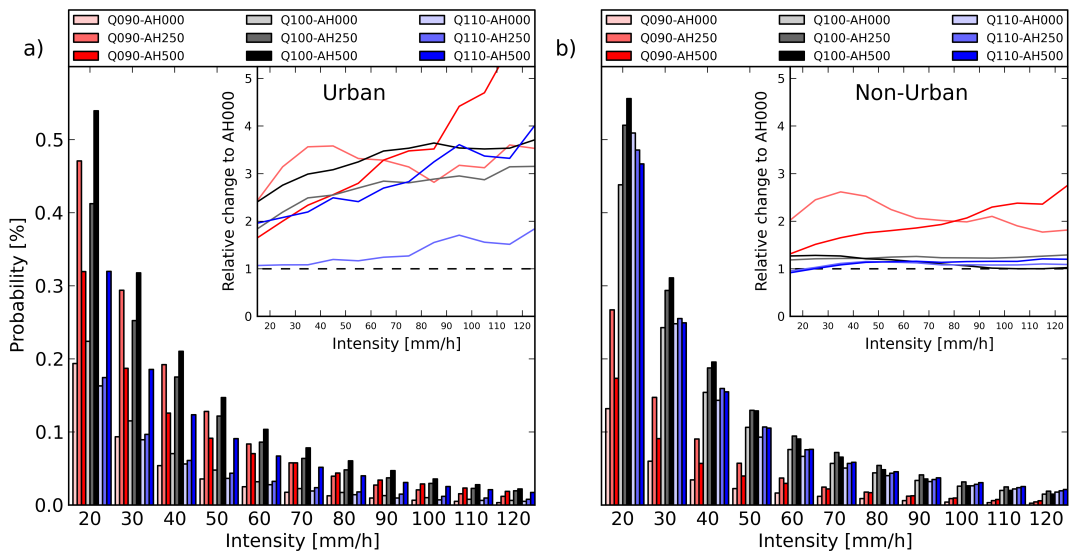


FIGURE 6.2: Simulated precipitation intensity distribution for (a) urban and (b) non-urban sub-domains. The cases Q090 in red colours refer to dry conditions while Q110 in blue refer to wet conditions. Different AH values are shown in different shades and denoted as AH000, AH250 and AH500 (refer to the legend at the top). The insets show the AH-sensitivity of each of the non-zero AH PDF divided by the corresponding zero-AH PDF, for example Q090–AH250/Q090–AH000.

of AH alone, hence the energy released by human activities is "absorbed" by the additional moisture. This could be caused by an increase in surface temperature through AH and the resulting increase in saturation vapour pressure. Further discussion will follow in the following sections.

The other interesting case is the scenario Q090–AH500, in which the slope shows an increase at about 70 mm h^{-1} . It could indicate that different physical processes of precipitation formation become important for dryer climatic conditions. In order to assess more details of this behaviour, further analysis will be discussed below.

6.2.1.2 Non-urban sensitivity

Figure 6.2b and especially the inset show that for reference and wet conditions, the AH sensitivity in non-urban grid points is very low and similar to the results of Chapter 4. For dryer conditions however, the AH sensitivity shows some similarity to that in the urban sub domain (comparing the red lines in the insets of Figure 6.2a and b), indicating that the urban effect in dryer conditions is not confined to the urban grid points alone but evident in the areas outside of the city. This is in line with past findings in dryer climates, for example in the "METROMEX" study (see, for example Ackerman et al. [1978] or Huff and Changnon, Jr. [1972]), in which downstream and upstream increases of rainfall were observed. How this effect manifests will be shown in the upcoming subsection.

6.2.1.3 Urban effects in non-urban land

The differences in precipitation fields in the simulations are shown in Figure 6.3. At first glance, it becomes visible that in the rows (e.g. for the same values of moisture) the spatial patterns look comparable. Hence most of the pattern is dominated by moisture changes. However, subtle local changes of enhancement or decrease can be seen when comparing the different columns (e.g. different AH values).

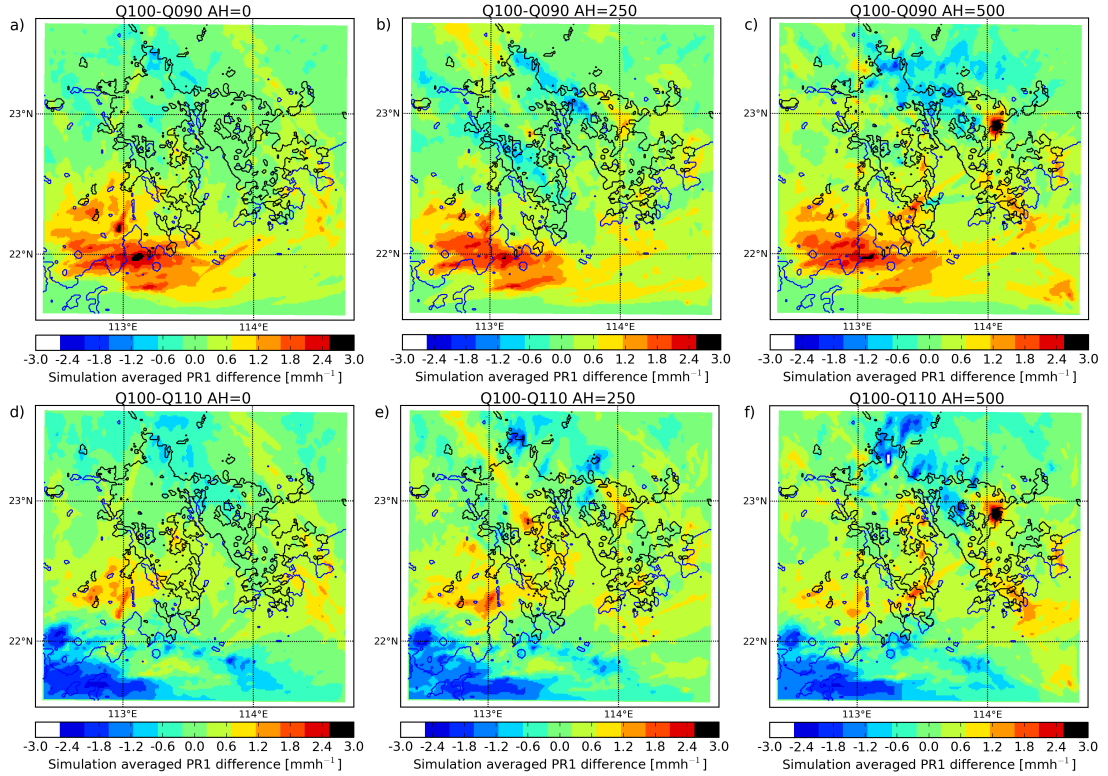


FIGURE 6.3: Comparison of (a, b, c) dry and (d, e, f) wet scenario accumulated precipitation pattern with reference simulations (e.g. Q100–Q090 and Q100–Q110) for different values of AH (0, 250 and 500 W m⁻² as 3 columns). Each panel has the title to indicate the comparison shown. The colours show dryer conditions relative to reference moisture (red and black) and wetter conditions (blue and white), while light green indicates no changes. The contour lines show the outlines of urban (black) and water (blue) model land use categories.

For the analysis of these patterns it is important to remember that the low pressure trough simulated in this case was south of the domain in the beginning of the simulation (refer to Chapter 3.1) and moved northwards, crossing the domain and dissipating close to the end of the simulation. So the wind field switched from mostly northerlies in the beginning to easterlies and southerlies towards the end of the simulation.

Figures 6.3a-c show a large dry belt in the southwest of the urban area in all dry scenario simulations. This feature is not affected by AH. However, with increasing AH an increased wet band in the north of the domain is found (refer to Figure 6.3b and 6.3c). When comparing panels (a) and (c) (as well as (d) and (f)) it also appears as if the wet areas for higher AH values are more localized and show larger peak values in the north of the urban area. Additionally, there is a dry

spot at 23°N , 114°E that appears to intensify with increasing AH for wet and dry scenarios (compare panels b to c and e to f).

In the wet scenarios, the dry belts obtained in the dry scenarios in the south were not found. Instead, increased rainfall is found in the south-west corner of the domain. In addition, the wet areas in the north of the domain are increasingly wet in the wet scenarios and cover larger area. Interestingly there are still dry areas between the wet patch in the southwest and the urban edge in the centre of the domain (see for example panel (d)). Analyses of individual snap shots of simulated precipitation (not shown) indicates that most of the precipitation in that area falls during the early simulation, e.g. when the area is downstream of the city. This agrees with findings of Huff and Changnon, jr. [1973], where increased rain was found about $25 - 50$ km downstream of the urban area. In these simulations, the distance is approximately 50 km.

An additional feature in the case Q110–AH250 explains the low sensitivity of urban precipitation compared to the other simulations: a dry band extends from the east of Zhongshan through Guangzhou (refer to cities shown in Figure 3.4) into the northwestern part of the domain, covering most of the urban area. Isolated local wet patches can be found north of Guangzhou and Donguan, but only small parts of urban area are covered. The small size of those patches suggests that those are related to convective systems, explaining why the sensitivity still shows slight increase for increasing precipitation rates over the urban area.

The other wet area in the north centre of the domain appears to be mainly affected by simulation conditions where southerly and southeasterly winds prevail. In this case however, the wet area extends from within the city over its boundaries into the northern part of the domain. This is related to the difference between moist advection over the sea in the case of southerlies and dry advection over land in the case of northerlies.

The last conclusion to be drawn from Figure 6.3 is that in the dry simulations, the AH sensitivity seems to manifest north of the city, e.g. 23.2°N and 113.5°E . Snapshots show that this happens predominantly after the northerly flow collapsed in the second half of the simulation and the wind turns southerly. Because of this

background flow change, the low-level moisture from the mouth of the Pearl River is transported over the urban area and interacts with the increased heat at the surface, giving the increased sensitivity for dry scenarios in the inset of Figure 6.2b.

In order to further separate the effects of urban activities and moisture changes and unveil their interdependency, the next subsection is dedicated to the sensitivity of the system to the background moisture, assuming that AH remains unchanged in the comparison.

6.2.2 Moisture sensitivity

To understand how sensitive the precipitation rates are to moisture changes, the comparison of dry and wet scenarios with the reference moisture scenario is plotted and shown in Figure 6.4 for different parameter values of AH.

The likelihoods of urban precipitation (Figure 6.4a) in both wet and dry cases are lower than for the reference simulations except for the Q090-AH250 case in which precipitation rates below 60 mm h^{-1} are slightly enhanced compared to the reference case. This increase happens in the area around 22.5°N and 113.5°E , where a wet belt extends to the north-west (refer to Figure 6.3b) and in the other parallel wet belt north-east of Guangzhou. Both wet areas in that simulation are almost parallel to the urban outlines as indicated by the black lines. This is caused by urban edge convergence lines during the time when the trough is located over that area and the background wind weakens significantly.

The decreased precipitation in case Q110–AH250 has been explained in the previous subsection.

The non-urban sensitivity behaves differently as shown in Figure 6.4b and explained in the previous subsection. The dry scenario precipitation is significantly reduced compared to the reference case due to the large dry patches that extend throughout almost half of the domain (see Figure 6.3a-c). The reasons for the decrease are enhanced surface temperatures and decreased relative humidity in the dry case and the saturation limit in the wet case (refer to the next section).

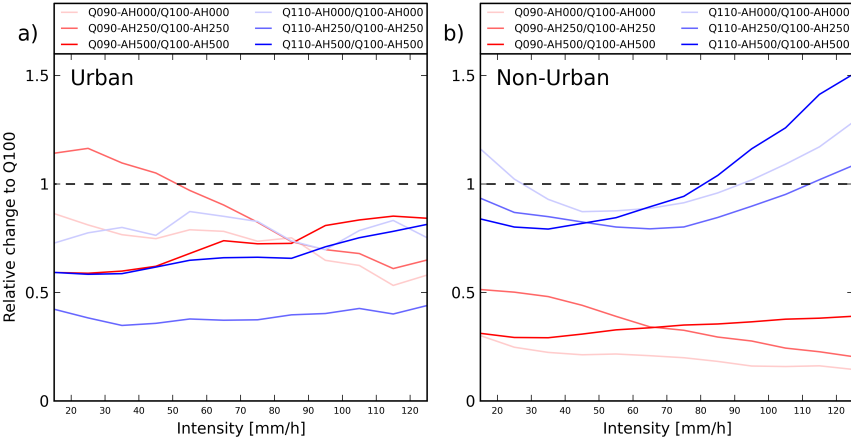


FIGURE 6.4: Urban (a) and non-urban (b) moisture sensitivity of precipitation for different AH values. Dry scenarios are plotted in red and wet scenarios in blue. In each line, the dry/wet case is compared corresponding to the reference case, please refer to the legend. The dashed line shows the ratio of 1, indicating no change.

In the wet case a decrease of precipitation rates below 80 mm h^{-1} goes in hand with a large increase of heavier precipitation above 80 mm h^{-1} in the wet area downstream of the city in the early simulation as described above. This increase indicates that additional moisture supply upstream of the urban area can enhance the downstream precipitation.

The presence of the city appears to diminishes the local urban effects of background moisture changes, while background moisture changes are found to enhance the downwind AH effects on precipitation (compare the difference between the two red lines in Figure 6.4b and 6.2b).

The effects the vertical structure of the troposphere in different scenarios is discussed in the next section.

6.3 Vertical structure of the atmosphere

The vertical structures of temperature and moisture provide useful insight in the changes that the moisture adjustments cause in the simulations. First it is important to choose an appropriate temperature variable which relates to buoyancy. Typically, in PBL studies the virtual potential temperature is used because it is interpreted as the potential temperature that a dry air parcel would have, if it

had the same density as the wet air parcel. This reduces the dimensionality of the dynamical system, allowing to use dry adiabatic analysis methods to investigate the behaviour of air parcels. Most importantly, virtual potential temperature is inversely proportional to the density of the air parcel and the dry gas constant is applicable. For practical purposes, the virtual potential temperature changes translate directly to specific volume (inverse density) changes. As long as diabatic heating is not considered, this measure is sufficient to identify local instability. Averages of moisture and temperature in time throughout the 96 simulated hours for every grid point in three spatial dimensions are evaluated. To split urban and non-urban signatures, horizontal grid points are averaged for urban and non-urban sub domains. This yields two vertical profiles for urban and non-urban parts of the domain. The formula to compute this data for the example of the urban virtual potential temperature is

$$\overline{\Theta_v(iz)}_{urban} = \frac{\sum_{nx} \sum_{ny} \overline{\Theta}_{v,t}(ix, iy) \delta_{urban}}{N_{urban}} = \frac{\sum_{nx} \sum_{ny} \frac{\sum_{nt} \Theta_v(it, ix, iy)}{N_t} \delta_{urban}}{N_{urban}}$$

for spatial indices ix, iy and iz, temporal index it and total number of grid points nx, ny, nt, N_{urban} and N_t , where the bars and subscripts indicate averages and δ_{urban} selects only urban grid points. The same formula is then applied to the non-urban grid points and for the cloud- and water vapour mixing ratios and equivalent potential temperature.

6.3.1 Temperature changes

Because of the nature of surface heat fluxes, Θ_v shows dependence on AH in the lowest 1000 m of the urban sub-domain (see Figure 6.5a), but the wetter scenarios show lower temperatures. This is related to the increased heat capacity of the moist air and the decreased potential evaporation of dryer soil. There is also a small area in the boundary layer where a negative virtual potential temperature

gradient is found in the urban area, hinting at an unstable layer close to the surface.

In the upper troposphere above 5000 m, the dominant differences are caused by the moisture adjustments (Figure 6.5c, d). The sensitivity to AH is found to diminish around 1500 m and shows insignificant effects for the dry and reference scenarios above 6000 m.

The profiles in the non-urban sub-domain (Figure 6.5b, d) appear to be less smooth. Below 1500 m the spread of the different scenarios is smaller than in the urban sub-domain, and has no negative gradients near the surface. The effect of moisture is the dominant difference because no significant difference between different values of AH can be identified from the profiles.

The finding that human activities do not exert a large influence on the upper tropospheric temperature is reasonable, because the amount of energy dispensed into the atmosphere is still low compared to that of the maximum solar heat flux at the surface (at noon on a clear day $\mathcal{O}(1 \text{ kW m}^{-2})$), which acts on every part of the surface, not only urban land. So the heating effect of AH appears mainly in the lower troposphere and only in urban areas. Moisture changes, however, have a larger but less localized effect. Increased moisture causes lower tropospheric cooling and upper tropospheric warming. This is related to the changes of heat capacity of the air and the soil, as dry simulations show higher temperatures up to 4000 m and the reverse is the case above, because of latent heat release during condensation when dry air is lifted. The reason for this conclusion lies in the behaviour of the water vapour, that is shown in the next subsection.

6.3.2 Water vapour changes

Figure 6.6 shows the average moisture profiles of the troposphere. It appears that the differences are small among different simulations, but when comparing individual levels (for example at $Z = 1000 \text{ m}$), the differences are at the order of 10 % or less, indicating that the signal in these profiles is weaker than in the temperature profiles, because the initial moisture adjustment was of the same magnitude.

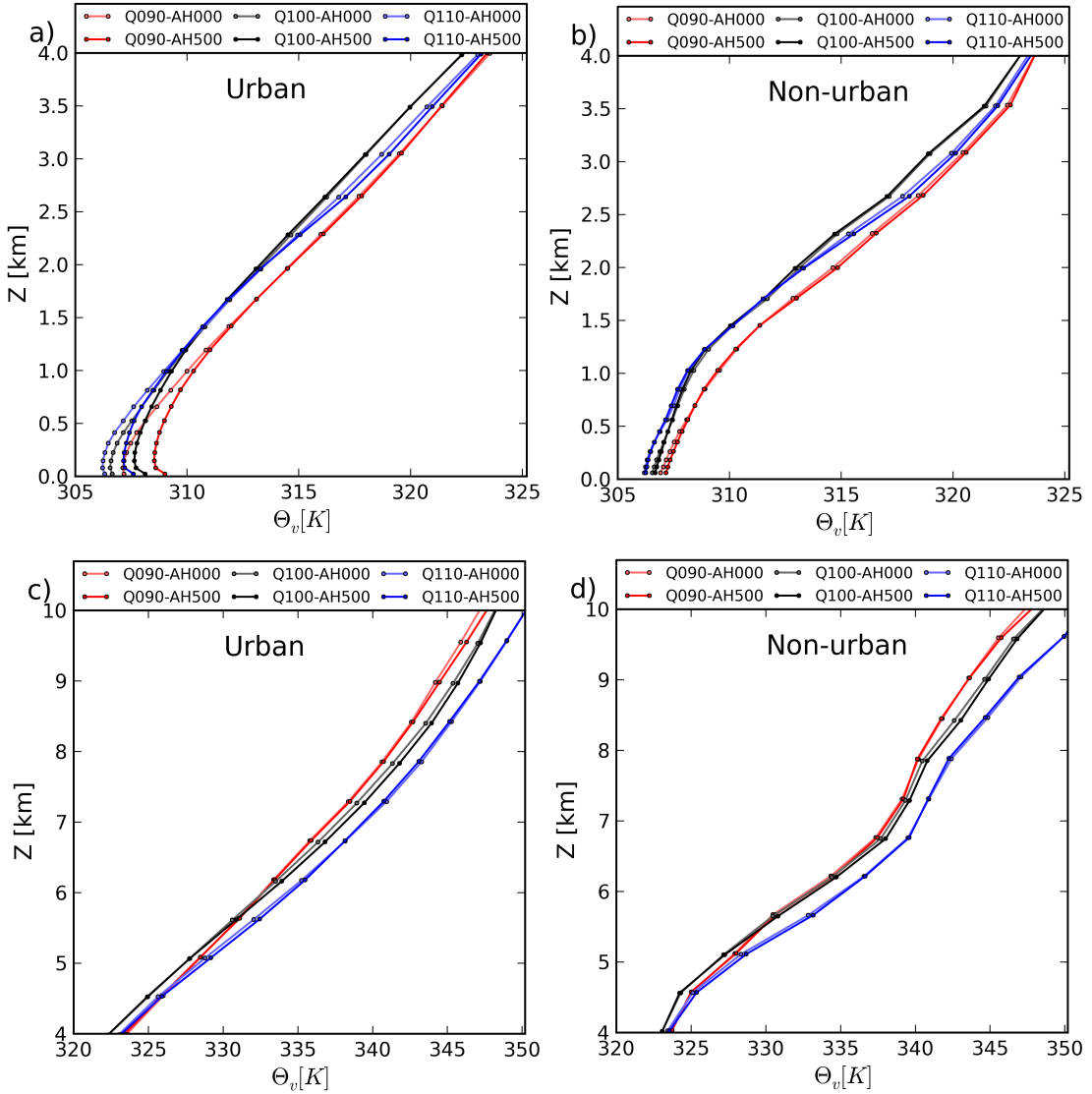
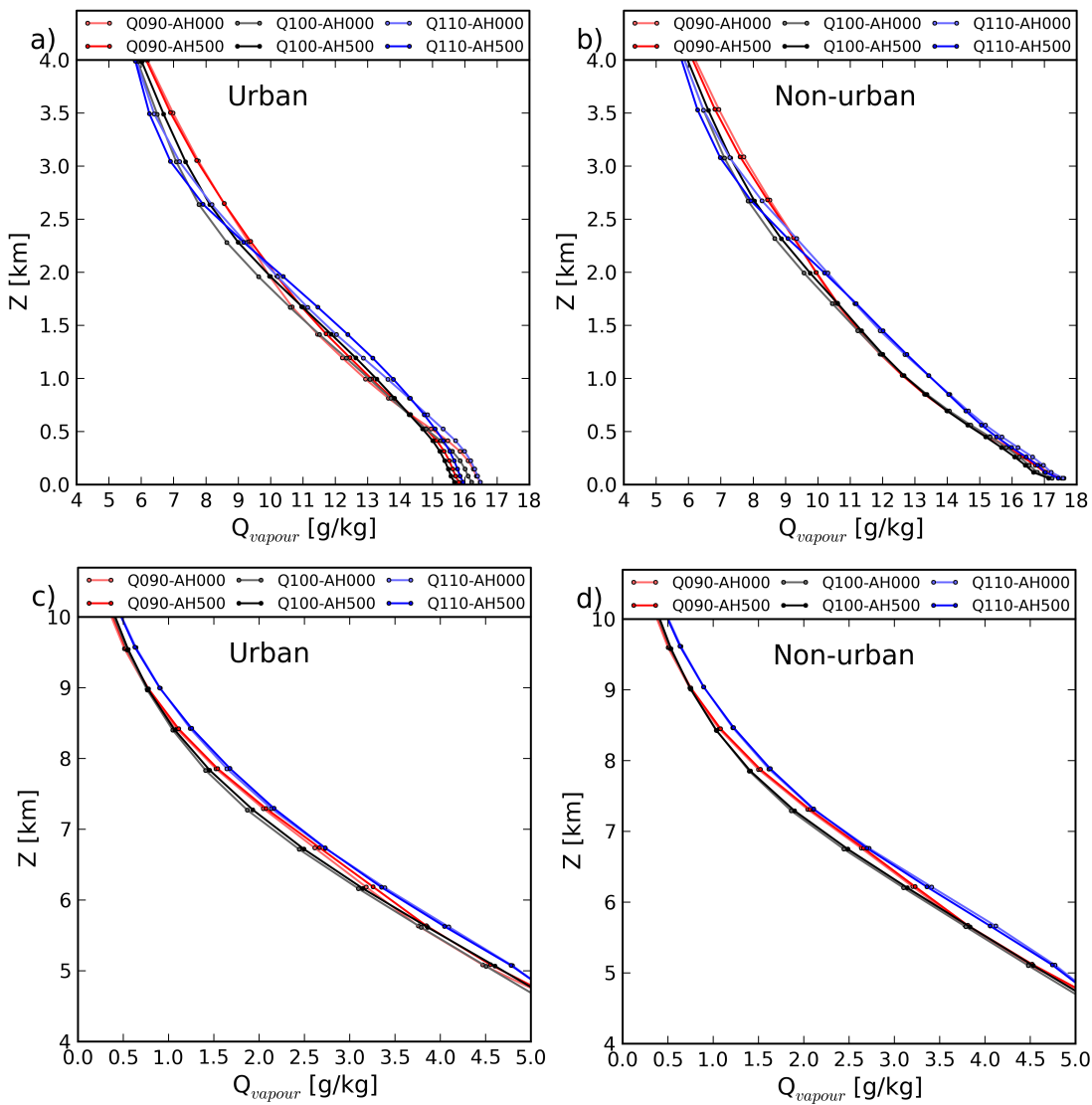


FIGURE 6.5: Vertical profiles of average Θ_v in the urban (a, c) and non-urban (b, d) sub-domains. The different colours refer to different scenarios for AH = 0 and 500 W m^{-2} and Q = 90, 100 and 110 % as shown in the legends at the top of each panel. The profiles are presented for (a, b) 0 – 4 km and (c, d) 4 – 10 km altitude.

When comparing panels (a) and (b), slightly increased moisture in the wet scenarios (Q110) is found in the layer between 1000 and 2000 m as well as above 4500 m (compare Figures 6.6c, d). The layer between 2000 and 4500 m shows an opposite relationship between moisture adjustments and simulated moisture. This is the same layer above which the virtual temperature switches from relative warming to relative cooling as described at the end of the previous subsection. This shows that at that particular layer the different amounts of latent heat between different


 FIGURE 6.6: Same as Figure 6.5 but for Q_{vapour} .

moisture values become important, so that in layers above more heat is released the more moisture is added to the model. A second layer in which the dry scenario shows slightly enhanced water vapour is between 6000 and 8000 m altitude. This moisture is brought up from the surface through enhanced convection because of enhanced surface temperatures as shown in Figure 6.5a and b.

The effect of AH on the moisture profiles is small. When comparing Q_{vapour} in the lowest 500 m of the urban atmosphere, a small drying effect can be seen in Figure 6.6a. The magnitude is approximately 10 %, so comparable to the scenario moisture adjustment. However, when comparing the spread of the different lines near the surface, the difference between different moisture scenarios are smaller

the difference between different AH values, so the effect of AH on surface moisture is larger than the effect of the moisture adjustments.

The fact that the average moisture profiles show a small sensitivity to AH and large scale moisture adjustments suggests that the moisture in the model has a relatively small retention time. In order to further demonstrate the described mechanisms, the average stability and cloud occurrence will be presented in the following subsection.

6.3.3 Stability and cloud changes

The graphs in Figure 6.7a and b show that the layer between the surface and 3000 m is unstable because of the negative equivalent potential temperature gradients. In the dry simulations, a near-neutral layer between 1500 and 4500 m is found and extends relatively higher up than in the wet and reference simulations. Especially at the surface, the dry scenario simulations show larger gradients and hence more instability, yet the slope changes abruptly at about 1500 m, so practically above the PBL. This indicates that clouds are to be expected higher up in the troposphere, approximately where the inversion is found. In Figure 6.7c and d, this can be seen, because the maxima of cloud water mixing ratios are located around 4000 m.

In the wet scenario however, the near-surface Θ_e profile is less steep, but shows a clearer inversion and a more stable layer above at around 3500 m. This corresponds with the local maximum in cloud water mixing ratios (compare Figure 6.7c, d).

In the non-urban environment, the cloud water mixing ratios seem to depend mostly in the background moisture adjustments, because differences between different AH values are small compared to those of different moisture scenarios.

In the urban environments (Figure 6.7c) the behaviour is more complicated. For different values of AH, a large difference in cloud incidence can be found throughout all scenarios.

In Figure 6.8 this difference is plotted against altitude. Each of the lines shows

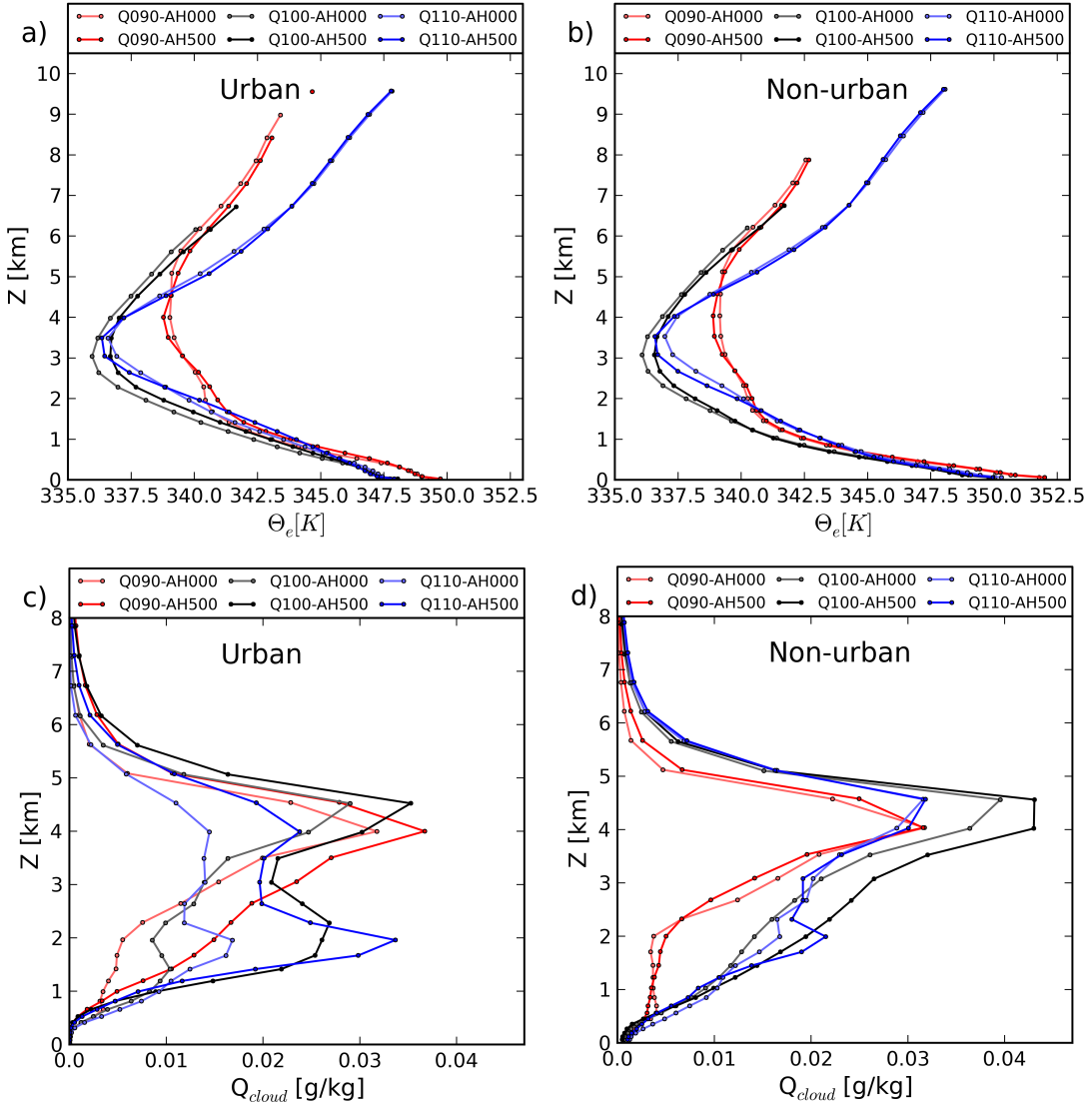


FIGURE 6.7: Vertical profiles of average (a, b) Θ_e and (c, d) Q_{cloud} . Similar to previous profiles in Figures 6.6 and 6.5.

the difference between the AH500 scenario and the corresponding AH000 scenario over the urban area (denoted by Δ_{AH}). Except for the lowest kilometre of the atmosphere, an increase in cloud water is found for all moisture scenarios, that has a similar shape like an inverse gamma distribution, but shows a secondary local maximum at around 4000 m altitude. The decrease of very low clouds below 2000 m agrees with the surface temperature increase described in previous subsections.

Between 3500 and 5000 m, a slight enhancement of the difference can be seen in the wet scenario. In addition, a diminishing is seen in the dry scenario between

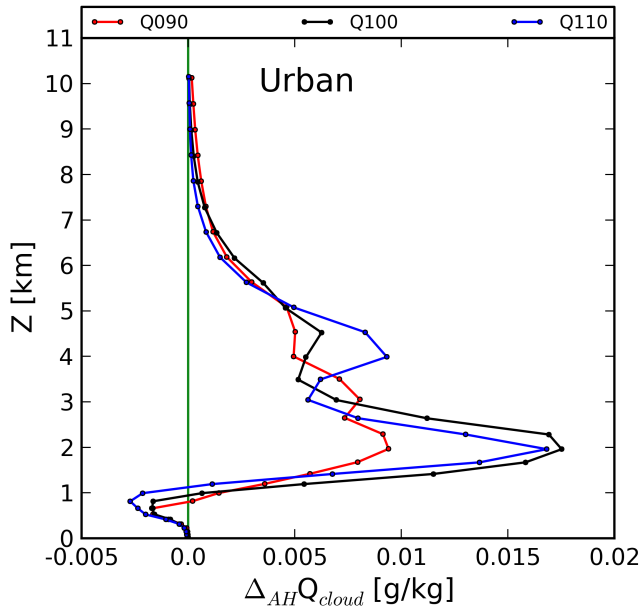


FIGURE 6.8: Vertical profiles of average difference $Q_{cloud}(AH = 500 \text{ W m}^{-2}) - Q_{cloud}(AH = 0)$. The green line indicates no difference.

1500 and 2500 m. The overall shape of the difference curve is similar in all scenarios, indicating that AH dominates cloud formation in the urban sub-domain.

6.4 Brief summary

In this chapter the impact of the moisture background on precipitation statistics is studied and discussed. Increasing AH is found to increase low level temperatures in the urban sub-domain and cloud water concentrations in the mid troposphere. Higher moisture is found to decrease temperatures below 4000 m altitude and increase upper tropospheric temperatures. The low-level water vapour mixing ratio over the non-urban sub-domain is higher than that over the urban sub-domain and the opposite is true for temperatures. The spread of the profiles among different scenarios is much higher over the urban sub-domain. The stability of the dry scenarios shows a neutral layer as opposed to an unstable layer followed by an inversion of Θ_e , causing more complicated precipitation behaviour.

The urban AH sensitivity described in Chapter 4 shows a relatively small sensitivity to moisture adjustments. In the dry scenario however, the AH effect is barely changed between urban and non-urban areas because under dry conditions, advection effects become more important. The moisture adjustments in the wet scenario produce less precipitation in the urban sub-domain, but more heavy precipitation above 90 mm h^{-1} in the non-urban sub-domain. In the dry scenario however, the change relative to the reference moisture shows slight decreases with intensity. In all scenarios, the differences in precipitation accumulations are most obvious in the downstream simulations, where northerlies produce dryer areas in the south of the cities and southerlies wetter areas in the north. The enhancement in the wet scenario is slightly smaller than the diminishing in the dry scenario, because the open water bodies supply sufficient moisture to the system, whereas in the dry scenario with a relatively dry flow coming from the land, the effect is larger. The effect of AH on cloud formation over the urban area shows a relatively low sensitivity to moisture changes.

Chapter 7

Concluding remarks and future investigations

7.1 Concluding remarks

In this thesis, questions regarding the local urban sensitivity of precipitation to different internal and external forcing effects are addressed.

The intensity of human activities was simulated by the anthropogenic heat parameter in WRF model simulations. Simulated local urban precipitation in the urban parts of the Pearl River Delta domain was found to be sensitive to the amount of anthropogenic heat released at the surface (see Chapter 4). The sensitivity applies for values of AH larger than 100 W m^{-2} and appears to increase with precipitation intensity for large AH values equal or above 250 W m^{-2} . The temporal standard deviation of the Richardson flux number and turbulent kinetic energy were found to increase over the urban area when comparing the reference $\text{AH} = 0$ scenario and the 500 W m^{-2} scenario. Comparison of 5-minute integrated "instantaneous" snapshots of hourly precipitation rates show relocation of rain patterns and spawning of additional heavy rainfall cells over parts of the domain. Also amplification of individual rain patches was found in the output.

Urban spatial extent plays a role for the AH-sensitivity as described in Chapter 5.

When comparing simulations with the same amount of AH for two different stages of urban development in the mid 1980's and early 2000's, a significant difference to the results in Chapter 4 is found. The results indicate local decreases rather than increases can be expected for large human activity in small urban areas. This is consistent with past findings from observations in the 'METROMEX' study, where downstream changes of precipitation were documented [Ackerman et al., 1978]. The difference was explained by comparing changes in stability and the total amount of energy released for the different urban extents. Small urban areas may not produce significant effects on local micro-climates as well as the regional statistics. However, a large urban extent was found not only to affect its own regional climate, but the change is more significant when sampling in the urban centre (e.g. where 1980's urban areas were located). A station, for example, that did not take into account regional changes could potentially experience systematic differences in observed rainfall statistics because of those regional effects.

In the final part of the study, the effects of large scale moisture changes are investigated. Reductions of 10% in model moisture amplify certain effects of AH on regional scales through enhanced advection. Increases in moisture play an increased role over the non-urban area, where the spread between precipitation rate PDFs of "dry" and "wet" simulations relative to the reference moisture scenario increased with increasing intensity, indicating that especially heavier precipitation in the periphery of large urban clusters could be affected by changes in tropospheric moisture. Increased moisture produces more clouds in the lower troposphere around 2000 m altitude.

Overall, this study has produced theoretical evidence that human activities potentially affect precipitation statistics on local and regional scales. A comparison of the different effects in this region shows that the amount of human activities in terms of energy release into the atmosphere has a large potential to affect the rainfall statistics, given the large extent of the cities in this region. In addition, long term tropospheric moisture changes appear to affect mainly advection effects downstream of urban areas and cloud distribution effects in the lower troposphere when added to the AH effects.

The next steps will require further comparisons and verifications of the results for different cases and conditions as well as comparisons of how different physical assumptions about other factors like aerosols, cloud physics, boundary layer interactions, etc. interact with the results presented here. This study may serve as a first step to motivate further in-depth investigations of urban precipitation behaviour in local and non-local forcing contexts.

7.2 Suggested future studies

In addition to the civil engineering approach, to increase model complexity and take more effects into account for simulations, the useful route to take after this study is to investigate the moist buoyancy effects further. Questions that are left to answer with rigorous detail are how, in this model setting, the horizontal and vertical scaling of clouds and precipitation behave and whether signatures of urban patterns can be found in the patterns produced.

The relationship between latent and sensible heat in the context of local air conditioning is also interesting. Water vapour affects the density and heat capacity of air, potentially affecting the generation or inhibition of buoyancy. These microphysical effects interact with urban aerosols (e.g. black carbon particles) and urban heat storage.

The impact of surface heterogeneity has been studied for simple geometries with large eddy simulation models (for example Gryschka et al. [2008]) but these simulations are still incompressible, so for large surface energy gradients and local secondary circulations like UHI circulations or sea breeze flows these models can not fully describe the phenomena. Studying how these secondary circulations interact with the urban induced flow on a fundamental level seems to be a reasonable next step. Especially after Gryschka et al. [2014] showed in a follow-up study that the downstream turbulence in surface heterogeneity-forced flows does not add up linearly. This has interesting applications for downstream precipitation formation and should be studied carefully.

Li et al. [2016] described interactions between urban-induced buoyancy and sea

breeze-induced moisture advection. Singapore however does not have large topography. Sea breeze circulations are probably more likely to form without obstructions, so studying this effect in the significantly hillier Hong Kong appears to be an interesting alley to explore.

As another important step, it would be fruitful to idealize the simulations and modify the model, such that different secondary circulation effects (sea breeze, urban secondary circulation, background flows) can be simulated separately and more carefully described.

Furthermore, the possibility to study scaling behaviour of convection over cities by applying modern wavelet analysis tools and tracing methods would be usefully related to ventilation questions of urban air quality. If connecting the AH questions with thermal stress estimations, the studies would have potential impact on the architectural science community.

Appendix A

Compilation and performance

A.1 Compilation

The Weather Research and Forecast model (WRF) version 3.5.1 was compiled with Intel Fortran compiler version xe2013.2.146 and Intel C compiler version xe2013.2.146 on the local computer cluster. In order to succeed with this task, NetCDF version 4.3.1, NetCDF Fortran version 4.2 needed to be compiled beforehand. The NetCDF version 4 features modern compression libraries which reduce the size of output files by up to 70 % in some simulations. The efficiency of the compression is greatest for values close to zero.

A.1.1 Dependency Compilation

The dependency of the NetCDF libraries required bzip2 version 1.0.6, curl version 7.35.0, hdf5 version 1.8.12, jasper version 1.900.1, jpeg version 6b, libpng version 1.6.9, pkg-config version 0.28, szip version 2.1 and zlib version 1.2.8 to be compiled, verified and tested with the same compiler settings. This process took some time due to a range of difficulties that can arise from environment settings. A total volume of 1.1 Gigabyte of executable code was generated in the process of compiling libraries, before the actual model code could be compiled. The whole

package is customized and depends on a long list of environment settings, but will not be discussed here.

Ultimately, a highly optimized executable was obtained, that allowed for compression with the quickest available algorithms, thus reduced the IO time used by the model. It should be noted, that parallel IO for NetCDF was not enabled, thus will not be used for the model compilation as well. The reason is basically that for non-constant IO streams, the performance improvement by such setting will be relatively small. Since WRF creates instantaneous output at certain user defined times, the model IO can be considered as a non-constant IO stream problem. Therefore, it is not worth the effort to carry out the incomparably more difficult compilation of a parallel NetCDF code. Despite that, the difference between writing from individual nodes or writing at once is small, because all nodes run time-stepping at the same rate, e.g. arrive at the output time step at the same real time.

A.1.2 Model Code Compilation

The WRF Preprocessing System (WPS) was compiled in a serial mode, thus each job will only be carried out by a single core, but due to the low amount of arithmetic calculation and the high amount of IO time, this has no significant effect on performance.

The WRF model was compiled in a parallel mode, using the message parsing interface openmpi version 1.6.4, which was compiled with the same Intel compilers and set up by the system administrator. The highest optimization was used, while maintaining a value-safe compilation standard. It should be noted that the dynamic core was compiled with slightly lower optimization for stability reasons at first, but towards the end of my study period I managed to compile an experimental version with highest optimization settings. However, I did not have sufficient time to test that setting extensively.

A.2 Performance

The system administrator confirmed, that a performance improvement of about 90% was achieved relative to the reference set-up, which is using pre-compiled executables for all dependency libraries and Portland Group compilers (PGI) that were previously available on the system.

Most recently a higher degree of optimization was achieved, so more performance may be achievable. With the new Portland Group compilers however comes also the support for the NVIDIA CUDA technology, which could allow for WRF compilations on GPU clusters for significantly higher degrees of parallelism.

It was found in the experiments for this thesis, that in this domain setting the scaling of the model performance with increasing numbers of cores is not very good. A spot where resources are used optimally seems to appear when using 32 cores on 2 nodes with a minimum of total computation time. Using 16 cores on a single node or 48 cores on 3 nodes consumes about 5 % more core time and using 64 cores on 4 nodes uses about 15 % more core time. Hence the effort of compiling the model on a CUDA system may not be worthwhile for simulations of similar scale as in this thesis. For simulations with significantly larger domains the situation is probably different and larger numbers of cores may improve the performance.

A.2.1 Experiment for Large Scale Domain (D01)

A simple performance experiment was carried out on the outermost domain. The setup was chosen to be appropriate for a 25 km length scale simulation, using single moment 4 class micro-physics, standard radiative transfer, convection and boundary layer parametrization schemes as well as a standard similarity theory based surface layer scheme. A simulation of one summer month took an amount of about 20 hours of real time with 32 cores, thus bears a ratio of

$$\frac{20 \text{ hours} \times 32 \text{ cores}}{24 \text{ hours/day} \times 30 \text{ days/month} \times 1 \text{ month}} = \frac{1}{1.125} \text{ core hour/simulated hours}$$

or 1 hour/36 simulated hours with 32 cores. Thus one year simulation could be executed in approximately 11 days.

The ratio may be further increased by optimizing time steps (here chosen to be 120 seconds and 30 seconds for acoustic modes) and vertical levels in the model, however at this point we did not investigate further for large scale domains.

A.2.2 Experiments for Small Scale Domains (D02, D03)

After testing the large scale domain performance, a test was carried out for the local scale domains. It turns out that the computation of higher resolution physics in a two-way-nested setting requires significant amounts of computation efforts. The easiest way to think about it is to consider the time stepping. WRF utilizes a 3rd order Runge-Kutta time stepping scheme, which means that for each time step, a number of sub steps are evaluated, in this case 3 sub steps. For the sake of simplicity, one may only look at physics calculations plus dynamics calls, since those are numerically more expensive than averaging or simple arithmetic operations. Each time step contains 3 dynamics calls plus one physics call. Each dynamics call contains 4 more dynamics calls for fast modes (acoustic modes), thus can be thought of as total 16 calls per time step (3 slow modes plus 4 times 3 fast modes). It is worth mentioning that acoustic steps can be customized, e.g. reduced or increased to trade stability for performance or vice versa. Also, the physics can be set to be called only at certain time steps (say for example: every 10 minutes for radiative transfer, every 2 time steps for turbulence, etc.). However, since this detail is highly custom for different simulations and grid spacings, it may be ignored here and assumed that every physics will be called once for each time step.

Consequently, a time step of 120 s for the outermost domain D01 will contain 16 dynamics calls and one physics call. The second domain D02 will use a shorter time step, in this case 20 s, thus a factor 6 more operations than the outermost domain. The innermost domain D03 is using a time step of 4 s, thus multiplies the amount of operations by a factor 5 relative to D02. Table A.1 shows an estimation

Domain	Grid x	Grid y	Grid z	Call phys	Call dyn	Call total	Ratio
D01	310	200	51	1.6M	25.3M	26.9M	
D02	151	90	51	2.1M	33.3M	35.4M	1.32
D03	241	231	51	42.6M	681.4M	724.0M	26.94

TABLE A.1: Estimated computational calls of dynamics and physics with relative comparison for different domains. The unit M in this case refers to 10^6 .

of the amount of computation for different domains based on above mentioned assumptions.

It is obvious, that the innermost domain adds a significant amount of computation to the whole simulation. Therefore, it is not surprising to find out, that ratios of approximately 8.333 core hours/simulated hour or 1 hour/3.840 simulated hours with 32 cores were observed in these experiments.

Thus a simulation of 4 days would take about 1 day to complete. As mentioned previously, this ratio may be improved by changing time steps and acoustic time steps, as well as the intervals of calling physics.

After spending significant amounts of time on improving details of the simulations, a full case simulation of 96 h could be finished within 22 h of real time with 32 cores on 2 nodes. Further improvements may be possible but are most likely not worth the while because only small gains can be expected.

Appendix B

Model land use

B.1 Overview over the land use

In the simulations for this study, two sets of land use data that are part of the WRF package have been used. The data are derived from the USGS as well as data from MODIS satellite retrieval. In order to start with the more recent data set, the MODIS-based data (dated approximately 2004) was initially used as a reference. Later in the study, only the urban grid point locations were extracted from the USGS-derived data (dated approximately 1984).

In order to maintain a full dataset, which the preprocessor can analyse, it is required to adjust the variable $LANDUSEF$ accordingly. This land use fraction variable has N dimensions for each horizontal grid point if N different land use types are defined. The fractional character of the variable allows to modify individual categories while the sum

$$1 = \sum_{k=0}^{N-1} LANDUSEF(k, ix, iy) \quad (\text{B.1})$$

remains constant for all horizontal grid indices ix and iy . This simple condition allows to study the differences between grassland, urbanized land, forests or tundra for example.

In this study, land that would have been urban in 2004 but not in 1984 is assigned

to be broad leaf forest. This appears reasonable, when considering the indigenous species and the abundance of water and energy for plant growth in this region. In Figure B.1 the differences between the two data sets that were finally used are visualized. The white lines indicate nest positions and the colours are explained in Table B.1.

No.	Category	RGB (256)	Colour
01	Evergreen needle leaf forest	(0,102, 0)	Green A
02	Evergreen broad leaf forest	(0,153, 0)	Green B
03	Deciduous needle leaf forest	(51,153, 0)	Green C
04	Deciduous broad leaf forest	(102,153, 0)	Green D
05	Mixed forests	(0, 51, 0)	Dark green
06	Closed scrub lands	(102,153,102)	Pale green
07	Open scrub lands	(153,204,153)	Pale green
08	Woody savannas	(153,153,102)	Beige
09	Savannas	(204,204,153)	Beige
10	Grassland	(0,255, 0)	Bright green
11	Permanent wetlands	(102,102, 0)	Green-brown
12	Crop lands	(204,204, 0)	Dark orange
13	Urban and Built-up	(204, 0, 0)	Red
14	Crop land and natural vegetation mosaic	(153,255,204)	Mint turquoise
15	Snow and ice	(204,255,255)	Pale cyan
16	Barren or sparsely vegetated	(255,255,204)	Pale cream
17	Water	(102,153,255)	Dark blue
18	Wooded tundra	(255,153,255)	Pale pink
19	Mixed tundra	(204,102,204)	Pink

TABLE B.1: Colour codes in Figure B.1. The author attempted to choose the colours in a reasonably intuitive way.

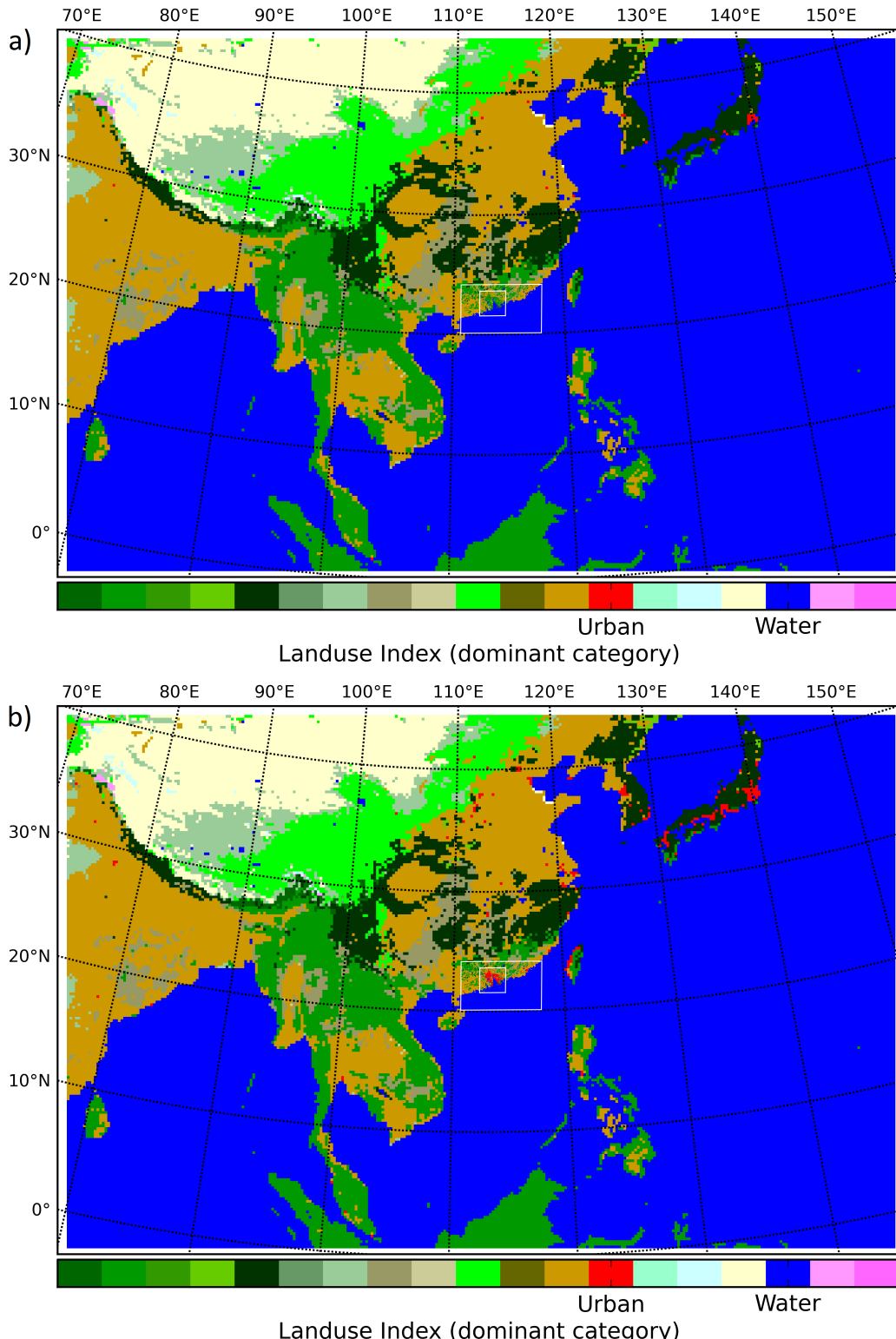


FIGURE B.1: Model domain land use dominant categories plotted for all domains in (a) 1984 and (b) 2004. The colours are explained in Table B.1 and the white lines indicate nest locations.

Appendix C

Calculation of the equivalent potential temperature

The calculation of the equivalent potential temperature in a reasonably accurate way requires the estimation of the potential temperature and absolute temperature at the lifting condensation level, e.g. the level at which condensation occurs under positive vertical motion of an air parcel. From a thermodynamic point of view, the actual level is not interesting and does not need to be computed.

C.1 Calculation of dewpoint temperature and saturation vapour pressure

When following Bolton [1980]'s suggested formula, it is necessary to compute the dewpoint temperature first. This is the temperature at which condensation occurs in an air parcel if it is cooled. This can be calculated by inverting the empirical Arden Buck formula [Buck, 1981] for saturation vapour pressure e_s at temperature T

$$e_s = a \exp \left(\left[b - \frac{T}{d} \right] \left[\frac{T}{c + T} \right] \right) . \quad (\text{C.1})$$

	Water (0 – 50 °C)	Ice (–40 – 0 °C)
a	6.1121 hPa	6.1115 hPa
b	18.678	23.036
c	257.14 °C	279.82 °C
d	234.5 °C	333.70 °C

TABLE C.1: Coefficients for the empirical Arden Buck formula [Buck, 2012].

The following series of arithmetic transformations are simple and need not to be commented on:

$$\begin{aligned}
 \ln\left(\frac{e_s}{a}\right) &= \left(b - \frac{T}{d}\right) \left(\frac{T}{c+T}\right) = \frac{Tb}{c+T} - \frac{T^2}{dc+dT} \\
 &= \frac{dTb - T^2}{dc+dT} \\
 T^2 + dc \ln\left(\frac{e_s}{a}\right) + dT \ln\left(\frac{e_s}{a}\right) - bdT &= 0 \\
 T^2 + \left(d \ln\left(\frac{e_s}{a}\right) - bd\right) T + dc \ln\left(\frac{e_s}{a}\right) &= 0 \\
 T = \frac{1}{2} \left(-d \left[\ln\left(\frac{e_s}{a}\right) - b \right] \pm \left[d^2 \left(\ln\left(\frac{e_s}{a}\right) - b \right)^2 - 4dc \ln\left(\frac{e_s}{a}\right) \right]^{\frac{1}{2}} \right)
 \end{aligned}$$

Then substitution of the actual vapour pressure e for the saturation vapour pressure e_s yields the dewpoint temperature T_d as a result:

$$T_d = \frac{1}{2} \left(-d \left[\ln\left(\frac{e}{a}\right) - b \right] \pm \left[d^2 \left(\ln\left(\frac{e}{a}\right) - b \right)^2 - 4dc \ln\left(\frac{e}{a}\right) \right]^{\frac{1}{2}} \right) \quad (\text{C.2})$$

The coefficients as recommended by Buck [2012] in his more recent work are shown in Table C.1 for water vapour and ice. The values produce reasonably accurate results according to Buck [1981].

C.2 Conversion from vapour pressure to mixing ratio

When using model simulation output, typically the schemes produce outputs of water vapour mixing ratios Q_v in dimensionless units, e.g. kg/kg. In order to convert this output to vapour pressure, one needs to combine the definition of the

specific humidity

$$Q_v = \frac{m_v}{m_v m_d} = \frac{\rho_v}{\rho_v + \rho_d} \quad (\text{C.3})$$

and the ideal gas law

$$p = \rho R T \quad (\text{C.4})$$

with masses m , densities ρ and pressure p and indices for vapour and dry air. The following conversion leads to the conversion between partial pressure and mixing ratio:

$$\begin{aligned} \rho_v Q_v + \rho_d Q_v &= \rho_v \\ \rho_v (1 - Q_v) &= \rho_d Q_v \\ \rho_v &= \rho_d \left(\frac{Q_v}{1 - Q_v} \right) \\ \frac{e}{R_v T} &= \frac{p_d}{R_d T} \left(\frac{Q_v}{1 - Q_v} \right) \\ e &= \frac{R_v}{R_d} p_d \left(\frac{Q_v}{1 - Q_v} \right) \end{aligned}$$

with R_v and R_d the specific gas constants for water vapour and dry air respectively.

For practical purposes the specific humidity and the mixing ratio are interchangeable, in which case the approximation is made that the dry pressure p_d equals the total pressure p . The typical error when comparing the values is about 4 %. But with small effort one can substitute $p_d = p - e$ and then derive

$$e = \frac{p}{1 + \frac{R_d}{R_v} \left(\frac{1}{Q_v} - 1 \right)} . \quad (\text{C.5})$$

Then the saturation mixing ratio can be computed by substituting e_s for e and inverting the formula

$$Q_{vs} = \frac{1}{1 + \frac{R_v}{R_d} \left(\frac{p}{e_s} - 1 \right)} . \quad (\text{C.6})$$

C.3 Temperatures at lifting condensation levels

In order to estimate the temperature that a parcel would have at the lifting condensation level, the formulas of Bolton [1980] are used. The absolute temperature at the LCL is estimated by

$$T_L \approx \frac{1}{\frac{1}{T_d - 56 \text{ K}} + \frac{\ln\left(\frac{T}{T_d}\right)}{800 \text{ K}}} + 56 \text{ K}, \quad (\text{C.7})$$

with T and T_d in Kelvin. The conversion to the potential temperature at LCL Θ_L yields then

$$\Theta_L = T \left(\frac{p_0}{p - e} \right)^{\kappa_d} \left(\frac{T}{T_L} \right)^{0.28 Q_v}. \quad (\text{C.8})$$

C.4 Estimation of the equivalent potential temperature

In the last step of the estimation the equivalent potential temperature is computed by

$$\Theta_e \approx \Theta_L \exp \left[\left(\frac{3036 \text{ K}}{T_L} - 1.78 \right) Q_v (1 + 0.448 Q_v) \right]. \quad (\text{C.9})$$

There is another estimation by Holton [1972]:

$$\Theta_e \approx \Theta_L \exp \left[\frac{r_s(T_L) L_v(T_L)}{C_{pd} T_d} \right] \quad (\text{C.10})$$

with latent heat of vaporization L_v and specific heat of dry air for constant pressure C_{pd} . Another suggestion is from Stull [1988]:

$$\Theta_e \approx T_e \left(\frac{p_0}{p} \right)^{\kappa_d} \approx \left[T + \frac{L_v(T)}{C_{pd} Q_v} \right] \left(\frac{p_0}{p} \right)^{\kappa_d}. \quad (\text{C.11})$$

The latter two approximations seem to be less accurate and are hence not used in this thesis. Note that the approximation of Holton [1972] has interesting theoretical implications and that of Stull [1988] does not require to compute T_L , hence

Appendix C Calculation of the equivalent potential temperature

both approximations are mentioned here, because a few comparisons have been done throughout the study to evaluate the benefits of each of the methods.

Appendix D

Simulated Surface Variables

D.1 Example Snapshots

The following plots in Figure D.1 show an example of simulated surface variables (wind, temperature, precipitation rate) on the 7 June 2008 at 16:35 local time (GMT+8).

Of particular interest is the rain band at 23°N and 113.5°E (see Figure D.1c), which is located at the urban edge (compare Figure 3.4). From Figure D.1b it can be seen that the flow is approaching from the west-north-west and converges at the edge of the urban area (decrease of velocity). The surface temperature plot in Figure D.1a shows a clear difference in surface temperature in the area of the precipitation compared to the environment. The urban heat maximum (e.g. AH peak at this time of day plus passive heat storage in the late afternoon) is also clearly visible. The temperature gradient between urban and rural areas here is approximately 5 K in most places and at the hottest areas up to 9 K. These large values appear to be somewhat unrealistic and are most likely enhanced by the 500 W m^{-2} forcing through AH. Note that peak values of 309 K are high, but not impossible in this region in summer on extremely hot days, because the damping of temperature fluctuations and extremes by the seawater body decreases with distance from the coast, particularly in this area with complex topography.

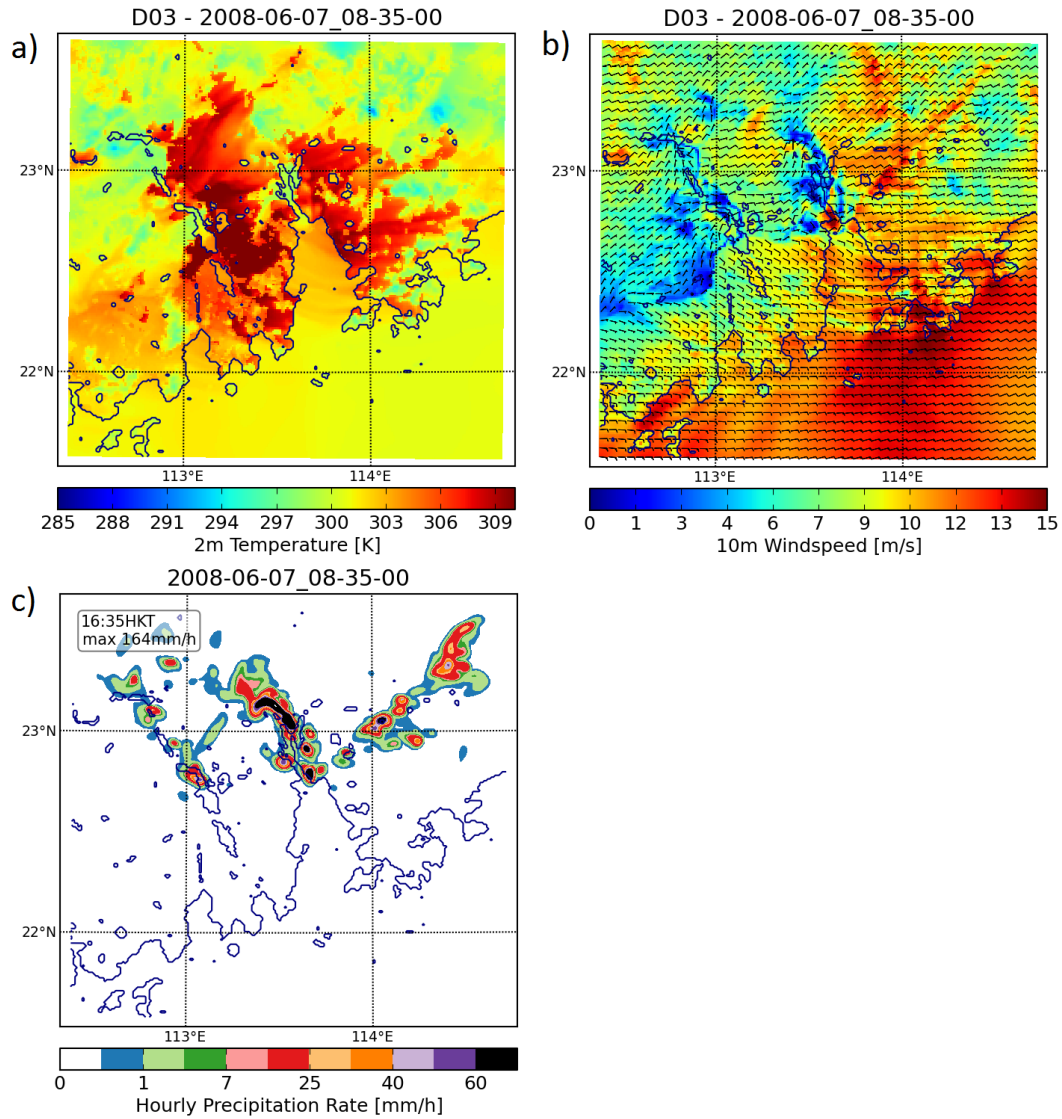


FIGURE D.1: Simulated surface temperatures (a), surface winds (b) and precipitation rates (c) in an example on 7 June 2008 at 16:35.

Even though urban ambient air temperature effects were not in the scope of this thesis, heat waves have a large impact on human health and hence are studied by growing numbers of researchers.

Bibliography

- Ackerman, B., Changnon, Jr., S., Dzurisin, C., Gatz, D. L., Grosh, R. C., Hilbers, S. D., Huff, F. A., Mansell, J. W., Ochs III, H. T., Peden, M. E., Schickedanz, P. T., Semonin, R. G., and Vogel, J. L. (1978). *Summary of METROMEX, Volume 2: Causes of Precipitation Anomalies*. State of Illinois, State Water Survey Division.
- Allen, L., Lindberg, F., and Grimmond, C. S. B. (2011). Global to city scale anthropogenic heat flux: model and variability. *International Journal of Climatology*, 31:1990–2005.
- Avissar, R. and Pielke, Sr, R. A. (1989). Parametrization of heterogeneous land surfaces for atmospheric numerical models and its impact on regional meteorology. *Monthly Weather Review*, 117:2113–2136.
- Bohnenstengel, S. I., Evans, S., Clark, P. A., and Belcher, S. E. (2011). Simulations of the London urban heat island. *Quarterly Journal of the Royal Meteorological Society*, 137:1625–1640.
- Bolton, D. (1980). The computation of equivalent potential temperature. *Monthly Weather Review*, 108:1046–1053.
- Bornstein, R. and Lin, Q. (2000). Urban heat islands and summertime convective thunderstorms in Atlanta: three case studies. *Atmospheric Environment*, 34:507–516.
- Bougeault, P. and Lacarèrre, P. (1989). Parameterization of orography-induced turbulence in a mesobeta-scale model. *Monthly Weather Review*, 117:1872–1890.

- Buck, A. (1981). New equations for computing vapor pressure and enhancement factor. *Journal of Applied Meteorology*, 20:1527–1532.
- Buck, A. (2012). *Buck Research Instruments L.L.C CR-1A User's Manual, Appendix 1, updated 1996*. Buck Research Instruments L.L.C.
- Chen, F. and Dudhia, J. (2001). Coupling and advanced land surface–hydrology model with the Penn State–NCAR MM5 modeling system. part i: Model implementation and sensitivity. *Monthly Weather Review*, 129:569–585.
- Chen, F., Mitchell, K., Schaake, J., Xue, Y., Pan, H. L., Koren, V., Duan, Q. Y., Ek, M., and Betts, A. (1996). Modeling of land surface evaporation by four schemes and comparison with FIFE observations. *Journal of Geophysical Research*, 101(D3):7251–7268.
- Dalu, G. A., Baldi, M., Pielke, Sr, R. A., Lee, J. T., and Colacino, M. (1991). Mesoscale vertical velocities generated by stress changes in the boundary layer: linear theory. *Annales Geophysicae*, 9:648–653.
- Dixon, P. G. and Mote, T. L. (2003). Patterns and causes of Atlanta’s urban heat island–initiated precipitation. *Journal of Applied Meteorology*, 42:1273–1284.
- Etling, D. (2008). *Theoretische Meteorologie, eine Einführung*. Springer, Berlin, Germany, 3rd edition.
- Gryschka, M., Drüe, C., Etling, D., and Raasch, S. (2008). On the influence of sea-ice inhomogeneities onto roll convection in cold-air outbreaks. *Geophysical Research Letters*, 35:L23804.
- Gryschka, M., Fricke, J., and Raasch, S. (2014). On the impact of forced roll convection on vertical turbulent transport in cold air outbreaks. *Journal of Geophysical Research Atmospheres*, 119:513–532.
- Hamdi, R., Van de Vyver, H., De Troch, R., and Termonia, P. (2013). Assessment of three dynamical urban climate downscaling methods: Brussels’s future urban heat island under an A1B emission scenario. *International Journal of Climatology*.

BIBLIOGRAPHY

- Han, J. and Pan, H.-L. (2011). Revision of convection and vertical diffusion schemes in NCEP Global Forecast System. *Weather And Forecasting*, 26:520–533.
- Holst, C. C., Tam, C.-Y., and Chan, J. C. L. (2016). Sensitivity of urban rainfall to anthropogenic heat flux: a numerical experiment. *Geophysical Research Letters*, 43(5):2240–2248.
- Holton, J. (1972). *An introduction to dynamic meteorology*. Academic Press, San Diego, California.
- Hong, S.-Y. and Lee, J.-W. (2009). Assessment of the WRF model in reproducing a flash-flood heavy rainfall event over Korea. *Atmospheric Research*, 93:818–831.
- Huff, F. A. and Changnon, Jr., S. A. (1972). Climatological assessment of urban effects on precipitation in St. Louis. *Journal of Applied Meteorology*, 11:823–842.
- Huff, F. A. and Changnon, jr., S. A. (1973). Precipitation modification by major urban areas. *Bulletin of the American Meteorological Society*, 54:1220–1232.
- Iacono, M. J., Delamere, J. S., Mlawer, E. J., Shephard, M. W., Clough, S. A., and Collins, W. D. (2008). Radiative forcing by long-lived greenhouse gases: Calculations with the AER radiative transfer models. *Journal of Geophysical Research*, 113:D13103.
- IPCC (2013). *Climate Change 2013: The Physical Science Basis. Contribution of Working Group 1 to the Fifth Assessment Report of the Intergovernmental Panel on Climate Change*. Cambridge University Press, Cambridge, United Kingdom.
- Kolmogorov, A. N. (1941). The local structure of turbulence in incompressible viscous fluid for very large reynolds numbers. *Proceedings of the USSR Academy of Sciences*, 30:pp 299.
- Krishtawal, C. M., Niyogi, D., Dewari, M., Pielke, Sr., R. A., and Shepherd, J. (2010). Urbanization signature in the observed heavy rainfall climatology over India. *International Journal of Climatology*, 30:1908–1916.

- Kusaka, H., Kondo, H., Kikegawa, Y., and Kimura, F. (2004). A simple single-layer urban canopy model for atmospheric models: Comparison with multi-layer and slab models. *Boundary Layer Meteorology*, 101:329–358.
- Lam, H. (2011). Lecture 1 setting the scene 2: Urban climate and climate change in hong kong. Croucher Advanced Study Institute 2011–2012, Urban Climatology for Tropical and Sub-Tropical Regions, School of Architecture, The Chinese University of Hong Kong.
- Landsberg, H. E. (1981). *The Urban Climate*. Academic Press, London, United Kingdom.
- Lei, M., Niyogi, D., Krishtawal, C., Pielke, Sr., R. A., Beltran-Przekurat, A., Nobis, T. E., and Vaidya, S. S. (2008). Effect of explicit urban land surface representation on the simulation of the 26 July 2005 heavy rain event over Mumbai, India. *Atmospheric Chemistry and Physics*, 8:5975–5995.
- Li, X.-X., Koh, T.-Y., Panda, J., and Norford, L. K. (2016). Impact of urbanization patterns on the local climate of a tropical city, Singapore: An ensemble study. *Journal of Geophysical Research: Atmospheres*, 121(9):4386–4403.
- Lo, J. C. F., Lau, A. K. H., Chen, F., Fung, J. C. H., and Leung, K. K. M. (2007). Urban modification in a mesoscale model and the effects on the local circulation in the Pearl River Delta Region. *Journal of Applied Meteorology and Climatology*, 46:457–476.
- Miguez-Macho, G., Stechikov, G. L., and Robock, A. (2004). Spectral nudging to eliminate the effects of domain position and geometry in regional climate model simulations. *Journal of Geophysical Research*, 109:D13104.
- Mok, H. Y., Leung, Y. K., Lee, T. C., and Wu, M. C. (2006). Regional rainfall characteristics of Hong Kong over the past 50 years. *Conference on “Changing Geography in a Diversified World”, Hong Kong Baptist University, Hong Kong, China, 1-3 June 2006*, Hong Kong Observatory Reprint 646.

BIBLIOGRAPHY

- Mossman, R. C. (1897). The non-instrumental meteorology of London, 1713—1896. *Quarterly Journal of the Royal Meteorological Society*, 23:287–298.
- Mossman, R. C. (1898a). Daily values of non-instrumental meteorological phenomena in London, 1763–1896. *Quarterly Journal of the Royal Meteorological Society*, 24:31–41.
- Mossman, R. C. (1898b). On the frequency of non-instrumental meteorological phenomena in London with different winds from 1763–1896. *Quarterly Journal of the Royal Meteorological Society*, 24:238–249.
- Niyogi, D., Pyle, P., Lei, M., Pal Arya, S., Krishtawal, C. M., Shepherd, J. M., Chen, F., and Wolfe, B. (2011). Urban modification of thunderstorms: An observational storm climatology and model case study for the Indianapolis urban region. *Journal of Applied Meteorology and Climatology*, 50(4):1129–1144.
- Oke, T. R. (1987). *Boundary Layer Climates*. Routledge, London , United Kingdom, 2nd edition.
- Oke, T. R. (1988). The urban energy balance. *Progress in Physical Geography*, 12(4):471–508.
- Orville, R. E., Huffines, G., Nielsen-Gammon, J., Zhang, R., Ely, B., Steiger, S., Phillips, S., Allen, S., and Read, W. (2001). Enhancement of cloud-to-ground lightning over Houston, Texas. *Geophysical Research Letters*, 28(13):2597–2600.
- Paegle, J., Mo, K. C., and Nogues-Paegle, J. (1996). Dependence of simulated precipitation on surface evaporation during the 1993 United States summer floods. *Monthly Weather Review*, 124:345–361.
- Penelly, C., Reuter, G., and Flesch, T. (2013). Verification of the WRF model for simulating heavy precipitation in Alberta. *Atmospheric Research*, 135–136:172–192.
- Pielke, Sr, R. A., Adegoke, J., Beltran-Przekurat, A., Hiemstra, C. A., Ling, J., Nair, U., Niyogi, D., and Nobis, T. (2007). An overview of regional land-use and land-cover impacts on rainfall. *Tellus*, 59B:587–601.

- Roy, S. B. and Traiteur, J. J. (2010). Impacts of wind farms on surface air temperatures. *Proceedings of the National Academy of Sciences of the United States of America*, 107:17899–17904.
- Shepherd, J. M. and Burian, S. J. (2003). Detection of urban-induced rainfall anomalies in a major coastal city. *Earth Interactions*, 7:1–17.
- Skamarock, W. C., Klemp, J. B., Dudhia, J., Gill, D. O., Barker, D. M., Duda, M., Huang, X.-Y., Wang, W., and Powers, J. G. (2008). *A description of the advanced research WRF version 3 NCAR Technical Note*. NCAR/TN-475+STR.
- Srikanth, S., Satyanarayana, A. N. V., and Narayana Rao, T. (2014). Performance evaluation of PBL and cumulus parametrization schemes for WRF ARW model in simulating severe thunderstorm events over Gadanki MST RADAR facility – Case study. *Atmospheric Research*, 139:1–17.
- Steiger, S. M. and Orville, R. E. (2003). Cloud-to-ground lightning enhancement over Southern Louisiana. *Geophysical Research Letters*, 30(19).
- Stull, R. B. (1976). The energetics of entrainment across a density interface. *Jounral of Atmopsheric Science*, 33:1260–1267.
- Stull, R. B. (1988). *An introduction to boundary layer meteorology*. Kluwer Academic Publishers, Dordrecht, Netherlands.
- Sühring, M., Maronga, B., Herbort, F., and Raasch, S. (2014). On the effect of surface heat-flux heterogeneities on the mixed-layer-top entrainment. *Boundary Layer Meteorology*, 151:531–556.
- Tewari, M., Chen, F., Wang, W., Dudhia, J., LeMone, M. A., Mitchell, K., Ek, M., Gayno, G., Wegiel, J., and Cuenca, R. H. (2004). Implementation and verification of the unified NOAH land surface model in the WRF model. *20th Conference on weather analysis and forecasting/16th conference on numerical weather prediction*, pages 11–15.

BIBLIOGRAPHY

- Trenberth, K. E., Dai, A., Rasmusson, R. M., and Parsons, D. B. (2003). The changing character of precipitation. *Bulletin of the American Meteorological Society*, 84:1205–1217.
- van den Heever, S. C. and Cotton, W. R. (2007). Urban aerosol impacts on downwind convective storms. *Journal of Applied Meteorology and Climatology*, 46:828–850.
- Vukovich, F. and Dunn III, J. W. (1978). A theoretical study of the St. Louis Heat island: Some parameter variations. *Journal of Applied Meteorology*, 17(11):1585–1594.
- Vukovich, F., Dunn III, J. W., and Chrissman, B. W. (1976). A theoretical study of the St. Louis heat island: The wind and temperature distribution. *Journal of Applied Meteorology*, 15(5):417–440.
- Vukovich, F. and King, W. J. (1980). A theoretical study of the St. Louis heat island: Comparisons between observed data and simulation results on the urban heat island circulation. *Journal of Applied Meteorology*, 19(7):761–770.
- Wallace, J. M. and Hobbs, P. V. (2006). *Atmospheric Science - An introductory survey*. Academic Press, Cambridge, Massachusetts, United States of America, 2nd edition. doi:10.1016/B978-0-12-732951-2.50002-8.
- Westra, S., Alexander, L. V., and Zwiers, F. W. (2013). Global increasing trends in annual maximum daily precipitation. *Journal of Climate*, 26:3904–3918.
- Wong, M. C., Mok, H. Y., and Lee, T. C. (2010). Observed changes in extreme weather indices in Hong Kong. *International Journal of Climatology*, 31:2300–2311.
- Wu, M. C., Lam, H., and Li, K. W. (2015). Characterization and indexing of heavy rainstorms in Hong Kong. *Meteorological Applications*, 22:25–36.
- Yu, E.-T., Sun, J. Q., and Xiang, W.-L. (2013). High-Resolution Hindcast of Record-Breaking Rainfall in Beijing and Impact of Topography. *Atmospheric and Oceanic Science Letters*, 6(5):253–258.

BIBLIOGRAPHY

- Yu, M. and Liu, Y. (2015). The possible impact of urbanization on a heavy rainfall event in Beijing. *Journal of Geophysical Research: Atmospheres*, 120(16):8132–8143.